

Strontium titanate based materials for use as oxygen transport membranes in membrane reactors

Yuning Tang

Energie & Umwelt / Energy & Environment Band / Volume 674 ISBN 978-3-95806-849-0



Forschungszentrum Jülich GmbH Institute of Energy Materials and Devices (IMD) Werkstoffsynthese und Herstellungsverfahren (IMD-2)

Strontium titanate based materials for use as oxygen transport membranes in membrane reactors

Yuning Tang

Schriften des Forschungszentrums Jülich Reihe Energie & Umwelt / Energy & Environment Bibliografische Information der Deutschen Nationalbibliothek. Die Deutsche Nationalbibliothek verzeichnet diese Publikation in der Deutschen Nationalbibliografie; detaillierte Bibliografische Daten sind im Internet über http://dnb.d-nb.de abrufbar.

UNIVERSITY OF TWENTE.

Herausgeber Forschungszentrum Jülich GmbH

und Vertrieb: Zentralbibliothek, Verlag

52425 Jülich

Tel.: +49 2461 61-5368 Fax: +49 2461 61-6103 zb-publikation@fz-juelich.de

www.fz-juelich.de/zb

Umschlaggestaltung: Grafische Medien, Forschungszentrum Jülich GmbH

Druck: Grafische Medien, Forschungszentrum Jülich GmbH

Copyright: Forschungszentrum Jülich 2025

Schriften des Forschungszentrums Jülich Reihe Energie & Umwelt / Energy & Environment, Band / Volume 674

(Diss. University of Twente, 2025)

ISSN 1866-1793 ISBN 978-3-95806-849-0

ISBN (print): 978-90-365-6869-2 (University of Twente) ISBN (digital): 978-90-365-6870-8 (University of Twente)

Vollständig frei verfügbar über das Publikationsportal des Forschungszentrums Jülich (JuSER) unter www.fz-juelich.de/zb/openaccess.



This is an Open Access publication distributed under the terms of the <u>Creative Commons Attribution License 4.0</u>, which permits unrestricted use, distribution, and reproduction in any medium, provided the original work is properly cited.

Graduation Committee:

Chair / secretary: prof.dr. J.J.L.M. Cornelissen

Promotors: prof.dr.ir. W.A. Meulenberg

Universiteit Twente, TNW, Inorganic Membranes

prof.dr.ir. A. Nijmeijer

Universiteit Twente, TNW, Inorganic Membranes

Co-promotor: dr. S. Baumann

Forschungszentrum Jülich GmbH

Committee Members: prof. dr. J. M. Serra Alfaro

Universitat Politècnica de València, CSIC-Instituto de Tecnología

Química (ITQ)

prof. dr. M.C.M. Van De Sanden

University of Eindhoven, Applied Physics and Science Education

prof.dr.ir. L. Lefferts

Universiteit Twente, TNW, Catalytic Processes and Materials

prof.dr. G. Mul

Universiteit Twente, TNW, Photocatalytic Synthesis

prof.dr.ir. G. Koster

Universiteit Twente, TNW, Inorganic Materials Science

Content

SUMMARY

SAMENVATTING

1. Introduction	1
1.1 Oxygen separation	1
1.2 Application in membrane reactors	4
1.3 Mixed ionic and electronic conductors (MIEC)	6
1.3.1 Single phase materials for OTMs	6
1.3.2 Dual phase materials for OTMs	8
1.3.3 Material selection	9
1.4 Oxygen transport mechanism	10
1.5 Scope of the thesis.	13
REFERENCES	17
2. Ni-doping influence on functional properties of SrTi _{0.65} Fe _{0.35} O _{3-δ} for use as oxy	gen transport
membranes	26
Abstract	26
2.1 Introduction	27
2.2 Experimental	28
2.2.1 Sample preparation	28
2.2.2 Structural characterization	29
2.2.3 Electrical conductivity measurements	29
2.2.4 Oxygen permeation measurement	30
2.2.5 Annealing measurement	31
2.3 Results and discussion	32
2.3.1 Crystal structure and microstructure	32
2.3.2 Functional properties	34
2.3.3 Thermo-chemical stability	38

2.4 Conclusions	45
REFERENCES	46
3. Functional properties of highly stable SrTi _{0.95-x} Zr _{0.05} Ni _x O _{3-δ} for use as or	xygen transport
membranes	52
Abstract	52
3.1 Introduction	53
3.2 Experimental	54
3.2.1 Powder preparation	54
3.2.2 Characterization methods	55
3.2.3 Electrical conductivity	56
3.2.4 Oxygen permeation measurement	57
3.3 Results and discussion	59
3.3.1 Crystal structure and microstructure	59
3.2 Functional properties	62
3.2.1 Electrical conductivity	62
3.2.2 Oxygen permeation	64
3.3.3 Thermo-chemical stability	68
3.4 Conclusions	72
REFERENCES	74
4.The effects of microstructure and functional properties of Mg and	Al doped into
SrTi _{0.65} Fe _{0.35} O ₃₋₈ (STF35)	79
Abstract	79
4.1 Introduction	80
4.2 Experimental	82
4.2.1 Sample preparation	82
4.2.2 Structural characterization	82
4.2.3 Oxygen permeation measurement	83
4.3 Results and discussion	84
4.3.1 Microstructure	84

4.3.2 Oxygen permeation	86
4.3.3 Oxygen vacancy concentration change of STFM _x	91
4.3.4 MgO segregation of STFM	93
4.4 Conclusions	95
REFERENCES	97
5. The performance of B-site doped STO ₃ in a membrane reactor	101
Abstract	101
5.1 Introduction	102
5.2 Experimental	104
5.2.1 Sample preparation	104
5.2.2 Structural characterization	105
5.2.3 Membrane reactor set up	105
5.3 Results and discussion	106
5.3.1 Oxygen flux in different conditions	106
5.3.2 CH ₄ conversion and selectivity	116
5.4 Conclusions	118
REFERENCES	120
6. Reflections and Conclusions	123
6.1 Introduction	123
6.1.1 Samples selection	124
6.1.2 Performance in a membrane reactor	127
6.2 Conclusions	129
Acknowledgements	130

SUMMARY

Perovskite-structured oxygen transport membranes hold great potential for the energy-efficient separation of pure oxygen from air. While many materials have demonstrated excellent performance, their industrial application still remains limited due to the lack of material stability, which hinders long-term operation under the required conditions. Preliminary studies suggest that strontium titanate SrTiO₃ is a promising candidate for membrane reactors due to its superior chemical and mechanical stability in harsh environments. However, its electronic and ionic conductivity remains negligible over a wide range of temperatures and oxygen partial pressures. To enhance conductivity, a B-site doping strategy is employed. The research focuses on developing SrTiO₃-based materials by substituting a portion of titanium with redox-active transition metals to obtain both sufficient oxygen permeability and strong chemical stability. Chapter 1 introduces the foundational principles of CO₂ capture, oxygen separation technology and membrane reactors incorporating integrated oxygen transport membranes (OTMs) for efficient oxygen separation. It explores the core mechanisms governing oxygen transport in these membranes, with a particular focus on charge carrier dynamics within the bulk material and at the surface of mixed ionic electronic conducting (MIEC) materials. The chapter also discusses conventional single-phase and dual-phase materials used in OTMs, while presenting the key components of the single composite system examined in this study. Chapter 2 explores the impact of Fe/Ni co-doping at the B-site of STO₃ on its structural and functional properties for application as an OTM. The findings indicate that Ni doping at the Bsite enhances both the electronic and ionic conductivities of SrTi_{0.65}Fe_{0.35}O₃₋₈ (STF35). The oxygen permeance of $SrTi_{0.65-x}Fe_{0.35}Ni_xO_{3-\delta}$ (x=0, 0.05, 0.075, 0.1) (STFN_x) slightly increases with Ni concentration and is comparable to that of the benchmark material La_{0.6}Sr_{0.4}Co_{0.2}Fe_{0.8}O_{3-δ} (LSCF6428). A key observation is that the even 5 mol% Ni-doped material STFN005 exhibits a uniformly distributed Fe/Ni exsolution after annealing in a reducing atmosphere, which could enhance catalytic performance in membrane reactors. All samples still possess the main peaks of perovskite evenly annealed in a very harsh condition, i.e. syngas with high H₂S contamination. However, the stability of STFN_x decreased as Ni content increased Additionally, two-cycle TGA measurements demonstrated that STF35 and SrTi_{0.60}Fe_{0.35}Ni_{0.05}O_{3-δ} (STFN005) exhibited greater stability in reducing environments compared to others. Therefore, STFN005, with 5 mol%. Ni doping, emerges as a promising candidate for partial oxidation of methane (POM) applications in membrane reactors.

Chapter 3 provides a systematic investigation into the microstructure, functional properties, and stability of the SrTi_{0.95-x}Zr_{0.05}Ni_xO_{3-δ} (x=0.01, 0.03, 0.05, 0.10, 0.15) (STZN_x) series materials for their potential use as OTMs. XRD analysis confirmed that the solubility limit of Ni in the perovskite structure is below 15 mol%. The results indicate that substituting Ti with Ni significantly enhances the oxygen permeability and electrical conductivity of STZN_x. All samples maintain their single-phase structure even after annealing in 2.9 vol% H₂/Ar for 48 hours. Notably, STZN10 exhibits a uniform distribution of Ni particles on its surface after annealing, which can serve as active catalytic centers in membrane reactor applications. Three-cycle TGA measurements reveal that all STZN_x materials demonstrate reversible oxygen exchange, further indicating excellent stability in reducing atmospheres.

Although the oxygen flux of STZN10 is lower than that of many B-site doped SrTiO₃ materials, it presents unique advantages of Ni exsolution and exceptional structural stability in reducing conditions for OTM applications, particularly in high-temperature membrane reactors involving hydrocarbon processing. Further optimization strategies can be considered to improve its oxygen permeability to position STZN10 as a promising candidate for high-temperature membrane reactor applications that integrate separation and reaction processes, such as the partial oxidation of methane, where both catalytic activity and structural stability are critical.

The microstructures and oxygen permeability of $SrTi_{0.65-x}Fe_{0.35}Al_xO_{3-\delta}$ (x=0.01, 0.03, 0.05, 0.10, 0.15) (STFA_x) and $SrTi_{0.65-x}Fe_{0.35}Mg_xO_{3-\delta}$ (x=0.01, 0.03, 0.05, 0.10) (STFM_x) series materials is studied in **Chapter 4**. XRD analysis confirmed that the STFA_x samples maintain a single-phase structure across the studied composition range (up to 15 mol%). In contrast, the solubility limit of Mg in the STFM_x series is below 10 mol%. Oxygen permeation measurements indicate that Al doping is unsuitable in the STFA_x system, as increased Al content leads to a decline in oxygen permeability. Similarly, MgO segregation is observed on

STFM_x materials, which negatively impacted the oxygen permeability of the materials. Consequently, understanding and mitigating MgO segregation is crucial for optimizing material performance. Further optimization strategies could be employed to minimize MgO segregation and enhance permeability, which could still make STFM_x as a promising candidate for oxygen transport membranes (OTMs) in membrane reactor applications

Chapter 5 explores the oxygen flux and catalytic performance of selected materials, including STFN005, SrTi_{0.75}Fe_{0.25}O_{3-\delta} with STFN005 catalytic layer (STF25 cl), SrTi_{0.65}Fe_{0.35}O_{3-\delta} with STFN005 catalytic layer (STF35 cl), and STZN10 for use as OTMs in a membrane reactor. The oxygen flux of STFN005 is evaluated under three different gas environments: air/Ar, air/10 vol% CH₄ and 15 vol% CO₂/10 vol% CH₄. The results indicate that the highest oxygen flux of STFN005 (0.55 mL·cm⁻²·min⁻¹) is achieved in air/10 vol% CH₄, suggesting that partial oxidation of methane (POM) reaction promotes oxygen transport. The remeasured oxygen flux and microstructure characterization after testing demonstrates the good crystal stability of STFN005. However, the membrane fractured due to chemical expansion. Additionally, Ni exsolution is observed on the membrane surface after the experiments. For STF25 cl, despite exhibiting lower oxygen permeability than STFN005 under air/Ar condition, it demonstrates higher permeability in air/10 vol% CH₄, suggesting the porous STFN005 catalytic layer significantly enhances catalytic performance by optimizing surface exchange kinetics and creating redox-active Fe/Ni sites. Furthermore, STF25_cl remained structurally intact, indicating strong thermochemical stability in reducing atmospheres. Activation energy analysis in air/Ar and air/10 vol% CH₄ reveals that STF35 cl exhibits improved oxygen surface exchange and bulk diffusion properties compared to STFN005 and STF25 cl. However, like STFN005, STF35 cl also fractures after exposure to the reducing atmosphere due to chemical expansion. STZN10 exhibits the lowest oxygen flux among the studied materials. The postexperiment membrane photograph and the microstructure analysis of the sweep side demonstrates its excellent thermochemical stability in reducing environments. Product selectivity analysis identified distinct reaction pathways for each material. STFN005 excel in syngas production (POM), while STF25 cl/STF35 cl suit oxy-combustion. STZN10 is promising for oxidative coupling of methane (OCM). Further optimization of the membrane architecture, including precise thickness control and asymmetric structural design and so on, is expected to enhance membrane performance for target reactions in membrane reactors.

Chapter 6 summarizes all obtained results, reflects on the overall findings, and further determines a direction for future research. It shows that STFN005, with 5 mol% Ni doping, emerges as a promising candidate for POM applications in membrane reactors due to its high oxygen permeance, Ni exsolution, and good stability in reducing environments. STZN10 is promising for OCM reaction due Ni exsolution and exceptional structural stability. However, further optimization strategies should be considered to improve its oxygen permeability. MgO segregation is observed on STFM_x materials, which negatively impacted the oxygen permeability of the materials. Further optimization strategies could be employed to minimize MgO segregation and enhance permeability, which could still make STFM_x as a promising candidate for oxygen transport membranes (OTMs) in membrane reactor applications. The porous STFN005 catalytic layer on STE25_cl and STF35_cl significantly enhances catalytic performance by optimizing surface exchange kinetics and creating redox-active Fe/Ni sites, making them suitable for oxy-combustion. Further optimization of membrane architecture, including precise thickness control and asymmetric structural design and so on, is expected to enhance membrane performance for target reactions in membrane reactors.

SAMENVATTING

Perovskiet-gestructureerde zuurstoftransportmembranen bieden veel potentieel voor de energie-efficiënte scheiding van pure zuurstof uit lucht. Hoewel veel materialen uitstekende prestaties hebben laten zien, blijft industriële toepassing beperkt door het gebrek aan materiaalkundige stabiliteit, wat langdurige werking onder de vereiste omstandigheden belemmert. Voorlopige studies suggereren dat strontiumtitanaat (SrTiO₃) een veelbelovende kandidaat is voor membraanreactoren vanwege zijn superieure chemische en mechanische stabiliteit in agressieve omgevingen. Echter, de elektronische en ionische geleidbaarheid is verwaarloosbaar over een breed temperatuurbereik en zuurstofpartiaaldrukken. Om de geleidbaarheid te verbeteren, wordt een strategie toegepast waarbij het op de B-positie wordt gedoteerd. Het onderzoek richt zich op het ontwikkelen van op SrTiO₃ gebaseerde materialen door een deel van het titanium te vervangen door redox-actieve overgangsmetalen om zowel voldoende zuurstofdoorlaatbaarheid als sterke chemische stabiliteit te verkrijgen.

introduceert fundamentele Hoofdstuk de principes van CO₂-afvang, membraanreactoren zuurstofscheidingstechnologie geïntegreerde en met zuurstoftransportmembranen (OTMs) voor efficiënte zuurstofscheiding. Het onderzoekt de kernmechanismen die zuurstoftransport in deze membranen sturen, met een bijzondere focus op ladingsdragerdynamiek binnen het bulk-materiaal en aan het oppervlak van gemengd ionisch-elektronisch geleidende (MIEC) materialen. Ook conventionele enkel- en tweefasige materialen die worden gebruikt in OTMs worden besproken, evenals de belangrijkste componenten van het enkelvoudige composietsysteem dat in deze studie wordt onderzocht.

Hoofdstuk 2 onderzoekt de impact van Fe/Ni-co-dotering op de B-positie van SrTiO₃ op de structurele en functionele eigenschappen met het oog op toepassing als OTM. De bevindingen tonen aan dat Ni-dotering op de B-positie zowel de elektronische als ionische geleidbaarheid van SrTi_{0.65}Fe_{0.35}O_{3-δ} (STF35) verbetert. De zuurstofdoorlaatbaarheid van SrTi_{0.65-x}Fe_{0.35}Ni_xO_{3-δ} (x=0, 0.05, 0.075, 0.1) (STFN_x) neemt licht toe met de Ni-concentratie en is vergelijkbaar met het referentiemateriaal La_{0.6}Sr_{0.4}Co_{0.2}Fe_{0.8}O_{3-δ} (LSCF6428). Een belangrijk resultaat is dat het materiaal met 5 mol% Ni-dotering (STFN005) een uniforme verdeling van Fe/Ni-exsolutie vertoont na gloeien in een reducerende atmosfeer, wat de katalytische prestaties in membraanreactoren kan verbeteren. Alle monsters behouden de hoofdstructuur van het perovskiet, zelfs na gelijkmatige behandeling onder zware

omstandigheden ophoge temperatuur, zoals synthese gas met hoge H₂S-verontreiniging. Echter, de stabiliteit van STFN_x daalt bij toenemende Ni-concentratie. Bovendien tonen TGA-metingen over twee cycli aan dat STF35 en SrTi_{0.60}Fe_{0.35}Ni_{0.05}O₃₋₈ (STFN005) grotere stabiliteit vertonen in reducerende omgevingen. Daarom blijkt STFN005, met 5 mol% Ni-dotering, een veelbelovende kandidaat te zijn voor toepassingen zoals de partiële oxidatie van methaan (POM) in membraanreactoren.

Hoofdstuk 3 biedt een systematisch onderzoek naar de microstructuur, functionele eigenschappen en stabiliteit van de $SrTi_{0.95-x}Zr_{0.05}Ni_xO_{3-\delta}$ (x=0.01, 0.03, 0.05, 0.10, 0.15) (STZN_x)-reeks voor hun potentiële gebruik als OTMs. XRD-analyse bevestigt dat de oplosbaarheidsgrens van Ni in de perovskietstructuur onder de 15 mol% ligt. De resultaten tonen aan dat vervanging van Ti door Ni de zuurstofdoorlaatbaarheid en elektrische geleidbaarheid van STZNx aanzienlijk verbetert. Alle monsters behouden hun enkelvoudige fase-structuur, zelfs na 48 uur behandeling op hoge termperatuur in 2.9 vol% H₂/Ar. Opmerkelijk is dat STZN10 een uniforme verdeling van Ni-deeltjes aan het oppervlak vertoont na de temperatuur behandeling, wat kan dienen als actieve katalytische centra in membraanreactoren. TGA-metingen over drie cycli tonen aan dat alle STZN_x-materialen reversibele zuurstofuitwisseling vertonen, wat wijst op uitstekende stabiliteit in reducerende atmosferen. Hoewel de zuurstofflux van STZN10 lager is dan die van veel andere B-gedoteerde SrTiO₃-materialen, biedt het unieke voordelen zoals Ni-exsolutie en uitzonderlijke structurele stabiliteit in reducerende omstandigheden voor OTM-toepassingen, met name in hoge membraanreactoren koolwaterstofverwerking. Verdere temperatuur voor optimalisatiestrategieën kunnen worden overwogen om de zuurstofdoorlaatbaarheid te verbeteren en STZN10 te positioneren als een veelbelovende kandidaat voor membraanreactortoepassingen waarbij scheiding en reactieprocessen worden geïntegreerd, zoals POM, waarbij zowel katalytische activiteit als structurele stabiliteit cruciaal zijn.

Hoofdstuk 4 behandelt de microstructuur en zuurstofdoorlaatbaarheid van SrTi_{0.65-x}Fe_{0.35}Al_xO_{3-δ} (x=0.01, 0.03, 0.05, 0.10, 0.15) (STFA_x) en SrTi_{0.65-x}Fe_{0.35}Mg_xO_{3-δ} (x=0.01, 0.03, 0.05, 0.10) (STFM_x). XRD-analyse bevestigt dat de STFA_x-monsters een enkelvoudige fase-structuur behouden binnen het onderzochte concentratiebereik (tot 15 mol%). Daarentegen ligt de oplosbaarheidsgrens van Mg in het STFMx-systeem onder de 10 mol%. Metingen van de zuurstofdoorlaatbaarheid wijzen uit dat Al-dotering ongeschikt is in het STFAx-systeem, aangezien een toename in Al-gehalte leidt tot een afname in zuurstofdoorlaatbaarheid. Evenzo wordt MgO-segregatie waargenomen in STFMx-materialen, wat de zuurstofdoorlaatbaarheid negatief beïnvloedt. Begrip van en oplossingen voor MgO-

segregatie zijn dus essentieel voor het optimaliseren van de materiaaleigenschappen. Verdere optimalisaties kunnen MgO-segregatie minimaliseren en de doorlaatbaarheid verbeteren, wat $STFM_x$ alsnog tot een veelbelovende kandidaat voor OTMs in membraanreactoren maakt.

Hoofdstuk 5 onderzoekt de zuurstofdoorlaatbaarheid en katalytische prestaties van geselecteerde materialen, waaronder STFN005, SrTi_{0.75}Fe_{0.25}O₃₋₈ met een STFN005katalytische laag (STF25 cl), SrTi_{0.65}Fe_{0.35}O₃₋₆ met STFN005-katalytische laag (STF35 cl), en STZN10 voor gebruik als OTMs in een membraanreactor. De zuurstofflux van STFN005 wordt geëvalueerd onder drie verschillende gassamenstellingen: lucht/Ar, lucht/10 vol% CH₄ en 15 vol% CO₂/10 vol% CH₄. De hoogste zuurstofdoorlaatbaarheid van STFN005 (0.55 mL·cm⁻²·min⁻¹) wordt bereikt in lucht/10 vol% CH₄, wat erop wijst dat de POM-reactie het zuurstoftransport bevordert. Herhaalde fluxmetingen en microstructuuranalyse na de test tonen aan dat STFN005 een goede kristalstabiliteit heeft. Echter, het membraan brak door chemische expansie. Daarnaast werd Ni-exsolutie waargenomen op het membraanoppervlak na de experimenten. Hoewel STF25 cl onder lucht/Ar lagere zuurstofdoorlaatbaarheid vertoont dan STFN005, toont het een hogere doorlaatbaarheid onder lucht/10 vol% CH₄. Dit suggereert dat de poreuze STFN005-katalytische laag de katalytische prestaties aanzienlijk verbetert door optimalisatie van de oppervlaktewisselkinetiek en vorming van redox-actieve Fe/Ni-sites. Bovendien bleef STF25 cl structureel intact, wat wijst op sterke thermochemische stabiliteit. Activeringsenergie-analyse laat zien dat STF35 cl verbeterde zuurstofoppervlakteuitwisseling en bulkdiffusie-eigenschappen heeft ten opzichte van STFN005 en STF25 cl. Echter, net als STFN005, breekt STF35 cl na blootstelling aan reducerende atmosfeer door chemische expansie. STZN10 vertoont de laagste zuurstofdoorlaatbaarheid van alle onderzochte materialen. Analyse na het experiment toont uitstekende thermochemische stabiliteit van STZN10 aan in reducerende omgevingen. Productselectiviteit toont aan dat STFN005 uitblinkt in syngas productie (POM), terwijl STF25 cl/STF35 cl geschikt zijn voor oxy-combustie. STZN10 is veelbelovend voor oxidatieve koppeling van methaan (OCM). Verdere optimalisatie van de membraanarchitectuur, inclusief nauwkeurige diktecontrole en asymmetrisch ontwerp, wordt verwacht de membraanprestaties voor specifieke reacties in membraanreactoren te verbeteren.

Hoofdstuk 6 vat alle verkregen resultaten samen, reflecteert op de algemene bevindingen en bepaalt een richting voor toekomstig onderzoek. STFN005, met 5 mol% Ni-dotering, komt naar voren als een veelbelovende kandidaat voor POM-toepassingen in membraanreactoren vanwege zijn hoge zuurstofdoorlaatbaarheid, Ni-exsolutie en goede stabiliteit in reducerende omgevingen. STZN10 is veelbelovend voor OCM-reacties dankzij Ni-exsolutie en

uitzonderlijke structurele stabiliteit. Echter, verdere optimalisatiestrategieën zijn nodig om de zuurstofdoorlaatbaarheid te verbeteren. MgO-segregatie die werd waargenomen in STFM_x-materialen beïnvloedt de zuurstofdoorlaatbaarheid negatief. Verdere optimalisatie zou deze segregatie kunnen minimaliseren en de prestaties verbeteren, waardoor STFM_x nog steeds een kansrijke kandidaat blijft voor OTM-toepassingen. De poreuze STFN005-katalytische laag op STF25_cl en STF35_cl verbetert de katalytische prestaties aanzienlijk, en maakt hen geschikt voor oxy-combustie. Verdere optimalisatie van de membraan architectuur, zoals nauwkeurige diktecontrole en asymmetrisch ontwerp, zal naar verwachting de prestaties van membranen voor gerichte reacties in membraanreactoren verbeteren.

Abbreviations

Materials

 $SrTi_{0.75}Fe_{0.25}O_{3-\delta}$ STF25 SrTin 65Fen 35O3-8 STF35 SrTio 60Fe0 35Nio 05O3-8 STFN005 $SrTi_{0.575}Fe_{0.35}Ni_{0.075}O_{3-\delta}$ STFN0075 $SrTi_{0.55}Fe_{0.35}Ni_{0.10}O_{3-\delta}$ STFN010 SrTio 94Zro 05Nio 01O3-8 STZN1 SrTio 92Zro 05Nio 03O3-8 STZN3 $SrTi_{0.90}Zr_{0.05}Ni_{0.05}O_{3-\delta}$ STZN5 $SrTi_{0.85}Zr_{0.05}Ni_{0.10}O_{3-\delta}$ STZN10 SrTio 80Zro 05Nio 15O3-8 STZN15 $SrTi_{0.64}Fe_{0.35}Al_{0.01}O_{3-\delta}$ STFA1 $SrTi_{0.62}Fe_{0.35}Al_{0.03}O_{3-\delta}$ STFA3 SrTio 60Fe0 35Alo 05O3-8 STFA5 $SrTi_{0.55}Fe_{0.35}Al_{0.10}O_{3-\delta}$ STFA10 $SrTi_{0.50}Fe_{0.35}Al_{0.15}O_{3-\delta}$ STFA15 $SrTi_{0.64}Fe_{0.35}Mg_{0.01}O_{3-\delta}$ STFM1 $SrTi_{0.62}Fe_{0.35}Mg_{0.03}O_{3-\delta}$ STFM3 STFM5 $SrTi_{0.60}Fe_{0.35}Mg_{0.05}O_{3-\delta}$ $SrTi_{0.55}Fe_{0.35}Mg_{0.10}O_{3-\delta}$ STFM10 LSCF6428 $La_{0.6}Sr_{0.4}Co_{0.2}Fe_{0.8}O_{3-\delta}$

Abbreviations

CCS Carbon Capture and Storage

ASUs Air Separation Units

OTMs Oxygen Transport Membranes

MIEC Mixed Ionic and Electronic Conductor

CMRs Catalytic Membrane Reactors
OCM Oxidative Coupling of Methane
POM Partial Oxidation of Methane

ODHE Oxidative Dehydrogenation of Ethane

ICP-OES Inductively Coupled Plasma Optical Emission Spectroscopy

PSD Particle Size Distribution

XRD X-ray Diffraction

SEM Scanning Electron Microscopy

EDS Energy Dispersive X-ray Spectroscopy

TGA Thermogravimetric Analysis

XPS X-ray Photoelectron Spectroscopy

Symbols

p₀₂ Oxygen Partial Pressure (bar)
L Membrane Thickness (mm)

L_c Characteristic Membrane Thickness (mm)

k_s Surface Exchange Reaction Coefficient (cm·s⁻¹)

 $\begin{array}{ccc} D_s & & Self\mbox{-diffusion Coefficient } (cm^2 \cdot s^{\text{-}1}) \\ R & & Ideal\mbox{ Gas Constant } (8.314\mbox{ J}\mbox{-mol}^{\text{-}1}\mbox{-}K^{\text{-}1}) \\ F & & Faraday\mbox{ Constant } (96\mbox{ 485.309 C mol}^{\text{-}1}) \end{array}$

T Membrane Temperature (K or °C)

σ Conductivity (S·cm⁻¹)

jo2 Oxygen Flux (mL·cm⁻²·min⁻¹)

m Mass (g)

E_a Activation Energy (kJ·mol⁻¹)

Chapter 1

1. Introduction

1.1 Oxygen separation

The most established technology for oxygen production is cryogenic air distillation in the industry, which can generate up to 30,000 m³·h⁻¹ of oxygen with a purity exceeding 95% [1, 2]. This technology requires high vacuum conditions and cryogenic temperatures to separate oxygen from air. The whole process is complex and energy-intensive, primarily due to the closely spaced boiling points of O₂ and N₂ (-183 °C for O₂ and -196 °C for N₂) and the extremely low temperatures required for the operation. It demands approximately 225 kWh per ton of energy [3]. Despite this, it has been continuously refined over the past century, making it the optimal choice for large-scale oxygen production [1]. However, oxygen production is equally critical for small- and medium-scale applications, leading to the development of various alternative technologies such as pressure and temperature swing adsorption, chemical looping, oxygen transport membranes (OTMs), etc. [2].

Pressure and temperature swing adsorption rely on the differing polarizability of air components. Nitrogen (N₂), being more polarizable than oxygen (O₂), is selectively absorbed by an adsorbent material. The technology operates under mild conditions, with temperatures below 150 °C and atmospheric pressure. Since the process is physical adsorption, the adsorbents can be easily regenerated by adjusting the temperature or pressure. However, achieving high-purity oxygen requires large amounts of adsorbents. This limitation poses challenges for high-purity oxygen production.

Chemical looping, on the other hand, extracts pure oxygen by reducing inorganic materials at high temperatures (usually above 1200 °C). Materials with redox properties are reduced and then release oxygen. The unique advantage of this technology is the subsequent step in the cycle, where the reduced materials are re-oxidized using CO₂ and/or H₂O, generating hydrogen

or syngas as valuable byproducts. However, chemical looping operates at extremely high temperatures, resulting in significant energy consumption.

Another attractive approach for oxygen production is the use of oxygen transport membranes (OTMs), which are prepared by dense ceramic materials with ionic and/or electronic conductivity properties. These membranes present a promising alternative to traditional methods, with the potential to reduce production costs by up to 35% compared to cryogenic distillation [4, 5]. Oxygen is produced as a result of a driving force generated by either an electrical potential or an oxygen concentration gradient across the membranes. Since the material's conductivity properties improve at high temperatures, OTMs typically operate within a temperature range of 700 °C to 1000 °C. Although the technology is still in the developmental stage for large-scale applications, it shows great promise for medium- and small-scale oxygen production in the future.

CO₂, a significant greenhouse gas, contributes to climate change by elevating global temperatures as its atmospheric concentration rises [6]. This escalation can disrupt the planet's natural ecosystems, leading to accelerated polar ice cap melting, rising sea levels, expanded desertification, intensified extreme weather events, and other severe consequences [7]. The CO₂ emissions have been on the rise since the Industrial Revolution, from 2.84 billion tons in 1850 to 41.42 billion tons in 2023 (Figure 1.1) [8]. In industry, CO₂ emissions primarily arise from combustion processes. To reduce greenhouse gas emissions, advancing carbon capture and storage (CCS) technologies is essential [1, 9]. The CCS generally can be categorized by type of capture into three types in power plants: post-combustion, pre-combustion, and oxycombustion [10].

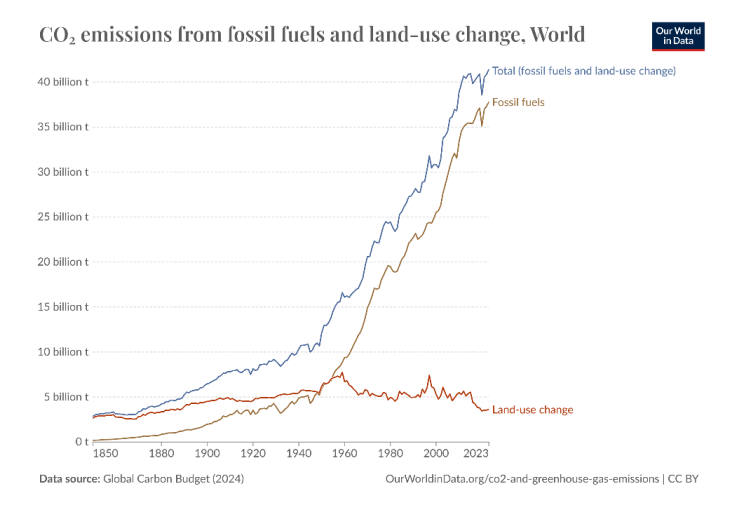


Figure 1.1 CO₂ emissions from fossil fuels and land-use change, World

Among these, post-combustion CCS is considered the most mature strategy. Various technologies have been developed according to different CO₂ concentrations and the presence of contaminants in the targeted streams. The most commonly utilized methods include physical adsorption, chemical absorption, membrane separation, and cryogenic distillation. In the case of the pre-combustion strategy, the fundamental approach involves removing carbon before the combustion process. However, the reactions included in the process are challenging to implement on an industrial scale due to the variety and volume of fuels used. Oxy-combustion has recently regained attention as a promising alternative to traditional combustion processes due to its higher efficiency. In addition, this method can make it easier to capture CO₂ from exhaust streams than conventional combustion methods [2].

By using pure O₂ instead of air, the oxy-combustion process eliminates N₂, resulting in an exhaust stream primarily composed of CO₂ and H₂O. This allows for straightforward CO₂ separation through condensation, simplifying the capture process and significantly reducing NO_x formation [11]. A critical challenge in oxy-combustion strategies is the efficient production of pure oxygen. Developing and improving air separation units (ASUs) is essential to make the generation of pure oxygen more cost-effective and energy-efficient, thereby enhancing the viability of this technology. Therefore, OTMs have garnered significant research attention owing to their ability to achieve high-purity oxygen production and energy-efficient

air separation, offering a sustainable alternative to conventional cryogenic or adsorption-based methods.

1.2 Application in membrane reactors

One of the key applications of OTMs is in catalytic membrane reactors (CMRs) to facilitate various chemical reactions [12-14]. CMRs can simultaneously combine gas separation and chemical reactions in a single step. During operation, OTMs function as selective barriers, allowing oxygen molecules to pass through while blocking nitrogen [15]. By combining separation and reaction, this approach creates synergies between the two processes, providing multiple benefits such as reduced pollution, environmentally sustainable chemistry, lower energy consumption, and higher selectivity as well as separation efficiency. CMRs have been investigated for various important applications, including oxidative coupling of methane (OCM), partial oxidation of methane (POM), oxidative dehydrogenation of ethane (ODHE), water splitting, oxy-combustion, and others [13, 16-19].

The OCM is a high-temperature reaction, typically conducted at 750–950 °C. The reaction can directly convert natural gas (CH₄) into value-added chemicals, like olefins. There are three main reactions in the process: the desired formation of ethylene (equation 1.1) and the undesired combustion reactions (equations 1.2 and 1.3). The complexity of OCM arises from the competition between these primary reactions and subsequent secondary reactions. Due to the significant impact of unwanted side reactions, the conventional OCM process struggles with the typical selectivity-conversion trade-off in consecutive reactions, often leading to suboptimal performance and limiting its scalability for industrial applications [20].

$$CH_4 + \frac{1}{2}O_2 \rightarrow \frac{1}{2}C_2H_4 + H_2O$$
 (1.1)

$$CH_4 + 2O_2 \rightarrow CO_2 + 2H_2O$$
 (1.2)

$$CH_4 + O_2 \rightarrow CO + H_2O + H_2 \tag{1.3}$$

POM is used to produce syngas (equation (1.4)). The process is less exothermic than commonly used technologies for syngas production in the industry, such as steam reforming and dry

reforming. In addition, the H₂/CO (2:1) ratio produced by POM is ideal for further chemical production in the industry. The operation temperature of the process is usually between 700 and 950 °C. Ni-based materials are usually applied as catalysts. Unlike OCM, the use of OTMs in POM membrane reactors cannot improve conversion or yield. However, OTMs can serve as an alternative to energy-intensive air separation units by supplying pure oxygen to the reactor, preventing N₂ dilution in high-pressure downstream processes and facilitating the conversion of syngas into valuable chemicals. The integration of an oxygen membrane enables substantial energy savings, enhancing overall process efficiency [21].

$$CH_4 + \frac{1}{2}O_2 \to CO + 2H_2$$
 (1.4)

The ODHE is a process for ethylene production [22]. Like OCM, the desired dehydrogenation reaction (equation (1.5)) is hindered by parallel and consecutive combustion reactions (equations (1.6) and (1.7)). The incorporation of membranes into the process provides benefits similar to those observed in the OCM process. By keeping oxygen partial pressures low, the desired reaction is promoted, leading to improved C₂H₄ selectivity through more efficient oxygen distribution. Additionally, heat management is enhanced as the exothermic reaction's heat release is more evenly dispersed. Moreover, the controlled oxygen supply ensures operation within safe explosive limits by maintaining very low local oxygen concentrations.

$$C_2H_6 + \frac{1}{2}O_2 \rightarrow C_2H_4 + H_2O$$
 (1.5)

$$C_2H_6 + \frac{7}{2}O_2 \to 2CO_2 + 3H_2O$$
 (1.6)

$$C_2H_4 + 3O_2 \rightarrow 2CO_2 + 2H_2O$$
 (1.7)

OTMs can also be utilized for hydrogen production via water splitting process. Since water dissociation is a thermodynamic equilibrium process, the equilibrium constant remains low at the operating temperatures of OTMs. However, by continuously removing the generated oxygen, the reaction can be shifted toward hydrogen production [23].

$$2H_2O \rightarrow 2H_2 + O_2 \tag{1.8}$$

The application of OTMs into oxy-combustion processes (equations (1.9) and (1.10)) has

shown significant potential, consistently enhancing process efficiency through in-situ air separation [13]. However, to ensure the economic feasibility of these membrane reactor systems, further improvements are required in oxygen flux and membrane stability for long-term operation.

$$CH_4 + 2O_2 \rightarrow CO_2 + 2H_2O$$
 (1.9)

$$C_{y}H_{y} + O_{2} \to CO_{2} + H_{2}O$$
 (1.10)

1.3 Mixed ionic and electronic conductors (MIEC)

Mixed ionic and electronic conductors (MIEC) show great potential for use as OTMs. In MIEC dense membranes, oxygen can be transported through crystal defects, such as interstitial oxygen, electronic defects, and oxygen vacancies. The oxygen transport capability is influenced by both ionic and electronic conductivities, which are affected by different factors. Electronic conductivity is primarily determined by the bandgap, while ionic conductivity depends mainly on the crystal structure [24]. Additionally, membrane performance is significantly affected by temperature and oxygen partial pressure. By utilizing MIEC dense membranes, oxygen purity can exceed 99.99% [3, 25].

1.3.1 Single phase materials for OTMs

Perovskite-based compounds ABO₃ are a typical type of MIEC used for oxygen transport. There are two equivalent ways to represent the perovskite unit cell [26]. In the first, as shown in Figure 1.2 (a), the A-site cation is located at the center of the cube, the B-site cations occupy the cube's corners, and oxygen atoms are positioned at the face centers. In the second, as depicted in Figure 1.2 (b), the B-site cation is at the center, A-site cations are at the cube's corners, and oxygen atoms reside at the edge centers. These two representations are interchangeable. In an ideal cubic perovskite structure, the B-site cation is coordinated by six oxygen atoms, forming an octahedron, while the A-site cation is in a 12-fold cuboctahedral coordination [27, 28]. A key advantage of the cubic perovskite structure is its ability to accommodate various cations with different valences, enabling doping at either the A- or B-

site to alter the oxygen stoichiometry. This, in turn, promotes the formation of oxygen vacancies and electron holes, which are essential for achieving the desired MIEC behavior [29]. Generally, the ionic/electronic conductivity of perovskites can be modified by doping the Asite with lanthanides or alkaline earth elements and adjusting the B-site composition with different metals. This flexibility allows for tailored transport properties.

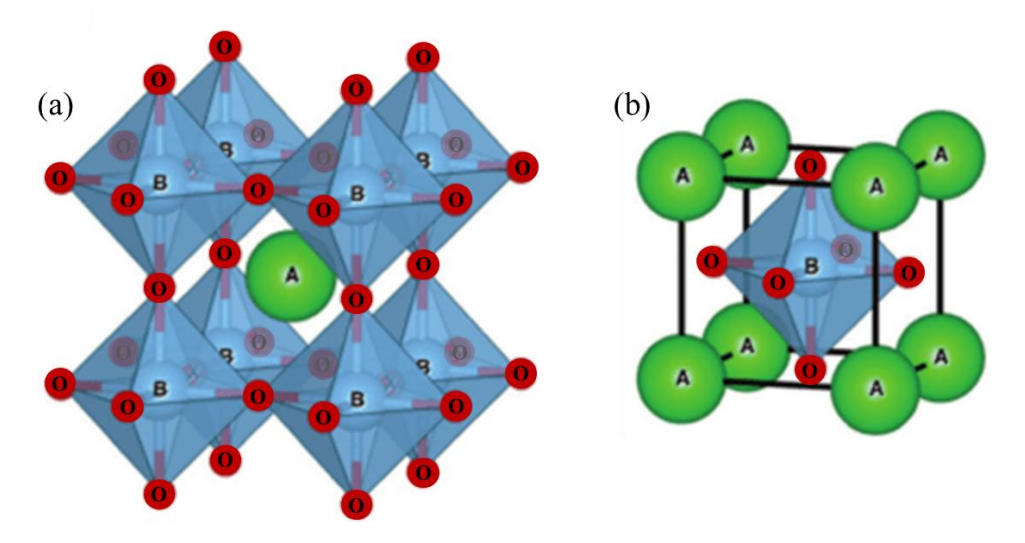


Figure 1.2 (a) A cation (b) B cation as an individual center in ideal cubic perovskite structure

ABO3

The first OTMs were reported in 1985 by Teraoka et al. and were based on perovskite crystal structures (ABO₃) [30]. Among the studied materials, SrCo_{0.8}Fe_{0.2}O_{3.δ} exhibited the highest oxygen permeation, paving the way for further exploration of OTMs using ceramic materials. In the following years, researchers continued to advance this technology, expanding the understanding and application of ceramic-based OTMs.

Perovskite based on SrFeO_{3- δ} and SrCoO_{3- δ} based perovskite materials with A/B site substitutions have been extensively investigated [31-37]. Among them, the La_{1-x}Sr_xCo_yFe_{1-y}O_{3- δ} series (LSCF), SrCo_{0.8}Fe_{0.2}O_{3- δ} as well as Ba_{0.5}Sr_{0.5}Co_{0.8}Fe_{0.2}O_{3- δ} (BSCF) have been reported to exhibit high oxygen permeation rates. However, these materials were unstable under low oxygen partial pressures [38, 39] and aggressive gases such as CO, CH₄ and CO₂ [40] as they tended to decompose from a cubic perovskite structure into an orthorhombic brownmillerite phase. In recent years, various efforts have been made to enhance

the stability of perovskites through element doping. One of the most notable approaches involved doping the A-site with lanthanides such as La, Pr, etc. [41, 42].

In addition, B-site doping with elements such as Al, Zr, Nb, Ti, and Y has been also explored to enhance stability [43-49]. While these strategies have shown some success, the high Co and Fe content in the B-site still limits resistance to reducing environments. In contrast, perovskite material SrTiO₃ is chemically and structurally stable but inherently oxygen-impermeable. However, B-site Ti⁴⁺ can be replaced by lower-valence metal cations, such as Fe³⁺[50-53], $Co^{2+}[54, 55]$, $Al^{3+}[56, 57]$, $Mg^{2+}[58]$ and $Ni^{2+}[59, 60]$, to enhance oxygen permeability. In practice, Fe and Co are preferred as B-site dopants since these cations readily reduce, promoting the formation of oxygen vacancies. Introducing a controlled amount of multivalent Fe/Co into the TiO₆ sublattice generates oxygen vacancies and electron holes, leading to an oxygen permeation rate comparable to that of LSCF [50, 54]. Ruddlesden-Popper (A₂BO₄) phases are also MIECs with high oxygen transport capacity [61, 62]. Their exceptional oxygen diffusion properties stem from interstitial oxygen transport rather than oxygen vacancies [63, 64]. However, these materials are unstable under CO₂ and varying atmospheric conditions, particularly within an oxygen partial pressure range of 10⁻¹ to 10⁻²⁰ bar on both sides of the membrane [62, 65, 66]. Despite these challenges, they are promising candidates for air electrodes in solid oxide fuel cells (SOFCs) [67]

1.3.2 Dual phase materials for OTMs

Given that perovskite-based OTMs often lack long-term stability under operating conditions, dual-phase materials have been extensively studied to address the limitations of single-phase systems. These composites are engineered to improve chemical and mechanical stability by combining ion-conducting and electron-conducting phases, each forming a continuous network that enables different transport mechanisms.

For the ionic-conducting phase, doped zirconia or ceria materials with a cubic fluorite crystal structure are often applied, which are stable in CO₂ atmospheres. The ionic conductivity of these materials is influenced by the specific composition of the lattice. Yttria-stabilized zirconia (YSZ) and scandium-doped zirconia (ScSZ) are the most widely used doped zirconia materials

[68-70]. The most attractive ceria materials are doped with gadolinium (CGO) or samarium (CSO) [71, 72]. For the electron-conducting phase, materials with perovskites crystal structures are the most commonly used [73, 74]. Their oxide structures can function as pure electronic semiconductors. A dual-phase system with La_{0.8}Sr_{0.2}MnO_{3-δ} (LSM) as the electron-conducting phase is one of the most studied formulations [75]. However, many of these materials face stability issues under CO₂ atmospheres during long-term operation [73, 76, 77]. Conversely, Ruddlesden-Popper materials can remain stable in CO₂ environments. However, they are prone to degradation in oxygen-deficient conditions [65]. Spinels (MM'₂O₄) are another widely used material class serving as the electron-conducting phase in dual-phase membranes, which are stable in CO₂ condition but fragile in reducing atmospheres [78, 79].

1.3.3 Material selection

Perovskite-structured oxygen transport membranes hold great potential for the energy-efficient separation of pure oxygen from air. This process typically occurs under relatively mild conditions (e.g., air/Ar), allowing for the use of a variety of materials with high oxygen permeability. In contrast, membrane reactors usually operate under much more severe environments—such as exposure to CO, CO₂, H₂, and CH₄ at high temperatures of approximately 800-900 °C-making material stability a key consideration in their design and application. Although many materials have demonstrated excellent oxygen permeation performance, their industrial deployment in membrane reactors remains limited. This is primarily due to insufficient material stability, which hinders long-term operation under harsh reducing and/or corrosive conditions. Preliminary studies suggest that strontium titanate SrTiO₃ is a promising candidate for membrane reactors due to its superior chemical and mechanical stability in harsh environments. However, its electronic and ionic conductivity remains negligible over a wide range of temperatures and oxygen partial pressures. To enhance conductivity, a B-site doping strategy is employed. The research focuses on developing SrTiO₃-based materials by substituting a portion of titanium with redox-active transition metals to obtain both sufficient oxygen permeability and strong chemical stability. The structural integrity of these materials is assessed using the tolerance factor (t), which defines A/B-site cation sizes range that can be accommodated while maintaining the perovskite structure [12]. In perovskite oxides, a tolerance factor of 1 corresponds to an ideal cubic structure, while deviations from this value indicate mismatches in A-O and B-O bond lengths. A perovskite structure can generally exist within a tolerance factor range of 0.75 to 1. Based on tolerance factor calculations, Fe, Ni, and similar redox-active elements, as well as less redox-active elements like Mg and Al, are selected for B-site doping in SrTiO₃ for this work. The substitution of Ti with these elements introduces mixed ionic and electronic conductivity, enhancing the material's functionality. Among them, Ni is particularly promising due to its strong catalytic properties—Ni-based catalysts can achieve over 95% CH₄ conversion and more than 96% syngas selectivity. Additionally, in-situ exsolution of catalytically active metallic nanoparticles, such as Ni, from the perovskite lattice has been reported [59]. Therefore, Ni is incorporated not only to improve conductivity but also to enhance catalytic performance.

1.4 Oxygen transport mechanism

Currently, OTMs are categorized into two main configurations: symmetric and asymmetric. Between the two, asymmetric OTMs demonstrate superior performance. An asymmetric membrane assembly typically consists of two layers (Figure 1.3): a dense membrane layer for oxygen separation, and a porous support layer, which is made from the same material as the dense membrane and provides mechanical stability.

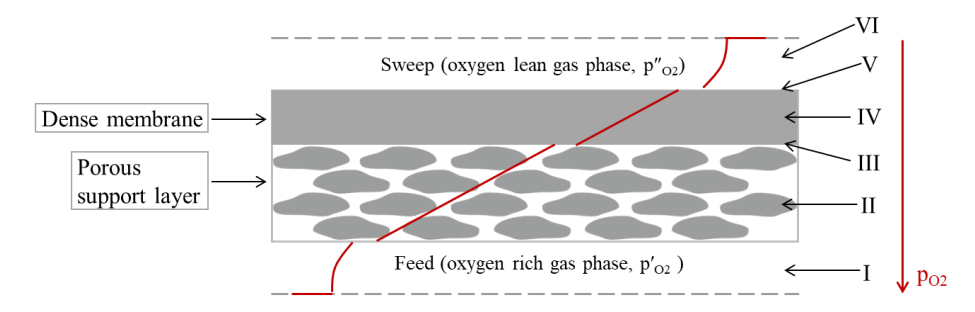


Figure 1.3 Oxygen partial pressure distribution (po2) across the asymmetric membrane

Oxygen transport through MIEC asymmetric membranes involves multiple mechanisms, including gas-phase diffusion, gas transport through porous media, surface exchange, and bulk diffusion [37]. The partial pressure gradient across the membranes is the driving force in this case, which facilitates ion diffusion and enhances oxygen surface exchange. During this process, O₂ molecules transition from the oxygen-rich gas phase and incorporate into oxygen vacancies in the materials. At the same time, electrons migrate via polaron transport, resulting in a pure oxygen flux. These membranes are usually operated at high temperatures (above 700 °C), as ion diffusion is a temperature-dependent process. Each transport mechanism can become the limiting step for oxygen permeation. Therefore, understanding the fundamental principles of each transport process is essential. Figure 1.2 illustrates the distribution of oxygen partial pressure distribution (po₂) across the asymmetric membrane.

- •Process I: oxygen molecules move through the feed gas phase, where concentration polarization can reduce p_{02} .
- Process II: oxygen transport through the porous support layer.
- Process III: surface exchange reaction. Oxygen molecules ionize and dissociate to oxygen ions according to equation (1.11).

$$\frac{1}{2}O_2 + V_O^{\circ} \longrightarrow O_O^{\times} + 2h^{\circ}$$
 (1.11)

where subscripts V_O^* , O_O^* and h^* represents an oxygen vacancy, an oxygen ion occupying an oxygen lattice site, and an electron hole, respectively. The superscripts \times and \cdot denote an electroneutral state and one positive effective charge, respectively.

- Process IV: the bulk diffusion process. Oxygen ions diffuse through the dense membrane via oxygen vacancies or other defects within the membrane, driven by the pressure gradient between the feed and permeate side. Simultaneously, electrons transport in the opposite direction to maintain electrical neutrality.
- Process V: surface exchange reaction. Oxygen ions associate with oxygen molecules based on equation (1.12).

$$O_0^{\times} + 2h \longrightarrow \frac{1}{2}O_2 + V_0^{-} \tag{1.12}$$

• Process VI: concentration polarization can reduce p_{O2} during oxygen molecules move through sweep gas phase [80].

Oxygen transport is generally limited by either surface exchange reactions or bulk diffusion, depending on the membrane thickness (L). The key distinction between both limiting steps is the characteristic membrane thickness (L_c), which can be determined by the surface exchange reaction coefficient (k_s) and the self-diffusion coefficient (D_s), as expressed in equation 1.13. These parameters, k_s and D_s can be obtained through experimental methods like O^{18} - O^{16} isotopic exchange and conductivity relaxation [81-83].

$$L_C = \frac{D_s}{k_s} \tag{1.13}$$

If $L \gg L_c$, the transport is assumed to be only limited by bulk diffusion. The oxygen flux in dense membranes is commonly described using a well-established model based on Wagner's theory, which is typically expressed in the form of the standard Wagner equation [24, 84]:

$$j(O_2) = \frac{R \cdot T}{16F^2 \cdot L} \cdot \int_{\ln p^* o_2}^{\ln p^* o_2} \sigma_{amb} \cdot d \ln p_{O_2}$$
 (1.14)

where R corresponds to the ideal gas constant, F is the Faraday constant, L is the thickness of the membrane, T is the membrane temperature, p'_{o_2} and p''_{o_2} are the oxygen partial pressure of oxygen-rich and oxygen-lean side, respectively, and σ_{amb} is the ambipolar conductivity, given by equation (1.15):

$$\sigma_{amb} = \frac{\sigma_i \cdot \sigma_e}{\sigma_i + \sigma_e} \tag{1.15}$$

In the MIEC, if $\sigma_e >> \sigma_i$, $\sigma_{amb} \approx \sigma_i$.

According to the article published by Koros et al. [85], permeance is defined as 'transport flux per unit transmembrane driving force', and its unit is usually expressed in mol·cm⁻²·s⁻¹·Pa⁻¹ for porous materials.

In our case, the driving force, as shown in equation (1.16), is unitless.

$$\ln p'_{O_2} - \ln p''_{O_2} = \ln \frac{p'_{O_2}}{p''_{O_2}}$$
 (1.16)

Consequently, the oxygen permeance can be expressed as shown in equation (1.17). In this

formulation, the unit of permeance becomes identical to that of the oxygen flux, $j(O_2)$, $mol \cdot cm^{-2} \cdot s^{-1}$, which often leads to confusion.

$$Permeance = \frac{j(O_2)}{\ln \frac{p'_{O_2}}{p''_{O_2}}} = \frac{R}{16F^2 \cdot L} \cdot T \cdot \sigma_{amb}$$
 (1.17)

Permeability coefficient is defined as 'transport flux per unit transmembrane driving force per unit membrane thickness' [85], as expressed in equation (1.18):

$$Permeability = \frac{R}{16F^2} \cdot T \cdot \sigma_{amb}$$
 (1.18)

On the other hand, if $L < L_c$, surface exchange reactions dominate the process. Unlike bulk diffusion, surface exchange reactions exhibit distinct behavior, influenced by multiple factors such as surface-active sites, gas flux, the surface characteristics of the mixed ionic-electronic conductor (MIEC), gas properties, oxygen partial pressure and temperature. As a result, the oxygen flux $j(O_2)$ can be calculated according to the following equation (1.19) [86]:

$$j(O_2) = \frac{R \cdot T}{16F^2} \cdot \frac{1}{L + 2L_c} \cdot \sigma_{amb} \cdot \ln \frac{p'_{O_2}}{p''_{O_2}}$$
(1.19)

In order to achieve a high oxygen flux, various strategies have been explored to enhance the surface exchange reaction. Studies have shown that applying a porous top coating made of the same material as dense membranes can significantly enhance surface exchange permeation by increasing the surface-to-volume ratio [87]. Additionally, other approaches include applying a porous coating made of high surface exchange materials and further modifying the porous surface with catalytically active nanoparticles [88]. Moreover, coating membrane surfaces with ultrafine grains has been utilized to enhance permeation, as a higher grain boundary density has been found to promote oxygen incorporation and improve surface exchange reactions [24, 82, 89].

1.5 Scope of the thesis.

MIEC ceramics exhibit great potential as OTMs, enabling both the efficient separation of highpurity oxygen from air and the integration of chemical reactions within membrane reactors. Given that most membrane reactors operate under reducing atmospheres, ensuring the chemical and structural stability of the membrane materials is essential for sustained performance and durability.

Given SrTiO3's exceptional stability, this thesis primarily focuses on investigating SrTiO3based materials for use as oxygen transport membranes in membrane reactors, where the operating conditions typically involve exposure to reducing gases. These reactors are designed to facilitate the efficient transport of oxygen while combining chemical reactions, making the development of stable and highly permeable membranes essential. To achieve this, powder mixtures are synthesized through the solid-state reaction method, utilizing raw powders directly sourced from commercial suppliers. After synthesis, the powders are sintered into dense target membranes, ensuring the proper structure for optimal functionality. The main objective of this work is to strike an optimal balance between the material's stability and oxygen permeability, which is crucial for enhancing the performance of membrane reactors. This is achieved by carefully optimizing the doping of various elements in the B-site of the SrTiO₃ material in this work. The choice of doping elements plays an important role in modifying the perovskite structure and consequently influencing its properties. These doping elements can either enhance or hinder the material's ability to conduct oxygen ions or electrons, so their selection is critical for achieving the desired membrane performance. The microstructures of the synthesized materials are characterized and analyzed via different methods. Additionally, their electrical and ionic conductivity, oxygen permeability, and stability under operating conditions are assessed to gain insight into the material's overall performance, identifying potential weaknesses or areas for improvement. Furthermore, the performance of these materials in membrane reactors is systematically assessed to determine their efficiency in target applications. Through this approach, the thesis aims to contribute to the development of high-performance oxygen transport membranes that are both stable and efficient for use in membrane reactors operating under challenging conditions.

Fe and Ni co-doped SrTi_{0.65-x}Fe_{0.35}Ni_xO_{3-δ} (x=0, 0.05, 0.075, 0.1) (STFN_x) materials are discussed in **Chapter 2**. The Ni-free material SrTi_{0.65}Fe_{0.35}O_{3-δ} is sintered at 1400 °C, whereas the others are sintered at 1350 °C. The material compositions are confirmed by inductively coupled plasma atomic emission spectroscopy (ICP-OES). All aspects including particle size distribution (PSD), X-ray diffraction (XRD), scanning electron microscopy (SEM) of both the

surface and cross section, electrical and ionic conductivity, oxygen permeability are discussed. Additionally, thermo-chemical stability is assessed through annealing experiments in both 2.9 vol% H₂/Ar and syngas conditions as well as thermogravimetric analysis (TGA). Furthermore, the Ni/Fe exsolution phenomenon on the STFN materials' surface is also explored in this part.

In **Chapter 3**, the effect of pure Ni doping in STO₃ materials is discussed. The microstructure features and functional prosperities of the synthesized Zr and Ni co-doped SrTi_{0.95-x}Zr_{0.05}Ni_xO_{3-δ} (x=0.01, 0.03, 0.05, 0.10, 0.15) (STZN_x) membranes are characterized and tested. Zr is incorporated to minimize cation mismatch and stabilize the cubic structure. The solubility limit of Ni in the perovskite is revealed by XRD. X-ray photoelectron spectroscopy (XPS) is applied to investigate the valance of Ni in the structure. The oxygen permeation measurements are conducted in air and pure O₂ at the feed side, respectively. Thermochemical stability tests are carried out by annealing samples in 2.9 vol% H₂/Ar and TGA measurement in reducing atmospheres. Like STFN_x, the presence of Ni exsolution particles on the surface is observed via SEM.

The effects of Mg and Al doping on the structural, sintering, and oxygen permeation properties of SrTi_{0.65}Fe_{0.35}O_{3-δ} (STF35) membrane are investigated in **Chapter 4.** A series of Al- and Mg-doped STF35 materials SrTi_{0.65-x}Fe_{0.35}Al_xO_{3-δ} (x=0.01, 0.03, 0.05, 0.10, 0.15) (STFA_x) and SrTi_{0.65-x}Fe_{0.35}Mg_xO_{3-δ} (x=0.01, 0.03, 0.05, 0.10) (STFM_x) are synthesized using the solid-state reaction method. The structural characteristics of these materials are examined through XRD analysis, which is used to determine phase composition, lattice parameter, and the solubility limits of Al and Mg within the perovskite lattice. The oxygen permeability of STFA_x and STFM_x are systematically evaluated to understand how Al and Mg doping influences oxygen transport through the membrane. The oxygen concentration changes in STFM_x series are analyzed using thermogravimetric analysis. Additionally, the sintering behavior of STFM_x is studied through the analysis of SEM images of cross section.

In **Chapter 5**, the performance of selected materials in membrane reactors is evaluated. A series B-site doped SrTiO₃ materials SrTi_{0.60}Fe_{0.35}Ni_{0.05}O_{3- δ} (STFN005), SrTi_{0.75}Fe_{0.25}O_{3- δ} (STF25), SrTi_{0.65}Fe_{0.35}O_{3- δ} (STF35) and SrTi_{0.85}Zr_{0.05}Ni_{0.10}O_{3- δ} (STZN10) were synthesized and subjected to high-temperature sintering (1350/1400°C) to fabricate dense membranes. To

enhance surface exchange kinetics and overall oxygen transport efficiency, STF25 and STF35 membranes were further modified with porous STFN005 catalytic layers on the both sides, yielding STF25_cl and STF35_cl, respectively. Oxygen permeability are studies under different conditions, including air/Ar, air/10 vol% CH4 and 15 vol% CO2/10 vol% CH4 atmospheres. The microstructure is assessed following the completion of all tests. Additionally, CH4 conversion rates and product selectivity are calculated in air/10 vol% CH4 condition.

Finally, **Chapter 6** provides an in-depth discussion of the significance of the overall findings. It also presents insightful recommendations for future research, highlighting potential directions and key areas for further exploration.

REFERENCES

- [1] R.J. Allam, Improved oxygen production technologies, Energy Procedia 1(1) (2009) 461-470.
- [2] F. Wu, M. Argyle, P. Dellenback, M. Fan, Progress in O2 separation for oxy-fuel combustion—A promising way for cost-effective CO2 capture: A review, Progress in Energy and Combustion Science 67 (2018).
- [3] R. Kiebach, S. Pirou, L. Martinez Aguilera, A.B. Haugen, A. Kaiser, P.V. Hendriksen, M. Balaguer, J. García-Fayos, J.M. Serra, F. Schulze-Küppers, M. Christie, L. Fischer, W.A. Meulenberg, S. Baumann, A review on dual-phase oxygen transport membranes: from fundamentals to commercial deployment, Journal of Materials Chemistry A 10(5) (2022) 2152-2195.
- [4] S. Smart, C.X.C. Lin, L. Ding, K. Thambimuthu, J.C. Diniz da Costa, Ceramic membranes for gas processing in coal gasification, Energy & Environmental Science 3(3) (2010) 268-278.
- [5] A. Leo, S. Liu, J.C.D.d. Costa, Review, International Journal of Greenhouse Gas Control 3(4) (2009) 357-367.
- [6] M. Harmsen, C. Tabak, L. Höglund-Isaksson, F. Humpenöder, P. Purohit, D. van Vuuren, Uncertainty in non-CO2 greenhouse gas mitigation contributes to ambiguity in global climate policy feasibility, Nature Communications 14(1) (2023) 2949.
- [7] Y.-H. Kim, S.-K. Min, N.P. Gillett, D. Notz, E. Malinina, Observationally-constrained projections of an ice-free Arctic even under a low emission scenario, Nature Communications 14(1) (2023) 3139.
- [8] G.C.B.w.m.p.b.O.W.i. Data, "Fossil fuels GCB" [dataset]. Global Carbon Project, "Global Carbon Budget" [original data]. 2024. https://ourworldindata.org/co2-emissions.
- [9] N.F. Himma, A.K. Wardani, N. Prasetya, P.T.P. Aryanti, I.G. Wenten, Recent progress and challenges in membrane-based O2/N2 separation, 35(5) (2019) 591-625.
- [10] B. Dziejarski, R. Krzyżyńska, K. Andersson, Current status of carbon capture, utilization, and storage technologies in the global economy: A survey of technical assessment, Fuel 342 (2023) 127776.
- [11] B.J.P. Buhre, L.K. Elliott, C.D. Sheng, R.P. Gupta, T.F. Wall, Oxy-fuel combustion

- technology for coal-fired power generation, Progress in Energy and Combustion Science 31(4) (2005) 283-307.
- [12] J. Sunarso, S.S. Hashim, N. Zhu, W. Zhou, Perovskite oxides applications in high temperature oxygen separation, solid oxide fuel cell and membrane reactor: A review, Progress in Energy and Combustion Science 61 (2017) 57-77.
- [13] F. Schulze-Küppers, F. Drago, L. Ferravante, S. Herzog, S. Baumann, P. Pinacci, W.A. Meulenberg, Design and fabrication of large-sized planar oxygen transport membrane components for direct integration in oxy-combustion processes, Separation and Purification Technology 220 (2019) 89-101.
- [14] G. Zhang, W. Jin, N. Xu, Design and Fabrication of Ceramic Catalytic Membrane Reactors for Green Chemical Engineering Applications, Engineering 4(6) (2018) 848-860.
- [15] W. Deibert, M.E. Ivanova, S. Baumann, O. Guillon, W.A. Meulenberg, Ion-conducting ceramic membrane reactors for high-temperature applications, Journal of Membrane Science 543 (2017) 79-97.
- [16] J. Garcia-Fayos, M.P. Lobera, M. Balaguer, J.M. Serra, Catalyst Screening for Oxidative Coupling of Methane Integrated in Membrane Reactors, Frontiers in Materials 5 (2018).
- [17] H. Wang, Y. Cong, W. Yang, Investigation on the partial oxidation of methane to syngas in a tubular Ba0.5Sr0.5Co0.8Fe0.2O3-δ membrane reactor, Catalysis Today 82(1) (2003) 157-166.
- [18] R. Schucker, G. Dimitrakopoulos, K. Derrickson, K. Kopec, F. Al-Ahmadi, J. Johnson, L. Shao, A. Ghoniem, Oxidative Dehydrogenation of Ethane to Ethylene in an Oxygen Ion Transport Membrane Reactor A Proposed Design for Process Intensification, Industrial & Engineering Chemistry Research 58 (2019).
- [19] Z. Cao, H. Jiang, H. Luo, S. Baumann, W.A. Meulenberg, H. Voss, J. Caro, Simultaneous overcome of the equilibrium limitations in BSCF oxygen-permeable membrane reactors: Water splitting and methane coupling, Catalysis Today 193(1) (2012) 2-7.
- [20] A. Cruellas, T. Melchiori, F. Gallucci, M. van Sint Annaland, Advanced reactor concepts for oxidative coupling of methane, Catalysis Reviews 59(3) (2017) 234-294.
- [21] A.P.E. York, T. Xiao, M.L.H. Green, Brief Overview of the Partial Oxidation of Methane to Synthesis Gas, Topics in Catalysis 22 (2003) 345-358.

- [22] M.L. Rodriguez, D.E. Ardissone, E. Heracleous, A.A. Lemonidou, E. López, M.N. Pedernera, D.O. Borio, Oxidative dehydrogenation of ethane to ethylene in a membrane reactor: A theoretical study, Catalysis Today 157(1) (2010) 303-309.
- [23] G. He, Y. Ling, H. Jiang, A. Toghan, Barium Titanate as a Highly Stable Oxygen Permeable Membrane Reactor for Hydrogen Production from Thermal Water Splitting, ACS Sustainable Chemistry & Engineering 9(33) (2021) 11147-11154.
- [24] J. Sunarso, S. Baumann, J.M. Serra, W.A. Meulenberg, S. Liu, Y.S. Lin, J.C. Diniz da Costa, Mixed ionic–electronic conducting (MIEC) ceramic-based membranes for oxygen separation, Journal of Membrane Science 320(1-2) (2008) 13-41.
- [25] X. Zhu, W. Yang, Introduction to Mixed Ionic–Electronic Conducting Membranes, in: X. Zhu, W. Yang (Eds.), Mixed Conducting Ceramic Membranes: Fundamentals, Materials and Applications, Springer Berlin Heidelberg, Berlin, Heidelberg, 2017, pp. 1-10.
- [26] G. George, S.R. Ede, Z. Luo, Fundamentals of Perovskite Oxides: Synthesis, Structure, Properties and Applications, 2020.
- [27] N. Harre, D. Mercurio, G. Trolliard, B. Frit, Crystal structure of BaLa4Ti4O15, member n=5 of the homologous series (Ba, La)nTin-1O3n of cation-deficient perovskite-related compounds, Materials Research Bulletin 33(10) (1998) 1537-1548.
- [28] S. Liu, H. Luo, Y. Li, Q. Liu, J.-L. Luo, Structure-engineered electrocatalyst enables highly active and stable oxygen evolution reaction over layered perovskite LaSr3Co1.5Fe1.5O10-δ, Nano Energy 40 (2017) 115-121.
- [29] M. Burriel, C. Niedrig, W. Menesklou, S. Wagner, J. Santiso, E. Ivers-Tiffée, BSCF epitaxial thin films: Electrical transport and oxygen surface exchange, Solid State Ionics 181 (2010) 602-608.
- [30] Y. Teraoka, H.-M. Zhang, S. Furukawa, N. Yamazoe, OXYGEN PERMEATION THROUGH PEROVSKITE-TYPE OXIDES, Chemistry Letters 14(11) (1985) 1743-1746.
- [31] T. Nagai, W. Ito, T. Sakon, Relationship between cation substitution and stability of perovskite structure in SrCoO3–δ-based mixed conductors, Solid State Ionics 177(39) (2007) 3433-3444.
- [32] W. Chen, C.-s. Chen, H.J.M. Bouwmeester, A. Nijmeijer, L. Winnubst, Oxygen-selective membranes integrated with oxy-fuel combustion, Journal of Membrane Science 463 (2014)

166-172.

- [33] Y. Teraoka, T. Nobunaga, K. Okamoto, N. Miura, N. Yamazoe, Influence of constituent metal cations in substituted LaCoO3 on mixed conductivity and oxygen permeability, Solid State Ionics 48(3) (1991) 207-212.
- [34] L. Qiu, T.H. Lee, L.-M. Liu, Y.L. Yang, A.J. Jacobson, Oxygen permeation studies of SrCo0.8Fe0.2O3 δ, Solid State Ionics 76 (1995) 321-329.
- [35] Z. Shao, S.M. Haile, A high-performance cathode for the next generation of solid-oxide fuel cells, Nature 431(7005) (2004) 170-173.
- [36] C. Niedrig, S. Taufall, M. Burriel, W. Menesklou, S.F. Wagner, S. Baumann, E. Ivers-Tiffée, Thermal stability of the cubic phase in Ba0.5Sr0.5Co0.8Fe0.2O3-δ (BSCF), SOLID STATE IONICS 197(1) (2011) 25-31.
- [37] S. Baumann, J.M. Serra, M.P. Lobera, S. Escolástico, F. Schulze-Küppers, W.A. Meulenberg, Ultrahigh oxygen permeation flux through supported Ba0.5Sr0.5Co0.8Fe0.2O3-δ membranes, Journal of Membrane Science 377(1) (2011) 198-205.
- [38] M. Kuhn, S. Hashimoto, K. Sato, K. Yashiro, J. Mizusaki, Oxygen nonstoichiometry and thermo-chemical stability of La0.6Sr0.4CoO3-δ, Journal of Solid State Chemistry 197 (2013) 38-45.
- [39] J. Ovenstone, J.-I. Jung, J.S. White, D.D. Edwards, S.T. Misture, Phase stability of BSCF in low oxygen partial pressures, Journal of Solid State Chemistry France 181 (2008) 576-586.
- [40] M. Arnold, H. Wang, A. Feldhoff, Influence of CO2 on the Oxygen Permeation Performance and the Microstructure of Perovskite-Type (Ba0.5Sr0.5)(Co0.8Fe0.2)O3-?? Membranes, Journal of Membrane Science 293 (2007) 44-52.
- [41] G. Chen, W. Liu, M. Widenmeyer, P. Ying, M. Dou, W. Xie, C. Bubeck, L. Wang, M. Fyta, A. Feldhoff, A. Weidenkaff, High flux and CO2-resistance of La0.6Ca0.4Co1–xFexO3–δ oxygen-transporting membranes, Journal of Membrane Science 590 (2019) 117082.
- [42] K. Partovi, F. Liang, O. Ravkina, J. Caro, High-Flux Oxygen-Transporting Membrane Pr0.6Sr0.4Co0.5Fe0.5O3–δ: CO2 Stability and Microstructure, ACS Applied Materials & Interfaces 6(13) (2014) 10274-10282.
- [43] Z. Wu, W. Jin, N. Xu, Oxygen permeability and stability of Al2O3-doped

- SrCo0.8Fe0.2O3-δ mixed conducting oxides, Journal of Membrane Science 279(1-2) (2006) 320-327.
- [44] A.L. Shaula, V.V. Kharton, J.C. Waerenborgh, D.P. Rojas, E.V. Tsipis, N.P. Vyshatko, M.V. Patrakeev, F.M.B. Marques, Transport properties and Mössbauer spectra of Fe-substituted La10–x(Si,Al)6O26 apatites, Materials Research Bulletin 39(6) (2004) 763-773.
- [45] Y. Shen, F. Wang, X. Ma, T. He, SrCo 1-y Ti y O $3-\delta$ as potential cathode materials for intermediate-temperature solid oxide fuel cells, Lancet 196 (2011) 7420-7425.
- [46] O. Ravkina, T. Klande, A. Feldhoff, Investigation of Zr-doped BSCF perovskite membrane for oxygen separation in the intermediate temperature range, Journal of Solid State Chemistry 201 (2013) 101–106.
- [47] P. Haworth, S. Smart, J. Glasscock, J.C. Diniz da Costa, Yttrium doped BSCF membranes for oxygen separation, Separation and Purification Technology 81(1) (2011) 88-93.
- [48] L.-S. Unger, R. Ruhl, M. Meffert, C. Niedrig, W. Menesklou, S.F. Wagner, D. Gerthsen, H.J.M. Bouwmeester, E. Ivers-Tiffée, Yttrium doping of Ba 0.5 Sr 0.5 Co 0.8 Fe 0.2 O 3-δ part II: Influence on oxygen transport and phase stability, Journal of the European Ceramic Society 38(5) (2018) 2388-2395.
- [49] F. Wang, T. Nakamura, K. Yashiro, J. Mizusaki, K. Amezawa, Effect of Nb doping on the chemical stability of BSCF-based solid solutions, Solid State Ionics 262 (2014) 719-723.
- [50] F. Schulze-Küppers, S.F.P. ten Donkelaar, S. Baumann, P. Prigorodov, Y.J. Sohn, H.J.M. Bouwmeester, W.A. Meulenberg, O. Guillon, Structural and functional properties of $SrTi1-xFexO3-\delta$ ($0 \le x \le 1$) for the use as oxygen transport membrane, Separation and Purification Technology 147 (2015) 414-421.
- [51] V. Metlenko, W. Jung, S.R. Bishop, H.L. Tuller, R.A. De Souza, Oxygen diffusion and surface exchange in the mixed conducting oxides SrTi(1-y)Fe(y)O(3-delta), Physical chemistry chemical physics: PCCP 18(42) (2016) 29495-29505.
- [52] V.V. Kharton, A.V. Kovalevsky, A.P. Viskup, J.R. Jurado, F.M. Figueiredo, E.N. Naumovich, J.R. Frade, Transport Properties and Thermal Expansion of Sr0.97Ti1–FexO3–(x=0.2–0.8), Journal of Solid State Chemistry 156(2) (2001) 437-444.
- [53] W. Jung, H.L. Tuller, Impedance study of SrTi1-xFexO3 $-\delta$ (x=0.05 to 0.80) mixed ionic-electronic conducting model cathode, Solid State Ionics 180(11-13) (2009) 843-847.

- [54] Y. Liu, S. Baumann, F. Schulze-Küppers, D.N. Mueller, O. Guillon, Co and Fe co-doping influence on functional properties of SrTiO3 for use as oxygen transport membranes, Journal of the European Ceramic Society 38(15) (2018) 5058-5066.
- [55] X. Li, H. Zhao, N. Xu, X. Zhou, C. Zhang, N. Chen, Electrical conduction behavior of La, Co co-doped SrTiO3 perovskite as anode material for solid oxide fuel cells, International Journal of Hydrogen Energy 34(15) (2009) 6407-6414.
- [56] Z. Zhao, R.V. Goncalves, S.K. Barman, E.J. Willard, E. Byle, R. Perry, Z. Wu, M.N. Huda, A.J. Moulé, F.E. Osterloh, Electronic structure basis for enhanced overall water splitting photocatalysis with aluminum doped SrTiO3 in natural sunlight, Energy & Environmental Science 12(4) (2019) 1385-1395.
- [57] M.A.K.Y. Shah, Y. Lu, N. Mushtaq, M. Yousaf, S. Rauf, M.I. Asghar, P.D. Lund, B. Zhu, Perovskite Al-SrTiO3 semiconductor electrolyte with superionic conduction in ceramic fuel cells, Sustainable Energy & Fuels 6(16) (2022) 3794-3805.
- [58] G. He, W. Liang, C.L. Tsai, X. Xia, S. Baumann, H. Jiang, W.A. Meulenberg, Chemical Environment-Induced Mixed Conductivity of Titanate as a Highly Stable Oxygen Transport Membrane, iScience 19 (2019) 955-964.
- [59] M.L. Weber, M. Wilhelm, L. Jin, U. Breuer, R. Dittmann, R. Waser, O. Guillon, C. Lenser,F. Gunkel, Exsolution of Embedded Nanoparticles in Defect Engineered Perovskite Layers,ACS Nano 15(3) (2021) 4546-4560.
- [60] N. Xu, J. Zhang, S. Su, J. Feng, Z. Xu, Preparation and bifunctional properties of the Asite-deficient SrTi(0.3)Fe(0.6)Ni(0.1)O(3-delta) perovskite, RSC advances 12(52) (2022) 33789-33800.
- [61] T. Ishihara, S. Miyoshi, T. Furuno, O. Sanguanruang, H. Matsumoto, Mixed conductivity and oxygen permeability of doped Pr2NiO4-based oxide, Solid State Ionics 177(35) (2006) 3087-3091.
- [62] T. Klande, K. Efimov, S. Cusenza, K.-D. Becker, A. Feldhoff, Effect of doping, microstructure, and CO2 on La2NiO4+δ-based oxygen-transporting materials, Journal of Solid State Chemistry 184 (2011) 3310–3318.
- [63] J.M. Bassat, P. Odier, A. Villesuzanne, C. Marin, M. Pouchard, Anisotropic ionic transport properties in La2NiO4+δ single crystals, Solid State Ionics 167(3) (2004) 341-347.

- [64] A. Flura, S. Dru, C. Nicollet, V. Vibhu, S. Fourcade, E. Lebraud, A. Rougier, J.-M. Bassat, J.-C. Grenier, Chemical and structural changes in Ln2NiO4+δ (Ln=La, Pr or Nd) lanthanide nickelates as a function of oxygen partial pressure at high temperature, Journal of Solid State Chemistry 228 (2015) 189-198.
- [65] N. Han, Q. Wei, H. Tian, S. Zhang, Z. Zhu, J. Liu, S. Liu, Front Cover: Highly Stable Dual Phase Membrane Based on Ce 0.9 Gd 0.1 O 2 δ —La 2 NiO 4+ δ for Oxygen Permeation under Pure CO 2 Atmosphere (Energy Technol. 5/2019), 2019.
- [66] K. Świerczek, H. Zhao, Z. Zhang, Z. Du, MIEC-type ceramic membranes for the oxygen separation technology, E3S Web of Conferences 108 (2019) 01021.
- [67] T. Ishihara, Oxide ion conductivity in defect perovskite, Pr₂NiO₄ and its application for solid oxide fuel cells, Journal of the Ceramic Society of Japan 122(1423) (2014) 179-186.
- [68] V.V. Kharton, F.M.B. Marques, A. Atkinson, Transport properties of solid oxide electrolyte ceramics: a brief review, Solid State Ionics 174(1) (2004) 135-149.
- [69] O. Yamamoto, Y. Arati, Y. Takeda, N. Imanishi, Y. Mizutani, M. Kawai, Y. Nakamura, Electrical conductivity of stabilized zirconia with ytterbia and scandia, Solid State Ionics 79 (1995) 137-142.
- [70] M.A. Borik, S.I. Bredikhin, V.T. Bublik, A.V. Kulebyakin, I.E. Kuritsyna, E.E. Lomonova, P.O. Milovich, V.A. Myzina, V.V. Osiko, P.A. Ryabochkina, N.Y. Tabachkova, Structure and conductivity of yttria and scandia-doped zirconia crystals grown by skull melting, Journal of the American Ceramic Society 100(12) (2017) 5536-5547.
- [71] D.A. Andersson, S.I. Simak, N.V. Skorodumova, I.A. Abrikosov, B. Johansson, Optimization of ionic conductivity in doped ceria, Proceedings of the National Academy of Sciences 103(10) (2006) 3518-3521.
- [72] S. Omar, E.D. Wachsman, J.L. Jones, J.C. Nino, Crystal Structure–Ionic Conductivity Relationships in Doped Ceria Systems, Journal of the American Ceramic Society 92(11) (2009) 2674-2681.
- [73] J. Xue, Q. Liao, Y. Wei, Z. Li, H. Wang, A CO2-tolerance oxygen permeable 60Ce0.9Gd0.1O2-δ-40Ba0.5Sr0.5Co0.8Fe0.2O3-δ dual phase membrane, Journal of Membrane Science 443 (2013) 124–130.

- [74] H. Luo, H. Jiang, T. Klande, Z. Cao, F. Liang, H. Wang, J. Caro, Novel Cobalt-Free, Noble Metal-Free Oxygen-Permeable 40Pr0.6Sr0.4FeO3-δ–60Ce0.9Pr0.1O2–δ Dual-Phase Membrane, Chemistry of Materials 24(11) (2012) 2148-2154.
- [75] Y. Ji, J.A. Kilner, M.F. Carolan, Electrical properties and oxygen diffusion in yttriastabilised zirconia (YSZ)–La0.8Sr0.2MnO3±δ (LSM) composites, Solid State Ionics 176(9) (2005) 937-943.
- [76] L. Shi, S. Wang, T. Lu, Y. He, D. Yan, Q. Lan, Z. Xie, H. Wang, M.-R. Li, J. Caro, H. Luo, High CO2-tolerance oxygen permeation dual-phase membranes Ce0.9Pr0.1O2-δ-Pr0.6Sr0.4Fe0.8Al0.2O3-δ, Journal of Alloys and Compounds 806 (2019) 500-509.
- [77] G. Chen, B. Tang, M. Widenmeyer, L. Wang, A. Feldhoff, A. Weidenkaff, Novel CO2-tolerant dual-phase Ce0.9Pr0.1O2–δ La0.5Sr0.5Fe0.9Cu0.1O3–δ membranes with high oxygen permeability, Journal of Membrane Science 595 (2020) 117530.
- [78] M. Balaguer, J. García-Fayos, C. Solís, J.M. Serra, Fast Oxygen Separation Through SO2-and CO2-Stable Dual-Phase Membrane Based on NiFe2O4–Ce0.8Tb0.2O2-δ, Chemistry of Materials 25(24) (2013) 4986-4993.
- [79] J. García-Fayos, R. Ruhl, L. Navarrete, H.J.M. Bouwmeester, J.M. Serra, Enhancing oxygen permeation through Fe2NiO4–Ce0.8Tb0.2O2–δ composite membranes using porous layers activated with Pr6O11 nanoparticles, Journal of Materials Chemistry A 6(3) (2018) 1201-1209.
- [80] P. Niehoff, S. Baumann, F. Schulze-Küppers, R.S. Bradley, I. Shapiro, W.A. Meulenberg, P.J. Withers, R. Vaßen, Oxygen transport through supported Ba0.5Sr0.5Co0.8Fe0.2O3-δ membranes, Separation and Purification Technology 121 (2014) 60-67.
- [81] F. Mauvy, J.M. Bassat, E. Boehm, P. Dordor, J.C. Grenier, J.P. Loup, Chemical oxygen diffusion coefficient measurement by conductivity relaxation—correlation between tracer diffusion coefficient and chemical diffusion coefficient, Journal of the European Ceramic Society 24(6) (2004) 1265-1269.
- [82] P.-M. Geffroy, E. Blond, N. Richet, T. Chartier, Understanding and identifying the oxygen transport mechanisms through a mixed-conductor membrane, Chemical Engineering Science 162 (2017).
- [83] R. Cox-Galhotra, S. McIntosh, Unreliability of simultaneously determining kehem and

- Dehem via conductivity relaxation for surface-modified La0.6Sr0.4Co0.2Fe0.8O3 $-\delta$, Solid State Ionics 181 (2010) 1429-1436.
- [84] A. Arratibel Plazaola, A. Cruellas Labella, Y. Liu, N. Badiola Porras, D.A. Pacheco Tanaka, M.V. Sint Annaland, F. Gallucci, Mixed Ionic-Electronic Conducting Membranes (MIEC) for Their Application in Membrane Reactors: A Review, Processes 7(3) (2019) 128.
- [85] W.J. Koros, Y.H. Ma, T. Shimidzu, Terminology for membranes and membrane processes (IUPAC Recommendations 1996), 68(7) (1996) 1479-1489.
- [86] L.C. A. J. Burggraaf*, Fundamentals of inorganic membrane science and technology, Elsevier1996.
- [87] Y. Zhang, R.-h. Yuan, J.-f. Gao, C.-s. Chen, Oxygen permeation properties of supported planar Zr0.84Y0.16O1.92-La0.8Sr0.2Cr0.5Fe0.5O3–δ composite membranes, Separation and Purification Technology 166 (2016) 142-147.
- [88] T.H. Lee, Y.L. Yang, A.J. Jacobson, B. Abeles, M. Zhou, Oxygen permeation in dense SrCo0.8Fe0.2O3 δ membranes: Surface exchange kinetics versus bulk diffusion, Solid State Ionics 100(1) (1997) 77-85.
- [89] J.H. Shim, J.S. Park, T.P. Holme, K. Crabb, W.J. Lee, Y.B. Kim, X. Tian, T.M. Gur, F.B. Prinz, Enhanced oxygen exchange and incorporation at surface grain boundaries on an oxide ion conductor, 60.

Chapter 2

2. Ni-doping influence on functional properties of $SrTi_{0.65}Fe_{0.35}O_{3-\delta}$ for use as oxygen transport membranes

Abstract

Pure strontium titanate, SrTiO₃, exhibits excellent thermodynamic stability but negligible electronic and ionic conductivity in a wide range of temperatures and oxygen partial pressures. In order to improve the conductivity, B-site doping strategy is used in this work. The $SrTi_{0.65-x}Fe_{0.35}Ni_xO_{3-\delta}$ (x=0, 0.05, 0.075, 0.1) (STFN_x) powders were synthesized by a solidstate reaction method at 1200 °C and then sintered into membranes at 1350/1400 °C for 5 h. Functionality, i.e. mixed ionic and electronic conductivity, is introduced by substitution of Ti by Fe and Ni. In addition, Ni is proven to improve the catalytic performance by exsolution phenomenon. The XRD patterns show that the materials are single phase after sintering in air. The oxygen permeance and the ionic conductivity of STFN_x increase with an increasing Ni content and are close to benchmark La_{0.6}Sr_{0.4}Co_{0.7}Fe_{0.8}O_{3.-δ} at around 850 °C. Thermochemical stability tests were performed by annealing samples in syngas with/without H₂S and clean H₂. XRD analysis and thermogravimetry analysis (TGA) reveal that STFN005 exhibits good thermochemical stability in reducing atmospheres and the stability of STFN_x decreases with increasing Ni content. Well distributed Fe/Ni exsolution particles can be found even with the lowest Ni amount doped material SrTi_{0.6}Fe_{0.35}Ni_{0.05}O_{3-δ} after annealing in reducing atmosphere, which will be beneficial to catalytic performance in a membrane reactor. Therefore, 5 mol% Ni doped STFN005 can be a promising material in catalytic membrane reactors, e.g. for partial oxidation of methane (POM).

This chapter has been published as: Y. Tang, S. Baumann, M. Müller, D. Sebold, A. Nijmeijer, O. Guillon, W.A. Meulenberg, Ni-doping influence on functional properties of SrT_{i0.65}Fe_{0.35}O₃₋₆ for use as oxygen transport membranes, Journal of the European Ceramic Society 44(15) (2024) 116742, DOI: https://doi.org/10.1016/j.jeurceramsoc.2024.116742

2.1 Introduction

Mixed ionic-electronic conducting (MIEC) materials are promising candidates of oxygen transport membranes (OTMs). They have attracted great interests in scientific research due to the high product purity and energy efficiency of oxygen separation from air as well as application in catalytic membrane reactors, e.g. for partial oxidation of methane (POM) [1, 2] and solid oxide fuel cell (SOFC) electrodes [3, 4]. For membrane reactors, materials are usually operated under harsh reducing and/or corrosive atmosphere like CO, H₂ and CH₄ at high temperature of approx. 800-900 °C. Therefore, the structural stability of MIEC membranes under operating conditions is a very important factor. La_{1-x}Sr_xCo_{1-y}Fe_yO_{3-δ} (LSCF) and Ba_{0.5}Sr_{0.5}Co_{0.8}Fe_{0.2}O_{3.δ} (BSCF) have been widely studied showing high oxygen permeability [5-12]. However, the high oxygen permeability of LSCF and BSCF relies on highly redoxactive B-site elements in particular Co, which is accompanied with low structural stability in reducing environments[9-12]. Some approaches have been applied for improving the stability of MIEC membranes. For example, partial substitution of A or B sites with cations with a higher valence or larger radius, such as Al[13, 14], Ti[15], Zr[16], Y[17, 18] and Nb[19]. Although these methods successfully improved stability to some degree, these materials are still not sufficiently stable against the reducing and corrosive atmospheres in some membrane reactors due to the high amount of Co and Fe on the B-site. Besides, the substitution of Co/Fe with Al/Zn will also reduce the oxygen permeability and conductivity in some cases due to lower oxygen diffusion or much lower oxygen surface-exchange kinetics[20, 21] In addition, dualphase ceramic membranes have also shown to be stable for the use in membrane reactors by introducing fluorites such as Y doped ZrO₂ (YSZ), Sm₂O₃ doped CeO₂ (SDC) or Gd doped CeO₂ (GDC) into the material structure [22, 23]. However, stability issues in reducing atmospheres remain due to the redox-active electronic conducting second phase as well as the chemical expansion particularly of ceria and resulting thermal/chemical stresses in the composite.

On the other hand, the perovskite material SrTiO₃ exhibits high stability in a wide range of temperatures and atmospheres, but negligible oxygen permeation performance due to a low concentration of intrinsic defects. The performance of SrTiO₃ can be improved by A/B-site

doping strategies to create oxygen vacancies as well as electronic defects in the material. In particular. B-site Ti⁴⁺ can be substituted by metal cations with lower valence, such as Fe³⁺[24-27], Co²⁺[28, 29], Al³⁺[30, 31], Mg²⁺[32] and Ni²⁺[33, 34], in order to introduce the required oxygen permeability. Redox-active elements, i.e. Fe, Co and in particular Ni, can be exsolved from the crystal lattice in very reducing atmospheres [33, 35-37]. Since Ni-based catalysts can achieve good CH₄ conversion and syngas selectivity in partial oxidation of methane (POM), Ni is a promising dopant potentially improving both the permeability as well as the catalytic activity. Our preliminary work indicated that SrTi_{0.65}Fe_{0.35}O_{3-\delta} (STF35) can achieve a good balance between stability and oxygen separation from air while Co doping again leads to instability in reducing atmospheres [24, 38]. However, the influence of Ni-doping on the functional properties of STF35 for oxygen transport membrane (OTM) materials has not yet been systematically characterized. Therefore, we studied the compositions $SrTi_{0.65-x}Fe_{0.35}Ni_xO_{3-\delta}$ (x=0, 0.05, 0.075, 0.1) (STFN_x) with the effects of Ni doping on oxygen permeation, electronic conductivity. The phase stability after annealing in H₂/Ar, clean syngas and syngas with H₂S contamination was also investigated.

2.2 Experimental

2.2.1 Sample preparation

SrTi_{0.65-x}Fe_{0.35}Ni_xO_{3- δ} (x=0, 0.05, 0.075, 0.1) (STF35, STFN005, STFN0075 and STFN010) powder was synthesized by a solid-state reaction method. The precursors SrCO₃ (Merck, 99%), TiO₂ (Merck, 99%), Fe₂O₃ (Merck, 99%), NiO (Merck, 99%) were ball milled for 24 h, dried and sieved through 500 μ m mesh, then calcined at 1200 °C for 5 h. The derived powders were ball milled again for 24 h. As-synthesized powder was collected after drying. Bulk membranes were then uniaxially pressed in the form of discs at around 70 MPa for 1.5 minutes using an uniaxial press model PW10 (\varnothing 20 mm) (Fa. Paul Otto Weber GmbH, Remshalden). The pressed STFN_x and STF35 membranes were sintered at 1350 °C and 1400 °C for 5 h, respectively. Heating and cooling rates were 5 K/min.

2.2.2 Structural characterization

The desired composition of Sr, Ti, Fe, and Ni was confirmed by Inductively Coupled Plasma-Optical Emission Spectrometry (ICP-OES) on a Thermo ScientificTM iCAPTM 7600 ICP-OES Analyzer. The particle size distribution (PSD) of the powder was determined using a particle analyzer HORIBA LA-950V2 (Horiba European GmbH, Germany). Crystalline structure and phase compositions were tested by X-ray diffraction (XRD) using a Bruker D4 ENDEAVOR diffractometer at room temperature with Cu Kα radiation in the 2θ range 10–80°. The step size used was 0.02° and 0.75 s per step. The XRD patterns were analyzed using Topas software. Microstructures were imaged via scanning electron microscopy (SEM) using a Zeiss GeminiSEM 450. Energy dispersive X-ray spectroscopy (EDS) was performed with Ultim Max 170 detector from Oxford Instruments. The gas tightness of the sintered membrane was checked by a He-leak rate detector (Qualy test HTL 260, Pfeiffer Vacuum GmbH, Asslar, Germany). The cyclic thermogravimetric analysis (TGA) measurements were carried out with a calorimeter STA449 F1 Jupiter coupled to the mass spectrometer QMS 403C Aëolos (Netzsch) in air and 2.9 vol% H₂/Ar. The final temperature was 900 °C with a heating/cooling rate of 10 °C/min in air and the gas flow rate was 50 mL/min. The holding time was 2 h for every cycle for reduction as well as oxidation.

2.2.3 Electrical conductivity measurements

Temperature dependent electrical conductivity measurements were conducted on a Keithley 2400 four-probe DC measurement setup from 600 to 900 °C in air (21 vol% O₂ and 79 vol% N₂). All samples were ground with sand paper step by step in order to remove contaminations on the surface and get a smooth surface before measurements. With a diamond wire saw (HDS25, Diamond WireTec GmbH&Co.KG), the samples were cut into bars with approx. 6mm width, 15mm length and 0.7mm height. Gold wires with a diameter of 0.25 mm were used to connect the rectangular samples with the DC measurement setup and additional gold paste was also used to enhance the contact between the gold wires and the sample surface. The total electrical conductivity of the materials can be calculated using the following equation:

$$\sigma_{total} = \frac{D}{R \cdot A} \tag{2.1}$$

where σ_{total} is the total electrical conductivity (S/cm), D is the distance between the inner voltage electrodes (cm), R is the resistance (Ω) and A is the cross-sectional area of the rectangular samples (cm²), respectively.

2.2.4 Oxygen permeation measurement

The oxygen permeance, as discussed in Chapter 1, is an important parameter to investigate the performance of oxygen transport membranes. It can be calculated by normalizing the oxygen flux $j(O_2)$ by the oxygen partial pressure gradient $(\ln \frac{p'_{O_2}}{p''_{O_2}})$, which is the driving force for

oxygen permeation. The oxygen flux $j(O_2)$ can be expressed by equation (2.2):

$$j(O_2) = \frac{R}{16F^2 \cdot L} \cdot T \cdot \sigma_{amb} \cdot \ln \frac{p'_{O_2}}{p''_{O_2}}$$
(2.2)

where R is the gas constant, T is the temperature, F is the Faraday constant, L is the thickness of the membrane, p'_{o_2} and p''_{o_2} are the oxygen partial pressure of oxygen rich and lean side of the membrane, respectively, and σ_{amb} is the ambipolar conductivity, which can be expressed by equation (2.3):

$$\sigma_{amb} = \frac{\sigma_i \cdot \sigma_e}{\sigma_i + \sigma_e} \tag{2.3}$$

where σ_i and σ_e are the ionic and electronic conductivity, respectively.

The oxygen permeance can be expressed as:

$$Permeance = \frac{j(O_2)}{\ln \frac{p'_{O_2}}{p''_{O_2}}} = \frac{R}{16F^2 \cdot L} \cdot T \cdot \sigma_{amb}$$
 (2.4)

The activation energy of the oxygen permeance can be obtained by the Arrhenius approach:

$$\ln(permeance) = -\frac{E_a}{RT} + A \tag{2.5}$$

Where E_a is the activation energy and A is the pre-exponential factor.

Oxygen permeation measurements were conducted on a 4-end mode set up in air (feed gas)/Ar (sweep side) atmosphere from 650 °C to 1000 °C. The size of the dense membrane was around \varnothing 14.6 mm x 1mm. The flow rate of the gas streams was controlled using mass flow controllers (MFCs). The standard flow rate was 250 mL·min⁻¹ for the feed side (air) and 50 mL·min⁻¹ for the sweep side (Ar). All samples were ground to 1 mm thickness using the same process for electrical conductivity measurements. Afterwards, the samples were sealed using gold rings with an inner diameter of 13 mm to a quartz glass reactor. The O₂ concentration was recorded by a mass spectrometer (Omni Star, Pfeiffer vacuum US) during measurements.

2.2.5 Annealing measurement

The annealing experiments aimed to investigate the thermo-chemical stability of the materials by simulating the composition from partial oxidation of methane gas $(CH_4 + 1/2 O_2 = > CO + 2 H_2)$. To prevent the formation of soot even at the lowest temperature, steam was added in the mixed gas. Furthermore, clean methane and sour gas containing H₂S was considered. Therefore, the samples were annealed for 72 h in a gas stream of 150 ml/min 25 vol% CO (with/without 1000 ppm H₂S) + 50 vol% H₂ + 25 vol% H₂O forming different syngas compositions (pure syngas and syngas with H₂S) equilibrated at 600 °C, 700 °C, 800 °C, and 900 °C, respectively. Experiments were conducted in a four tubes set-up[39], which can anneal samples at four different temperatures in the same gas atmosphere at the same time. Sintered pellets (Ø 8 mm x 5 mm) were put in alumina boats in order to investigate the surface change before and after annealing. The well mixed gases were sent to the tubes when the four tubes reached the different aimed temperatures. The tubes were heated/cooled in N2 with a rate of 10 K/min. The annealing experiment in clean H₂ was conducted in 2.9 vol% H₂/Ar at 800 °C for 10h. The software package FactSage 7.1 (GTT Technologies, Herzogenrath, Germany) was used for thermodynamic calculations. The calculations were based on the commercial database FactPS in the software package.

2.3 Results and discussion

2.3.1 Crystal structure and microstructure

Table 2.1 lists the particle size distribution of as-synthesized powders after calcination and sieving and the sintering temperature of the pressed samples. The powders show a monomodal distribution with d50 values around 1.5 µm. The intended chemical composition of all samples was confirmed by ICP-OES measurements. Figure 2.1(a) shows the XRD patterns of the STF35 and STFN_x pellets sintered at 1400 °C and 1350 °C for 5 h, respectively, confirming that all pellets are single phase. The results identify that the space group of all the materials is Pm3m (cubic perovskite structure). Doping Ni in STF35 causes shifting of all reflections towards higher diffraction angles, exemplarily shown by zoomed-in patterns for 30°~35° (Figure 2.1(b)), which indicates a decrease in the lattice constant. The lattice parameters of the perovskites have been determined from XRD patterns, which are 3.903 Å, 3.897 Å, 3.891 Å and 3.889 Å for STF35, STFN005, STFN0075 and STFN010, respectively. It was reported that Ni can take +2 (0.69 Å) and +3 (0.56 Å) oxidation states during incorporation into Ti in SrTiO₃ [40, 41] and Ni-doped STF structures [34, 42]. The substitution of the host Ti⁴⁺ (0.605 Å) with the dopant Ni³⁺ (0.56 Å) is expected to decrease the lattice constant of SrTi_{1-x}Ni_xO₃ [40, 41]. Therefore, the observed lattice parameter changes of the STFN_x materials suggest that the introduction Ni is most likely in the state of +3. In addition, STF-series and STC-series have also been studied that the lattice parameter of the materials decreased with Fe/Co content increased due to smaller ionic radii of Fe^{4+}/Co^{3+} (0.585 Å /0.545 Å) valence state compared with Ti^{4+} (0.605 Å) [24, 28]. SEM images of cross-section of sintered pellets (Figure 2.2) show that all the sintered materials exhibit good density, which is confirmed by Helium leakage experiments ($< 10^{-7}$ mbar·L·s⁻¹).

Table 2.1 Particle size distribution of as-synthesized powders and sintering temperature of the samples

Name	Commonition	d10	d50	d90	Sintering temperature
	Composition	μm	μm	μm	(°C)
STF35	SrTi _{0.65} Fe _{0.35} O _{3-δ}	0.84	1.68	3.87	1400
STFN005	$SrTi_{0.6}Fe_{0.35}Ni_{0.05}O_{3\text{-}\delta}$	0.80	1.44	3.04	1350
STFN0075	$SrTi_{0.575}Fe_{0.35}Ni_{0.075}O_{3\text{-}\delta}$	0.79	1.47	3.10	1350
STFN010	$SrTi_{0.55}Fe_{0.35}Ni_{0.1}O_{3\text{-}\delta}$	0.89	1.60	3.55	1350

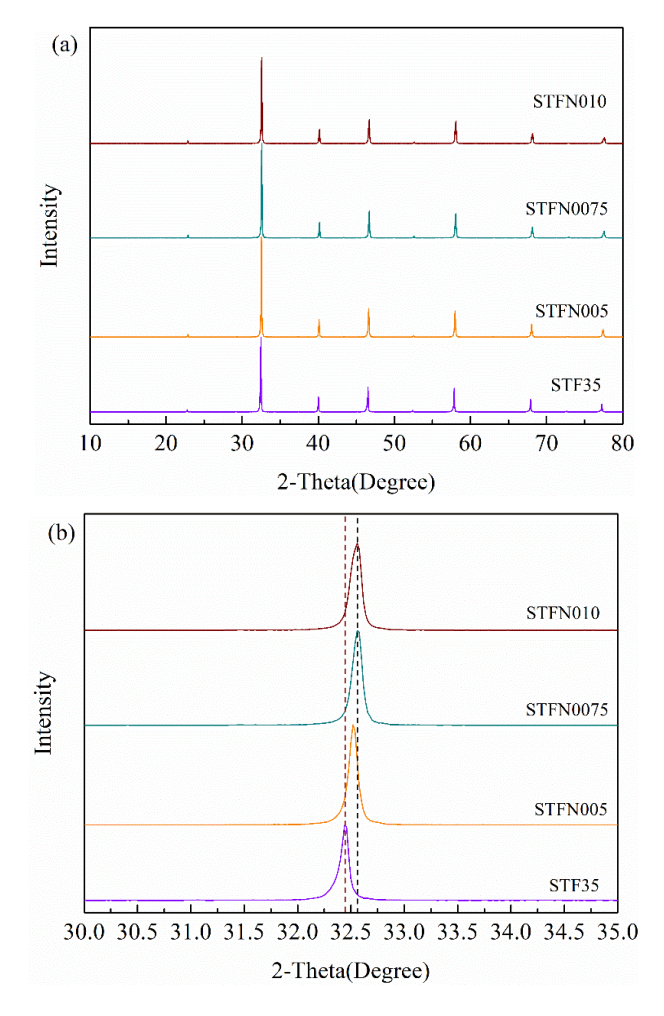


Figure 2.1 XRD patterns of the sintered samples of STF35 and STFN $_{x}$.

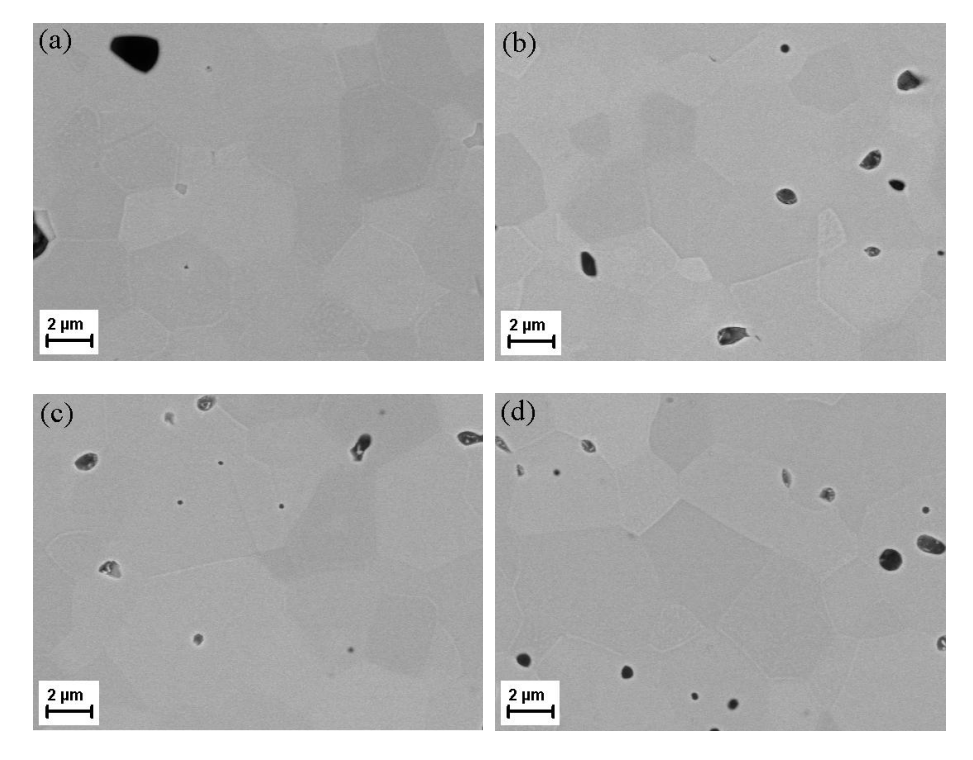


Figure 2.2 Cross-section of sintered (a) STF35; (b) STFN005; (C) STFN0075 and (D) STFN010

2.3.2 Functional properties

Electrical conductivity and oxygen permeation performance were measured to investigate the functional properties of all the materials.

Figure 2.3 shows that the total electrical conductivity of STFN_x increases with increasing Ni content in air and all compositions showed a similar temperature dependence. All materials exhibit semiconductive behavior at low temperature, i.e. below 700 °C of STFN_x (pink dash line), switching to metallic behavior at higher temperature, i.e. above 700 °C of STFN_x (pink dash line) in the studied range, The measured conductivity of STF35 as well as the temperature dependence is reasonable compared to literature data [26, 43-46]. In such semiconductive materials, the electron-lattice distortion coupling is weak at relative low temperature and the migration of small polarons is equivalent to electrons, resulting in rising conductivity with temperature. However, the mobility of small polaron hopping decreases due to strong electron-

lattice distortion coupling at relative high temperature. Therefore, the migration of small polarons is lower than electrons, resulting in a decreasing conductivity with temperature [45].

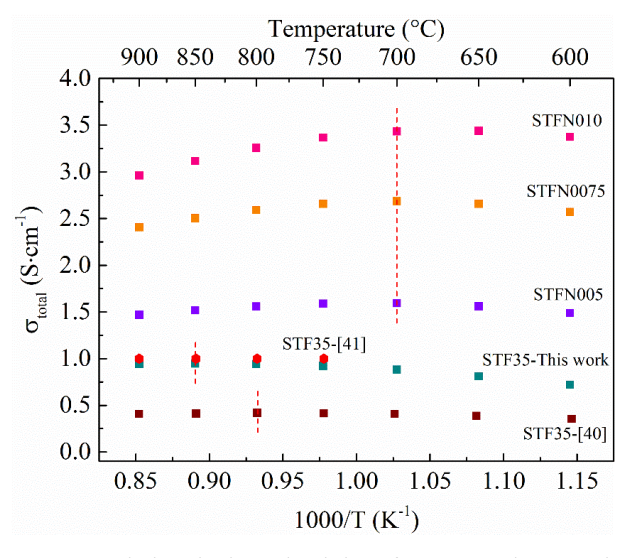


Figure 2.3 Total electrical conductivity of STF35 and STFN_x in air

Figure 2.4 compared the permeance of 1 mm thick STF35, STFN_x, and LSCF6428 as a benchmark. The permeance and oxygen flux increases slightly with increasing Ni content due to the enhanced oxygen vacancy concentration. Furthermore, STFN010 exhibits a comparable oxygen permeance to the standard OTM material LSCF6428 [24] at around 850 °C, and is slightly higher at lower temperatures due to the lower activation energy. Table 2.2 lists the oxygen flux, permeance and activation energy Ea of LSCF6428, STF35, STFN_x as well as the oxygen flux of other oxygen transport membranes at around 900 °C. Although these membranes [47-53]exist quite higher oxygen flux than STFNx, their stability in reducing atmospheres is still too low to meet the requirements in a membrane reactor.

Table 2.2 Oxygen flux, permeance and activation energy Ea of LSCF6428, STF35, STFN $_{x}$ and other oxygen transport membranes at around 900 $^{\circ}$ C

	T ℃	Oxygen flux	Log	Ea of Permeance	Thickness	Ref.
Composition		ml·cm ⁻² ·min ⁻¹	(Permeance)	(800-1000 °C)	(mm)	
			mol·cm ⁻² ·s ⁻¹	kJ/mol		
SrTi _{0.65} Fe _{0.35} O _{3-δ} (STF35)	893	0.15	-7.40	82	1	
$SrTi_{0.6}Fe_{0.35}Ni_{0.05}O_{3-\delta}$ (STFN005)	892	0.17	-7.32	89	1	
$SrTi_{0.575}Fe_{0.35}Ni_{0.075}O_{3-\delta} \\ (STFN0075)$	887	0.17	-7.31	92	1	
$SrTi_{0.55}Fe_{0.35}Ni_{0.1}O_{3-\delta}$ (STFN010)	889	0.20	-7.24	86	1	
$La_{0.6}Sr_{0.4}Co_{0.2}Fe_{0.8}O_{3-\delta}$ (LSCF6428)	883	0.20	-7.19	118	1	[24]
$CaTi_{0.73}Fe_{0.18}Mg_{0.09}O_{3\text{-}\delta}\text{-}$	900	0.46	-	-	0.9	[47]
$BaFe_{0.8}Ca_{0.05}Ti_{0.15}O_{3\text{-}\delta}$	900	0.87	-	-	1	[48]
$SrCo_{0.9}Nb_{0.1}O_{3-\delta}$	900	4.24	-	-	1	[49]
$SrCo_{0.8}Sc_{0.2}O_{3\text{-}\delta}$	900	3.09	-	-	1	[50]
$Ba_{0.6}Sr_{0.4}Co_{0.7}Fe_{0.25}Bi_{0.05}O_{3-\delta}$	900	1.05	-	-	1.2	[51]
$BaCo_{0.7}Fe_{0.15}In_{0.15}O_{3\text{-}\delta}$	900	1.30	-	-	1	[52]
$SrCo_{0.1}Fe_{0.8}Nb_{0.1}O_{3\delta}$	900	0.9	-	-	1	[53]

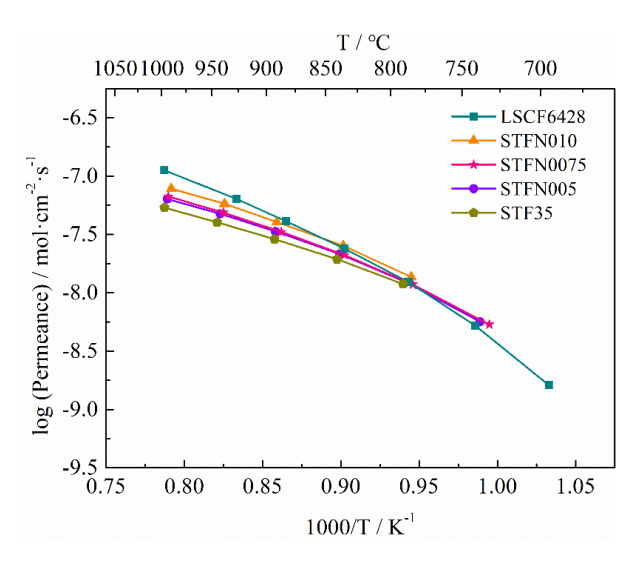


Figure 2.4 Permeance of STF35, STFN_x and benchmark LSCF6428 [24] of 1 mm thickness

The ionic conductivity σ_i can be estimated by calculated the respective ionic transference number t_i according to equation (2.6-2.8).

$$\sigma_{total} = \sigma_i + \sigma_e \tag{2.6}$$

$$\frac{\sigma_{amb}}{\sigma_{total}} = t_i (1 - t_i) \tag{2.7}$$

$$\sigma_i = \sigma_{total} \cdot t_i \tag{2.8}$$

As the ionic transference number of LSCF6428 is quite low 9×10^{-4} at 900 °C [54], and thus, the ionic conductivity is approx. equal to the ambipolar conductivity published by the literature [24] based on permeation tests. The ionic conductivity of different materials is plotted in Figure 2.5. The ionic conductivity of STFN_x is comparable with benchmark LSCF6428 and it increased with increasing Ni content. The activation energy Ea was calculated according to the Arrhenius equation (2.9):

$$\sigma_t = \sigma_0 \cdot \exp(-\frac{1}{T} \cdot \frac{Ea}{R}) \tag{2.9}$$

The results reveal that the activation energy Ea of STF35 and STFN_x is in the range 84-95 $kJ \cdot mol^{-1}$ (Table 2.3), which is lower than that of LSCF6428 (103 $kJ \cdot mol^{-1}$) [24]

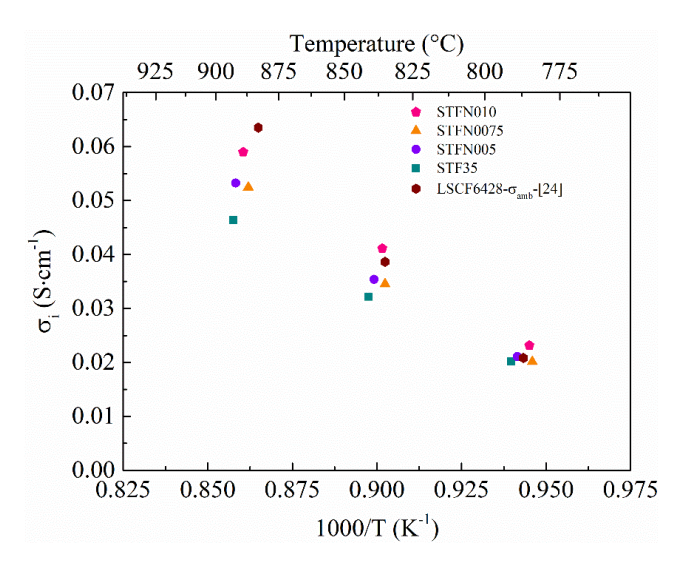


Figure 2.5 Ionic conductivity of different materials in air

Table 2.3 Ionic conductivity, electronic conductivity, ionic transference number t_i and activation energy Ea of STF35 and STFN_x at around 900 °C

	T	Ionic	Electronic	Ionic	Ea(800-
Name	$^{\circ}\!\mathrm{C}$	Conductivity	conductivity	transference	900 °C)
		S·cm ⁻¹	S·cm ⁻¹	number t _i	kJ/mol
STF35	893	4.64×10 ⁻²	0.925	5.02×10 ⁻²	84
STFN005	892	5.31×10 ⁻²	1.468	3.62×10 ⁻²	93
STFN0075	887	5.29×10 ⁻²	2.406	2.20×10 ⁻²	95
STFN010	889	5.90×10 ⁻²	2.961	1.99×10 ⁻²	92

2.3.3 Thermo-chemical stability

Annealing and Two-cycle TGA measurements were conducted to study the thermo-chemical stability of all the materials.

The phase composition of the STF35 and STFN $_x$ samples after annealing under different conditions, i.e. clean H_2 , pure syngas, and syngas with H_2S was measured. XRD patterns of sintered pellets annealed in 2.9 vol% H_2 /Ar at 800 °C for 10 h (Figure 2.6(a)) reveal that minor

Ruddlesden-Popper-like phases Sr₂TiO₄ have formed. Potential exsolution of Ni and Fe [33, 37] cannot be detected by XRD due to too low sensitivity. Therefore, the surface of annealed samples was analyzed by SEM/EDS. Figure 2.6(b-c) shows exemplarily STF35 and STFN005 confirming the exsolution phenomenon. Fe particles marked in pink are well-dispersed on the STF35 surface as shown in Figure 2.6(b) and Fe/Ni inter-metallic phase can be found even with the lowest Ni-doped amount material STFN005 surface marked by the yellow circle in Figure 2.6(c).

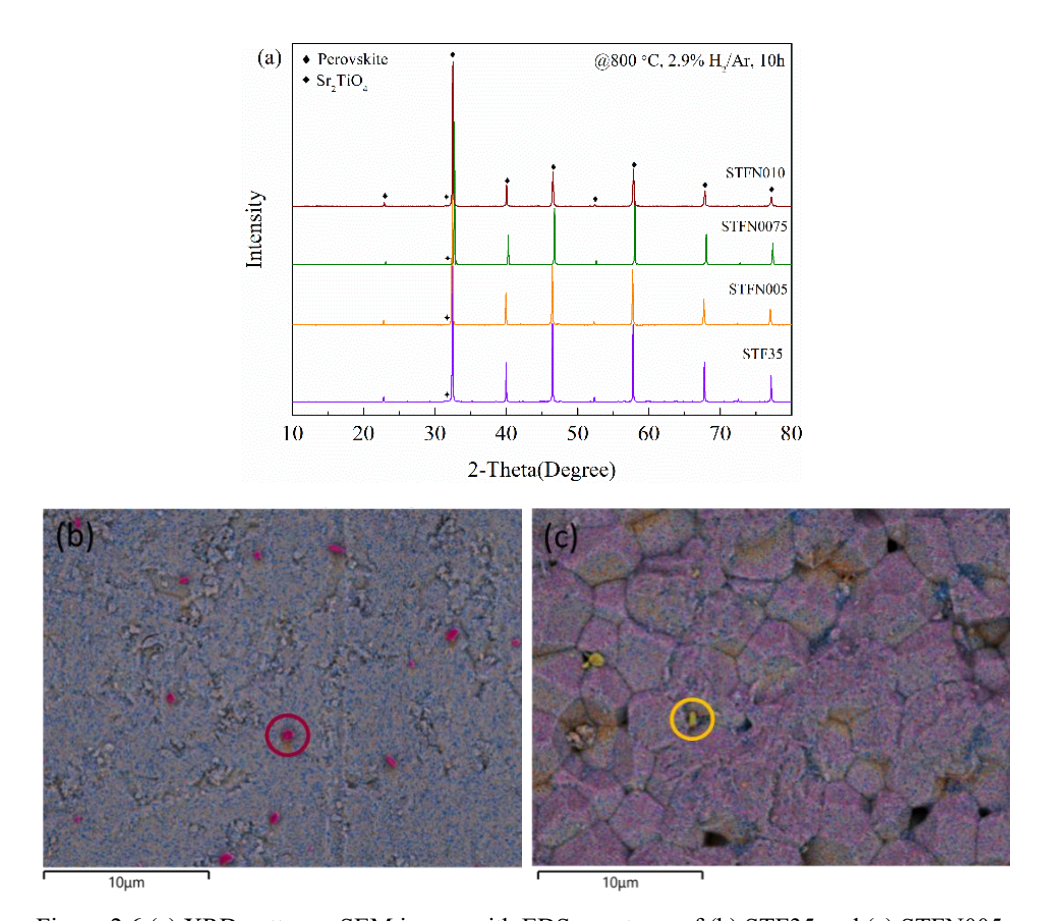


Figure 2.6 (a) XRD patterns, SEM image with EDS-spectrum of (b) STF35 and (c) STFN005 after annealing in 2.9 vol% H₂/Ar at 800 °C

Table 2.4 and Table 2.5 list the calculated gas composition at different temperatures during annealing measurements in pure syngas and syngas with H_2S , respectively. It is assumed that all gas components reach equilibrium during measurements due to the relatively long residence time at respective temperatures. The oxygen partial pressure increases with temperature. The slight changes in H_2S concentration originate from the gas phase reactions resulting in slightly different gas volume (e.g. CO + 3 $H_2 \Longrightarrow CH_4 + H_2O$; 4 mol \Longrightarrow 2 mol). From thermodynamic calculations, potentially ex-solved Ni is expected to equilibrate in presence of H_2S forming Ni_3S_2 (solid/liquid) depending on temperature as shown in Figure 2.7. Unfortunately, STF is not present in the commercial database, so that its stability cannot be predicted by the FactSage software.

Table 2.4 Equilibrium gas composition during annealing measurement in pure syngas

Composition	600 °C	700 °C	800 °C	900 °C
H ₂	47.05%	56.00%	56.40%	55.45%
CO	8.87%	15.86%	18.33%	19.51%
H ₂ O	24.13%	18.37%	18.54%	19.54%
CO_2	12.31%	8.51%	6.62%	5.48%
CH ₄	7.63%	1.25%	0.11%	0.01%
O ₂ (atm)	3.46E-25	1.56E-22	4.73E-20	6.27E-18

Table 2.5 Equilibrium gas composition during annealing measurement in syngas with H₂S

Composition	600 °C	700 °C	800 °C	900 °C
H_2	47.06%	55.99%	56.38%	55.44%
СО	8.83%	15.79%	18.25%	19.43%
H_2O	24.14%	18.39%	18.56%	19.56%
CO_2	12.25%	8.48%	6.60%	5.46%
CH ₄	7.60%	1.25%	0.11%	0.01%
H ₂ S(ppm)	1145	1016	992	989
$Lg(p(H_2S))(atm)$	-2.94	-2.99	-3.00	-3.00
O ₂ (atm)	3.44E-25	1.54E-22	4.69E-20	6.23E-18

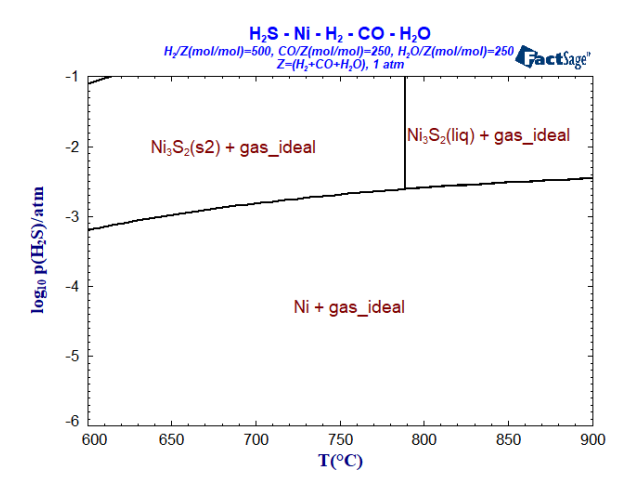


Figure 2.7 Stability of Ni compounds at different temperatures and H_2S partial pressures in syngas

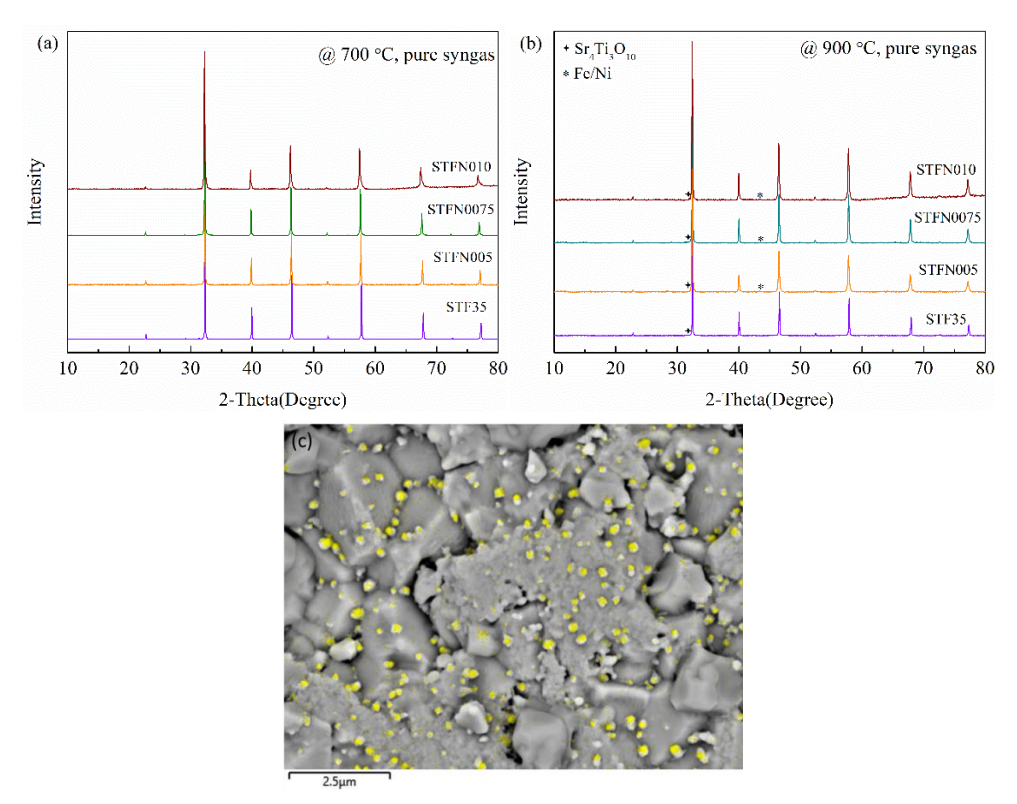


Figure 2.8 XRD patterns of samples annealed at (a) 700 °C and (b) 900 °C, (c) SEM image with EDS-spectrum of Ni (in yellow) of STFN005 annealed at 900 °C in pure syngas

The XRD results of samples annealed in pure syngas show that the materials can maintain single phase after annealing in pure syngas below 700 °C (Figure 2.8(a)). Additional peaks of Sr₄Ti₃O₁₀ and Fe/Ni metallic phase are detected at 900 °C as shown in Figure 2.8(b). The decomposition of perovskite can be explained by the very low p_{O2} (~10⁻¹⁸ bar) and high temperature. Some of the Fe and Ni cations were reduced from the perovskite structure to the metallic state and were therefore extracted from the oxide lattice forming Fe/Ni metallic phase. In order to compensate for the loss of B-site cations, the remaining composition in the structure will form Sr-richer Ruddlesden-Popper-like phases Sr₄Ti₃O₁₀. Figure 2.8(c) reveals that Fe/Ni (marked in yellow) are well distributed on the surface of STFN005 annealed at 900 °C in pure syngas. This will potentially enhance the catalytic performance in a membrane reactor in particular for (partial) oxidation reactions.

For the materials annealed in syngas with H₂S, all the samples are still stable at 600 °C (Figure 2.9(a)). Nevertheless, the Fe/Ni exsolution phenomenon appears stronger at high temperature. It is also found on the surface of samples annealed at 900 °C by XRD patterns, which is consistent with the samples annealed in pure syngas. In addition, the excess SrO from the A site forms SrS in the H₂S-containing atmosphere and the remaining composition then forms Ruddlesden-Popper-like phases Sr₂TiO₄ in order to compensate for the remaining loss of A-site and cations. As Ni is easier to reduce than Fe[55], the intensity of SrS peaks on XRD patterns becomes higher with Ni increasing, indicating that the perovskite structure decomposes more severely and the stability of Ni-doped STF35 decreases with an increasing Ni content. As it is hard to distinguish between Ni and Ni₂S₃ by XRD patterns, SEM/EDS mapping were used to investigate the surface of materials after annealing (Figure 2.10). A very small amount of NiS_x (marked by red) and many Ni areas are clearly shown by EDS mapping. This is consistent with data calculated by FactSage software. The area where Sr and S are enriched at the same time is expected to be the SrS phase. Besides, the Fe/Ni metallic phase can also be detected by the mapping.

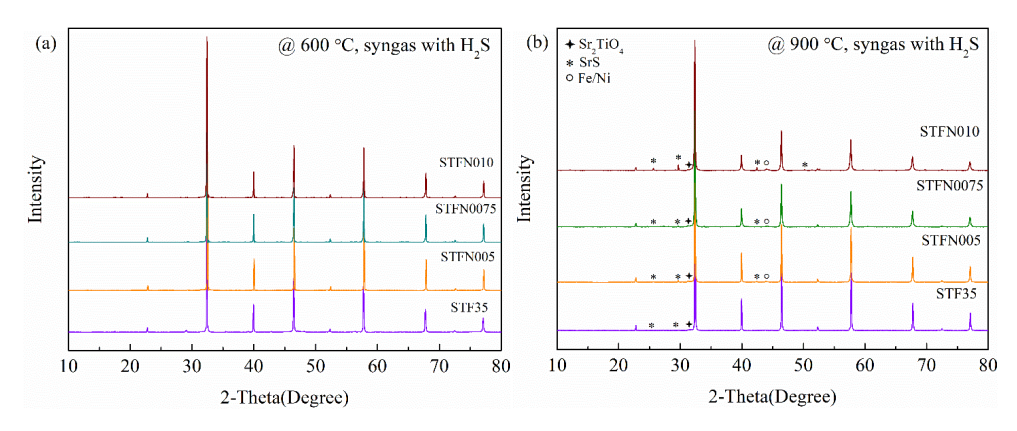


Figure 2.9 XRD patterns of STF35 and STFN_x samples annealed in syngas with H_2S at (a) 600 °C and (b) 900 °C

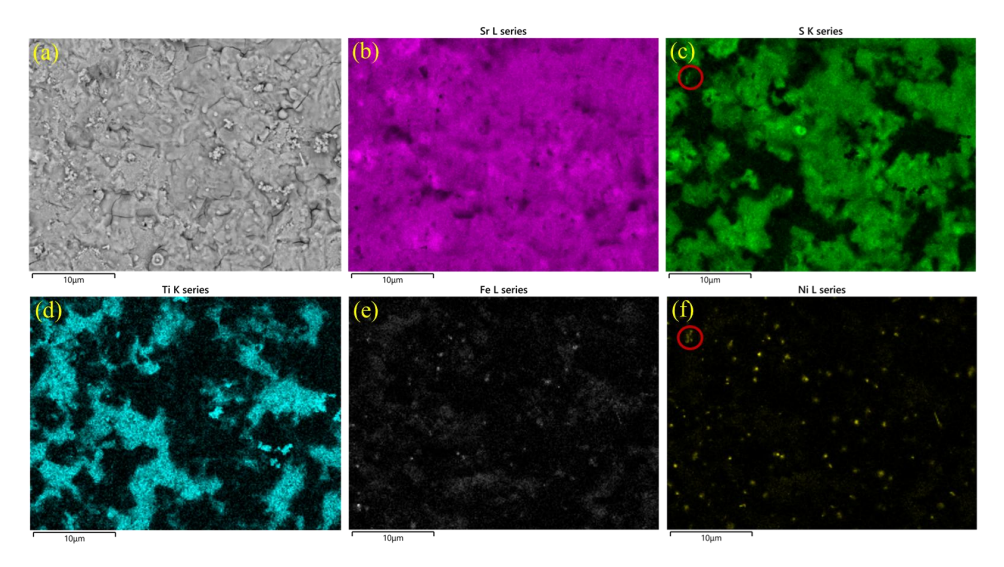


Figure 2.10 SEM images and EDS mapping of STFN005 annealed at 900 $^{\circ}$ C in syngas with H_2S

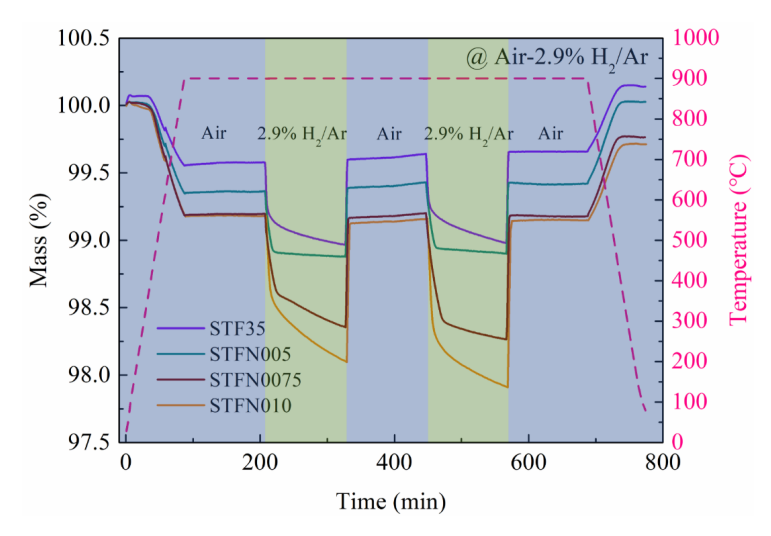


Figure 2.11 Two-cycle TGA measurements of STF35 and STFN $_x$ in air and 2.9 vol% H_2/Ar atmospheres

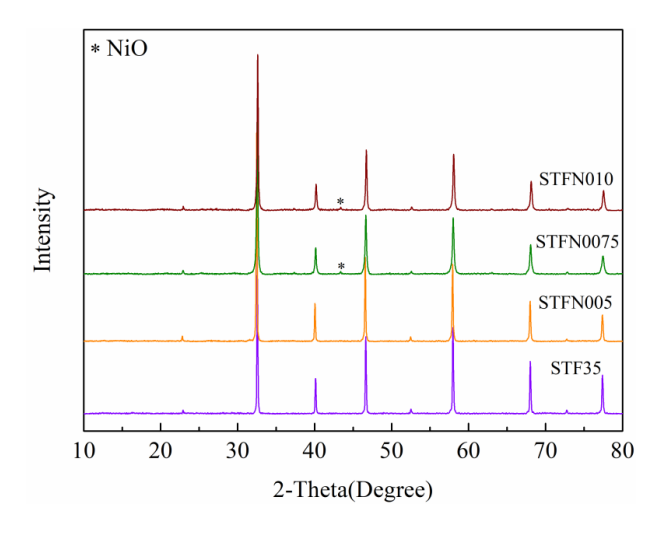


Figure 2.12 XRD patterns of STF35 and STFN_x after two-cycle TGA measurement

Two-cycle TGA measurements were carried out to compare the stability of the four samples in reducing atmosphere (Figure 2.11). The mass loss increases with Ni content increasing. For the first cycle, the mass loss of STF35 and STFN005 is close to each other (1.08 wt.% and 1.12 wt.%, respectively), but the degree strongly increases with 1.65 wt.% for STFN0075 and 1.9 wt.% for STFN010 after dwelling for 2 h in 2.9 vol% H₂/Ar at 900 °C. The mass loss further

increases to 1.74 wt.% for STFN0075 and 2.09 wt.% for STFN010 during the second cycle, while that of STF35 and STFN005 still keeps a similar value as the first cycle (1.02 wt.% and 1.10 wt.%, respectively). XRD patterns shows that STF35 and STFN005 are still single phase after the two-cycle TGA measurements, while additional NiO peaks are found in STFN0075 and STFN010. This indicates that STF35 and STFN005 exhibit higher stability than STFN0075 and STFN010 in reducing atmosphere. Therefore, it can be concluded that the stability of STFN_x will decrease with increasing Ni content and 5 mol% Ni-doped material STFN005 will not significantly reduce the material stability compared to STF35.

2.4 Conclusions

This work studied the influence of Ni doping on the B-site of STFN_x with regard to structural and functional properties for its use in oxygen transport membranes. The results showed that Ni doping on the B-site can increase both electronic and ionic conductivities of STF35. The oxygen permeance of STFN_x slightly varies with Ni concentration and is close to the benchmark LSCF6428. Fe and Ni exsolution phenomenon was clearly found on the surface of STF35 and STFN_x after annealing in reducing atmospheres. All samples still possess the main peaks of perovskite evenly annealed in a very harsh condition, i.e. syngas with high H₂S contamination. The stability of STFN_x decreased with increasing Ni content.

It is worth noting that even 5 mol% Ni-doped material STFN005 exhibits uniformly distributed Fe/Ni exsolution after annealing in a reducing atmosphere, which will benefit the catalytic performance in a membrane reactor. Two-cycle TGA measurements illustrate that STF35 and STFN005 exhibit higher stability than STFN0075 and STFN010 in a reducing atmosphere. Therefore, 5 mol% Ni doped STFN005 can be a promising material for POM in membrane reactors.

REFERENCES

- [1] C. Salles, J. Fouletier, D. Marinha, M.-C. Steil, Determining the rate-limiting step during oxygen semi-permeation of CaTi0.9Fe0.1O3-δ oxygen transport membranes, Journal of Membrane Science 527 (2017) 191 197.
- [2] A.H. Elbadawi, L. Ge, Z. Li, S. Liu, S. Wang, Z. Zhu, Catalytic partial oxidation of methane to syngas: review of perovskite catalysts and membrane reactors, Catalysis Reviews 63(1) (2021) 1-67.
- [3] H. Chen, T. Zhu, X. Chen, Y. Bu, Q. Zhong, Sr(Ti,Fe)O3-δ

 Based Intermediate Temperature Solid Oxide Fuel Cell Anode with Self-precipitated (Ni,Fe) and Gd0.1Ce0.9O2-δ

Nano Particles, Journal of The Electrochemical Society 167(16) (2020) 164507.

- [4] X. Zhou, N. Yan, K.T. Chuang, J. Luo, Progress in La-doped SrTiO3(LST)-based anode materials for solid oxide fuel cells, RSC Adv. 4(1) (2014) 118-131.
- [5] Y. Teraoka, H.-M. Zhang, S. Furukawa, N. Yamazoe, OXYGEN PERMEATION THROUGH PEROVSKITE-TYPE OXIDES, Chemistry Letters 14(11) (1985) 1743-1746.
- [6] F. Schulze-Küppers, S. Baumann, W.A. Meulenberg, D. Stöver, H.P. Buchkremer, Manufacturing and performance of advanced supported Ba0.5Sr0.5Co0.8Fe0.2O3-δ (BSCF) oxygen transport membranes, Journal of Membrane Science 433 (2013) 121-125.
- [7] C. Niedrig, S. Taufall, M. Burriel, W. Menesklou, S. Wagner, S. Baumann, E. Ivers-Tiffée, Thermal stability of the cubic phase in Ba0.5Sr0.5Co0.8Fe0.2O3-delta (BSCF)1, Solid State Ionics 197 (2011) 25–31.
- [8] E.V. Artimonova, O.A. Savinskaya, A.P. Nemudry, Effect of B-site tungsten doping on structure and oxygen permeation properties of SrCo0.8Fe0.2O3-δ perovskite membranes, Journal of the European Ceramic Society 35(8) (2015) 2343-2349.
- [9] M. Kuhn, S. Hashimoto, K. Sato, K. Yashiro, J. Mizusaki, Oxygen nonstoichiometry and thermo-chemical stability of La0.6Sr0.4CoO3-, Journal of Solid State Chemistry 197 (2013) 38-45.
- [10] J. Ovenstone, J.-I. Jung, J.S. White, D.D. Edwards, S.T. Misture, Phase stability of BSCF in low oxygen partial pressures, Journal of Solid State Chemistry 181(3) (2008) 576-586.

- [11] S.J. Xu, W.J. Thomson, Stability of La0.6Sr0.4Co0.2Fe0.8O3-δ Perovskite Membranes in Reducing and Nonreducing Environments, Industrial & Engineering Chemistry Research 37(4) (1998) 1290-1299.
- [12] M. Arnold, H. Wang, A. Feldhoff, Influence of CO2 on the Oxygen Permeation Performance and the Microstructure of Perovskite-Type (Ba0.5Sr0.5)(Co0.8Fe0.2)O3-?? Membranes, Journal of Membrane Science 293 (2007) 44-52.
- [13] Z. Wu, W. Jin, N. Xu, Oxygen permeability and stability of Al2O3-doped SrCo0.8Fe0.2O3-δ mixed conducting oxides, Journal of Membrane Science 279(1-2) (2006) 320-327.
- [14] A.L. Shaula, V.V. Kharton, J.C. Waerenborgh, D.P. Rojas, E.V. Tsipis, N.P. Vyshatko, M.V. Patrakeev, F.M.B. Marques, Transport properties and Mössbauer spectra of Fe-substituted La10–x(Si,Al)6O26 apatites, Materials Research Bulletin 39(6) (2004) 763-773.
- [15] Y. Shen, F. Wang, X. Ma, T. He, SrCo 1– y Ti y O 3– δ as potential cathode materials for intermediate-temperature solid oxide fuel cells, Lancet 196 (2011) 7420-7425.
- [16] O. Ravkina, T. Klande, A. Feldhoff, Investigation of Zr-doped BSCF perovskite membrane for oxygen separation in the intermediate temperature range, Journal of Solid State Chemistry 201 (2013) 101–106.
- [17] P. Haworth, S. Smart, J. Glasscock, J.C. Diniz da Costa, Yttrium doped BSCF membranes for oxygen separation, Separation and Purification Technology 81(1) (2011) 88-93.
- [18] L.-S. Unger, R. Ruhl, M. Meffert, C. Niedrig, W. Menesklou, S.F. Wagner, D. Gerthsen, H.J.M. Bouwmeester, E. Ivers-Tiffée, Yttrium doping of Ba 0.5 Sr 0.5 Co 0.8 Fe 0.2 O 3-δ part II: Influence on oxygen transport and phase stability, Journal of the European Ceramic Society 38(5) (2018) 2388-2395.
- [19] F. Wang, T. Nakamura, K. Yashiro, J. Mizusaki, K. Amezawa, Effect of Nb doping on the chemical stability of BSCF-based solid solutions, Solid State Ionics 262 (2014) 719-723.
- [20] G. Coffey, Electrochemical properties of lanthanum strontium aluminum ferrites for the oxygen reduction reaction, Solid State Ionics 158(1-2) (2003) 1-9.
- [21] M. Reichmann, P.M. Geffroy, J. Fouletier, N. Richet, P. Del Gallo, T. Chartier, Effect of cation substitution at the B site on the oxygen semi-permeation flux in La 0.5 Ba 0.5 Fe 0.7 B 0.3 O $3-\delta$ dense perovskite membranes with B = Al, Co, Cu, Mg, Mn, Ni, Sn, Ti and Zn (part

- II), Journal of Power Sources 277 (2015) 17-25.
- [22] X. Zhu, Q. Li, Y. He, Y. Cong, W. Yang, Oxygen permeation and partial oxidation of methane in dual-phase membrane reactors, Journal of Membrane Science 360(1-2) (2010) 454-460.
- [23] J.-j. Liu, S.-q. Zhang, W.-d. Wang, J.-f. Gao, W. Liu, C.-s. Chen, Partial oxidation of methane in a Zr0.84Y0.16O1.92–La0.8Sr0.2Cr0.5Fe0.5O3–δ hollow fiber membrane reactor targeting solid oxide fuel cell applications, Journal of Power Sources 217 (2012) 287-290.
- [24] F. Schulze-Küppers, S.F.P. ten Donkelaar, S. Baumann, P. Prigorodov, Y.J. Sohn, H.J.M. Bouwmeester, W.A. Meulenberg, O. Guillon, Structural and functional properties of $SrTi1-xFexO3-\delta$ ($0 \le x \le 1$) for the use as oxygen transport membrane, Separation and Purification Technology 147 (2015) 414-421.
- [25] V. Metlenko, W. Jung, S.R. Bishop, H.L. Tuller, R.A. De Souza, Oxygen diffusion and surface exchange in the mixed conducting oxides SrTi(1-y)Fe(y)O(3-delta), Physical chemistry chemical physics: PCCP 18(42) (2016) 29495-29505.
- [26] V.V. Kharton, A.V. Kovalevsky, A.P. Viskup, J.R. Jurado, F.M. Figueiredo, E.N. Naumovich, J.R. Frade, Transport Properties and Thermal Expansion of Sr0.97Ti1–FexO3–(x=0.2–0.8), Journal of Solid State Chemistry 156(2) (2001) 437-444.
- [27] W. Jung, H.L. Tuller, Impedance study of SrTi1–xFexO3–δ (x=0.05 to 0.80) mixed ionic-electronic conducting model cathode, Solid State Ionics 180(11-13) (2009) 843-847.
- [28] Y. Liu, S. Baumann, F. Schulze-Küppers, D.N. Mueller, O. Guillon, Co and Fe co-doping influence on functional properties of SrTiO3 for use as oxygen transport membranes, Journal of the European Ceramic Society 38(15) (2018) 5058-5066.
- [29] X. Li, H. Zhao, N. Xu, X. Zhou, C. Zhang, N. Chen, Electrical conduction behavior of La, Co co-doped SrTiO3 perovskite as anode material for solid oxide fuel cells, International Journal of Hydrogen Energy 34(15) (2009) 6407-6414.
- [30] Z. Zhao, R.V. Goncalves, S.K. Barman, E.J. Willard, E. Byle, R. Perry, Z. Wu, M.N. Huda, A.J. Moulé, F.E. Osterloh, Electronic structure basis for enhanced overall water splitting photocatalysis with aluminum doped SrTiO3 in natural sunlight, Energy & Environmental Science 12(4) (2019) 1385-1395.
- [31] M.A.K.Y. Shah, Y. Lu, N. Mushtaq, M. Yousaf, S. Rauf, M.I. Asghar, P.D. Lund, B. Zhu,

- Perovskite Al-SrTiO3 semiconductor electrolyte with superionic conduction in ceramic fuel cells, Sustainable Energy & Fuels 6(16) (2022) 3794-3805.
- [32] G. He, W. Liang, C.L. Tsai, X. Xia, S. Baumann, H. Jiang, W.A. Meulenberg, Chemical Environment-Induced Mixed Conductivity of Titanate as a Highly Stable Oxygen Transport Membrane, iScience 19 (2019) 955-964.
- [33] M.L. Weber, M. Wilhelm, L. Jin, U. Breuer, R. Dittmann, R. Waser, O. Guillon, C. Lenser, F. Gunkel, Exsolution of Embedded Nanoparticles in Defect Engineered Perovskite Layers, ACS Nano 15(3) (2021) 4546-4560.
- [34] N. Xu, J. Zhang, S. Su, J. Feng, Z. Xu, Preparation and bifunctional properties of the Asite-deficient SrTi(0.3)Fe(0.6)Ni(0.1)O(3-delta) perovskite, RSC advances 12(52) (2022) 33789-33800.
- [35] T. Zhu, H.E. Troiani, L.V. Mogni, M. Han, S.A. Barnett, Ni-Substituted Sr(Ti,Fe)O3 SOFC Anodes: Achieving High Performance via Metal Alloy Nanoparticle Exsolution, Joule 2(3) (2018) 478-496.
- [36] D. Papargyriou, D.N. Miller, J.T. Sirr Irvine, Exsolution of Fe–Ni alloy nanoparticles from (La,Sr)(Cr,Fe,Ni)O3 perovskites as potential oxygen transport membrane catalysts for methane reforming, Journal of Materials Chemistry A 7(26) (2019) 15812-15822.
- [37] J. Wang, D. Kalaev, J. Yang, I. Waluyo, A. Hunt, J.T. Sadowski, H.L. Tuller, B. Yildiz, Fast Surface Oxygen Release Kinetics Accelerate Nanoparticle Exsolution in Perovskite Oxides, Journal of the American Chemical Society 145(3) (2023) 1714-1727.
- [38] Y. Liu, V. Motalov, S. Baumann, D. Sergeev, M. Müller, Y.J. Sohn, O. Guillon, Thermochemical stability of Fe- and co-functionalized perovskite-type SrTiO3 oxygen transport membrane materials in syngas conditions, Journal of the European Ceramic Society 39(15) (2019) 4874-4881.
- [39] E. Forster, D. van Holt, M.E. Ivanova, S. Baumann, W.A. Meulenberg, M. Müller, Stability of ceramic materials for H2 transport membranes in gasification environment under the influence of gas contaminants, Journal of the European Ceramic Society 36(14) (2016) 3457-3464.
- [40] D.T.T. Phuong, L.V. Hong, N.V. Minh, SrTi1-xNixO3 nanoparticles: synthesis and characterisation, International Journal of Nanotechnology 8(3-5) (2011) 312-323.

- [41] A. Mizera, E. Drożdż, Studies on structural, redox and electrical properties of Ni-doped strontium titanate materials, Ceramics International 46(15) (2020) 24635-24641.
- [42] G.A. Alna'washi, A.M. Alsmadi, I. Bsoul, B. Salameh, G.M. Alzoubi, M. Shatnawi, S.M. Hamasha, S.H. Mahmood, Investigation on X-ray photoelectron spectroscopy, structural and low temperature magnetic properties of Ni-Ti co-substituted M-type strontium hexaferrites prepared by ball milling technique, Results in Physics 28 (2021) 104574.
- [43] S. Molin, W. Lewandowska-Iwaniak, B. Kusz, M. Gazda, P. Jasinski, Structural and electrical properties of Sr(Ti, Fe)O3-δ materials for SOFC cathodes, Journal of Electroceramics 28(1) (2012) 80-87.
- [44] A. Rothschild, S.J. Litzelman, H.L. Tuller, W. Menesklou, T. Schneider, E. Ivers-Tiffée, Temperature-independent resistive oxygen sensors based on SrTi1–Fe O3– solid solutions, Sensors and Actuators B: Chemical 108(1-2) (2005) 223-230.
- [45] K. Shan, D. Dastan, Z.Z. Yi, M.K.A. Mohammed, X.T. Yin, A. Timoumi, A.S. Weidenbach, Conductivity and aging behavior of Sr(Ti(0.6)Fe(0.4))(1-x) O(3-delta) mixed conductor materials, RSC advances 13(13) (2023) 8683-8691.
- [46] S.-L. Zhang, H. Wang, M.Y. Lu, A.-P. Zhang, L.V. Mogni, Q. Liu, C.-X. Li, C.-J. Li, S.A. Barnett, Cobalt-substituted SrTi0.3Fe0.7O3–δ: a stable high-performance oxygen electrode material for intermediate-temperature solid oxide electrochemical cells, Energy & Environmental Science 11(7) (2018) 1870-1879.
- [47] M. Balaguer, S. Escolástico, J.M. Serra, Oxygen permeation and stability of CaTi0.73Fe0.18Mg0.09O3-δ oxygen-transport membrane, Journal of Membrane Science 524 (2017) 56-63.
- [48] K. Li, H. Zhao, Y. Lu, Y. Ma, Z. Du, Z. Zhang, High CO2 tolerance oxygen permeation membranes BaFe0.95-xCa0.05TixO3-8, Journal of Membrane Science 550 (2018) 302-312.
- [49] T. Nagai, W. Ito, T. Sakon, Relationship between cation substitution and stability of perovskite structure in SrCoO3–δ-based mixed conductors, Solid State Ionics 177(39) (2007) 3433-3444.
- [50] P. Zeng, Z. Shao, S. Liu, Z.P. Xu, Influence of M cations on structural, thermal and electrical properties of new oxygen selective membranes based on SrCo0.95M0.05O3–δ perovskite, Separation and Purification Technology 67(3) (2009) 304-311.

- [51] J. Yang, H. Zhao, X. Liu, Y. Shen, L. Xu, Bismuth doping effects on the structure, electrical conductivity and oxygen permeability of Ba0.6Sr0.4Co0.7Fe0.3O3–δ ceramic membranes, International Journal of Hydrogen Energy 37(17) (2012) 12694-12699.
- [52] F. Yang, H. Zhao, J. Yang, M. Fang, Y. Lu, Z. Du, K. Świerczek, K. Zheng, Structure and oxygen permeability of BaCo0.7Fe0.3–In O3– ceramic membranes, Journal of Membrane Science 492 (2015) 559-567.
- [53] Z. Wang, N. Dewangan, S. Das, M.H. Wai, S. Kawi, High oxygen permeable and CO2-tolerant SrCoxFe0.9-xNb0.1O3- δ (x = 0.1–0.8) perovskite membranes: Behavior and mechanism, Separation and Purification Technology 201 (2018) 30-40.
- [54] J.W. Stevenson, T.R. Armstrong, R.D. Carneim, L.R. Pederson, W.J. Weber, Electrochemical Properties of Mixed Conducting Perovskites La1 x M x Co1 y Fey O 3 δ (M = Sr, Ba, Ca), Journal of The Electrochemical Society 143(9) (1996) 2722.
- [55] T. Nakamura, G. Petzow, L.J. Gauckler, Stability of the perovskite phase LaBO3 (B = V, Cr, Mn, Fe, Co, Ni) in reducing atmosphere I. Experimental results, Materials Research Bulletin 14(5) (1979) 649-659.

Chapter 3

3. Functional properties of highly stable $SrTi_{0.95-x}Zr_{0.05}Ni_xO_{3-\delta}$ for use as oxygen transport membranes

Abstract

Mixed ionic-electronic conducting ceramics have the potential to serve as oxygen transport membranes, thereby facilitating the separation of pure oxygen from air for a variety of chemical conversion applications. Given that the majority of the membrane reactors are operated in a reducing atmosphere, the stability of the materials is of great importance. In this study, the $SrTi_{0.95-x}Zr_{0.05}Ni_xO_{3-\delta}$ (x=0.01, 0.03, 0.05, 0.10, 0.15) (STZN_x) powders were successfully synthesized and subsequently sintered into membranes. Ni substitution enhances oxygen permeability and catalytic activity via exsolution, while Zr improves structural stability by minimizing cation mismatch. XRD results indicate a Ni solubility limit below 15 mol%. An increase in the Ni content results in a corresponding enhancement in oxygen permeability, with STZN10 achieving the highest oxygen permeability while retaining a single phase. Thermochemical stability tests were conducted by annealing samples in a reducing atmosphere containing 2.9 vol% H₂ in Ar. The XRD and thermogravimetric analysis (TGA) demonstrate that STZN_x displays remarkable stability in reducing atmospheres. The presence of well-distributed Ni particles on the surface of STZN10 is observed after annealing in 2.9 vol% H₂/Ar at 900°C for 48 h, proving the successful exsolution phenomenon aiming for improved catalytic activity for applications such as partial oxidation of methane. It can therefore be concluded that 10 mol% Ni-doped STZN10 is a promising material for oxygen transport membranes in catalytic membrane reactors.

This chapter has been published as: Y. Tang, S. Baumann, A. Nijmeijer, O. Guillon, W.A. Meulenberg, Functional properties of highly stable SrTi_{0.95-x}Zr_{0.05}Ni_xO₃₋₆ for use as oxygen transport membranes, Journal of the European Ceramic Society 45(16) (2025) 117715, DOI: https://doi.org/10.1016/j.jeurceramsoc.2025.117715

3.1 Introduction

Oxygen is a very important gas that can be widely applied in different industrial areas. Despite the large availability of oxygen in the air, the process of separating it into a pure form requires a significant input of energy. The principal industrial techniques for the production of pure oxygen are cryogenic distillation and pressure swing adsorption (PSA), both of which require significant investment and operational expenses [1]. Ceramic materials that exhibit both ionic and electronic conductivity are well-regarded for their good performance in oxygen transport membranes (OTMs), which have been developed for a variety of energy applications, including air separation to produce pure oxygen for oxyfuel combustion [2] and medical purposes [3]. Additionally, the membranes can be utilized in membrane reactors for the production of commodity chemicals through a range of industrial reaction systems, including the water splitting [4, 5], selective oxidation of ethane [6], oxidative coupling of methane [7], and partial oxidation of methane [8, 9]. In the context of membrane reactor operating conditions, the gas environment typically contains CO, CO₂, H₂, or CH₄. Consequently, the membranes must exhibit high chemical stability under reducing environments. Strontium titanate (SrTiO₃), a highly stable perovskite material, typically exhibits dielectric properties. However, its electrical properties can be significantly altered through A/B-site doping. The potential for oxygen vacancies and electronic defects formation enables doped SrTiO₃ to conduct oxide ions, thus rendering it a mixed ionic-electronic conductor (MIEC) for use as OTM. Over the past decade, a variety of elements have been incorporated as dopants into the Sr or Ti sites of strontium titanate, such as Fe [10, 11], Co [12, 13], Al [14-16], Mg [17] and so on. However, the introduction of defects into the crystal lattice through doping can also result in the deterioration of stability. Cobalt-doped STO₃ can significantly enhance the oxygen permeability, but its stability remains a significant challenge [18]. Schulze-Küppers et al. [10] investigated the functional properties of SrTi_{1-x}Fe_xO_{3-δ}. The findings suggest that the Fe content of 25–35 mol% seems promising with considering the trade-off between stability and oxygen permeability. He et al. [17] identified a highly stable material SrMg_{0.15}Zr_{0.05}Ti_{0.8}O₃₋₈ (SMZ-Ti), which showed a good environment-induced oxygen permeation performance. The membrane can facilitate water splitting on one side while utilizing the permeated oxygen on the other side for methane reforming.

It is noteworthy that if the dopant element can exist in multiple oxidation states, the doped materials may also function as active catalytic centers [19]. Ni can adopt multiple oxidation states when incorporated into the titanium sublattice, like Ni²⁺, Ni³⁺ and Ni⁴⁺. This not only facilitates the modification of the material's electrical properties as a dopant but also renders it an active site for redox reactions on the surface of Ni-doped SrTiO₃ due to the associated valence change [20]. The phenomenon of Ni exsolution in reducing atmospheres has abundantly been reported in literature [21-25]. The synthesis and study of pure Ni-doped strontium titanate have been conducted by several researchers [20, 26, 27]. Nevertheless, the permeance as oxygen transport membrane materials has not yet been systematically characterized. For practical applications, especially under high-temperature or reducing environments, structural stability becomes a critical factor. In such conditions, the mismatch in ionic radii and valence states among B-site cations can lead to lattice distortions and phase instability. To mitigate this, Zr⁴⁺ is introduced as a co-dopant. With its high valence and excellent resistance to reduction, Zr⁴⁺ helps stabilize the cubic perovskite structure [17], thereby enhancing the material's suitability for demanding environments such as membrane reactors. Moreover, Zr typically exists in the Zr⁴⁺ oxidation state, with an ionic radius of 0.72 Å, which is larger than that of Ti^{4+} (0.605 Å) and Ti^{3+} (0.67 Å). As a result, incorporating Zr into the perovskite structure can not only minimize cation mismatch and stabilize the cubic structure, but also increase the lattice parameters of STO [17]. Therefore, we here study $SrTi_{0.95-x}Zr_{0.05}Ni_xO_{3-\delta}$ (x=0.01, 0.03, 0.05, 0.10, 0.15) (STZN_x) aiming at high stability. The structure of the various materials has been characterized, and their permeability and electrical conductivity have been determined. Furthermore, the chemical stability and Ni exsolution phenomenon in reducing atmosphere (2.9 vol% H₂/Ar) were investigated.

3.2 Experimental

3.2.1 Powder preparation

Series of Ni-doped strontium titanates $SrTi_{0.95-x}Zr_{0.05}Ni_xO_{3-\delta}$ (STZN_x), with x=0.01, 0.03, 0.05, 0.10, 0.15, were prepared by a solid-state reaction method. For convenience,

SrTi_{0.94}Zr_{0.05}Ni_{0.01}O_{3-δ} is represented as STZN1 and so on in the following content. For the first step, SrCO₃ (Merck, 99%), TiO₂ (Merck, 99%), ZrO₂ (Merck, 99%) and NiO (Merck, 99%) powder were mixed with 3 mm Y-stabilized ZrO₂ milling balls and ethanol in a polyethylene bottle, and then homogenized on a roller bench for 48 h. The mass proportions of powder, ethanol, and balls were kept at a ratio of 1:2:3. The mixture was dried at 70 °C after milling and then sieved through 250 μm mesh. The calcination step was conducted at 1200 °C for 5 h. The powder obtained after calcination was ball milled, dried and sieved again with the same parameters as before. The bulk membranes were formed into discs using a PW10 uniaxial press (Ø 20 mm) (Fa. Paul Otto Weber GmbH, Remshalden), applying a pressure of 70 MPa for 1.5 min. 4 wt.% polyvinyl alcohol was added as binder to the mixture prior to pressing. The pressed STZN_x membranes were subsequently sintered at 1500 °C for 5 h, with heating and cooling rates of 5 K/min.

3.2.2 Characterization methods

The particle size distribution of all the powders was measured by a particle analyzer HORIBA LA-950V2 (Horiba European GmbH, Germany). The crystal structures and phase compositions were analyzed based on X-ray diffraction (XRD) using a D4 ENDEAVOR diffractometer (Bruker, Germany) with Cu K α radiation. The diffraction angle (2 θ) was scanned over a range of 10° to 80° with a step size of 0.02° and a dwell time of 0.75 s per step. Rietveld refinement analysis (Topas, Bruker, Germany) was carried out to determine the quantitative compositions and lattice parameters of the materials. The microstructure of the surface and cross section was observed via scanning electron microscopy (SEM) (Zeiss GeminiSEM 450) coupled with energy dispersive X-ray spectroscopy (EDS, Ultim Max 170, Oxford Instruments). A thin platinum layer was sputter-deposited onto the samples to improve their electronic conductivity before analysis. X-ray photoelectron spectroscopy (XPS) was performed using a PHI 5000 VersaProbe II system (ULVAC-PHI Inc., USA) equipped with a monochromatic Al K α X-ray source (hv = 1486.6 eV). The X-ray was operated at 50 W and 15 kV with a spot size of 200 μ m. Survey spectra were acquired with a pass energy of 187.5 eV, a step size of 0.8 eV, and a dwell time of 100 ms/step. High-resolution spectra were recorded

with a pass energy of 23.5 eV, a step size of 0.1 eV, and a dwell time of 100 ms/step. Charge correction was applied by referencing the main C 1s peak to 285.0 eV. Cyclic thermogravimetric analysis (TGA) was performed using a STA449 F1 Jupiter calorimeter coupled with a QMS 403C Aëolos (Netzsch) mass spectrometer under air and 2.9 vol% H₂/Ar atmospheres. The analysis was conducted up to a final temperature of 900 °C, with a heating and cooling rate of 10 K/min, and a gas flow rate of 50 mL/min. Each cycle included a holding time of 2 h for both the reduction and oxidation stages. The annealing experiments were carried out at 900 °C in reducing atmospheres (2.9 vol% H₂/Ar) for durations of 10 hours and 48 hours, respectively, with the heating and cooling rates of 5 °C/min. The surface changes of sintered pellets (Ø 8 mm x 5 mm) were investigated before and after annealing. All fresh synthesized pellets were gas-tight, which has been confirmed by a He-leak rate detector (Qualy test HTL 260, Pfeiffer Vacuum GmbH, Asslar, Germany).

3.2.3 Electrical conductivity

The total electrical conductivity (σ_t) was analyzed by electrochemical impedance spectroscopy (EIS) in air and Ar using an Alpha-A high performance frequency analyzer (Novocontrol Technologies, Germany). The measurements were conducted between 300 °C and 900 °C in a frequency range of 10^6 Hz to 10^{-1} Hz with three measurements per temperature step. Each temperature was maintained for 1 h before measurements to ensure equilibration of the oxygen vacancy concentration. The pellets ($\varnothing 8$ mm x 5 mm) were prepared by polishing the surfaces of a cylindrical specimen using 2500-grit sandpaper. Pt paste was brushed on both sides of the pellets and sintered at 900 °C for 1 h to prepare Pt electrodes. The total conductivity σ_t of the sample was obtained according to equation (3.1):

$$\sigma_t = \frac{1}{R} \cdot \frac{l}{A} \tag{3.1}$$

Where R is the resistance (Ω) from the impedance spectroscopy, A is the electrode area (cm²), and l is the sample thickness (cm).

The activation energy E_a was calculated according to Arrhenius equation (3.2):

$$\ln(\sigma_t \cdot T) = -\frac{E_a}{RT} + A \tag{3.2}$$

Where *T* is temperature (K), *R* is the ideal gas constant (8.31446261815324 $J \cdot K^{-1} \cdot mol^{-1}$), *A* is a constant.

3.2.4 Oxygen permeation measurement

A 4-end mode set up was applied for the oxygen permeation experiments. The membranes were ground to approx. \varnothing 14.6 mm, polished to 1 mm thickness with 2500-grit sandpaper, and then sealed by two gold rings (\varnothing 13 mm) on the both sides in a vertical quartz glass housing. The measurements were conducted in air (250 mL min⁻¹) or pure O₂ (200 mL·min⁻¹) at the feed side from 1000 °C to 800 °C, respectively. Inert gas Ar was used as sweep gas at the permeate side with a flow rate of 50 mL·min⁻¹ when the feed gas was air or O₂. The flow rate was controlled using mass flow controllers (MFCs, Bronkhorst, Germany). The concentration of O₂ and N₂ in the permeate gas was detected by a mass spectrometer (Omni Star, Pfeiffer Vacuum GmbH, Germany).

Oxygen transport is generally limited by either surface exchange reactions or bulk diffusion, depending on the membrane thickness (L). The key distinction between both limiting steps is the characteristic membrane thickness (L_c) [28-30]. If $L \gg L_c$, the transport is assumed to be only limited by bulk diffusion. According to literature studies, the characteristic thickness L_c for bulk-diffusion-limited oxygen transport in perovskite-type membranes is typically lower than 200 μ m [10, 31, 32]. Since our membranes are significantly thicker (1 mm), it is reasonable to assume that the oxygen flux is primarily governed by bulk diffusion. The oxygen flux $j(O_2)$ in dense membranes is commonly described using a well-established model based on Wagner's theory in this case, which is typically expressed in the form of the standard Wagner equation [33, 34] (equation (3.3)):

$$j(O_2) = \frac{R}{16F^2 \cdot L} \cdot T \cdot \sigma_{amb} \cdot \ln \frac{p'_{O_2}}{p''_{O_2}}$$
(3.3)

where R corresponds to the ideal gas constant, F is the Faraday constant, L is the thickness of the membrane, T is the membrane temperature, p'_{o_2} and p''_{o_2} are the oxygen partial pressure for oxygen rich and lean side of the membrane, respectively, and σ_{amb} is the ambipolar conductivity, given by equation (3.4):

$$\sigma_{amb} = \frac{\sigma_i \cdot \sigma_e}{\sigma_i + \sigma_e} \tag{3.4}$$

Where σ_i is the ionic conductivity and σ_e is the electronic conductivity. The ionic conductivity σ_i can be estimated with the respective ionic transference number t_i according to equation (3.5-3.7).

$$\sigma_t = \sigma_i + \sigma_e \tag{3.5}$$

$$\frac{\sigma_{amb}}{\sigma_t} = t_i (1 - t_i) \tag{3.6}$$

$$\sigma_i = \sigma_t \cdot t_i \tag{3.7}$$

In the MIEC, if $\sigma_e >> \sigma_i$, $\sigma_e \approx \sigma_t$, $\sigma_i \approx \sigma_{amb}$. The activation energy of σ_i was calculated as the same way as σ_t (equation (3.2)).

The driving force for OTMs is the gradient in oxygen partial pressure at the two sides of the membrane. Since the oxygen partial pressure depends on temperature, the driving force varies during the measurement. Therefore, the permeance, as discussed in Chapter 1, can be determined by normalizing the oxygen flux $j(O_2)$ with the oxygen partial pressure gradient $\left(\ln \frac{p'_{O_2}}{p''_{O_2}}\right)$, and is defined as equation (3.8):

$$Permeance = \frac{j(O_2)}{\ln \frac{p'_{O_2}}{p''_{O_2}}} = \frac{R}{16F^2 \cdot L} \cdot T \cdot \sigma_{amb}$$
(3.8)

$$ln(permeance) = -\frac{E_a}{RT} + A$$
(3.9)

The activation energy of permeance can be obtained by the Arrhenius approach (equation (3.9)), where R is the ideal gas constant and A is the pre-exponential factor.

3.3 Results and discussion

3.3.1 Crystal structure and microstructure

The d_{50} values of all the as-synthesized STZN_x powders are around 1 μm (Table 3.1). The XRD patterns (Figure 3.1) of all samples show a cubic perovskite structure (Pm3m), which was confirmed by Rietveld refinement. For the STZN15 sample, the XRD pattern shows a secondary phase with reflections corresponding to NiO, indicating that nickel is only partially dissolved into the perovskite structure during synthesis. This suggests that the solubility limit of Ni in perovskitic STZN is below 15 mol%. Figure 3.1(b) presents an enlarged view of the patterns from 30° to 35°. It is observed that the peaks of STZN_x shift towards higher angles as the Ni content increases, indicating a reduction in the lattice parameter. The cubic lattice parameters of STZN1, STZN3, STZN5, STZN10 and STZN15 are 3.918, 3.917, 3.916, 3.914 and 3.913 Å, respectively, according to the Rietveld refinement. The observed changes of the lattice parameter suggest that the introduced Ni most likely favors multiple oxidation states, including +2 (0.69 Å), +3 (0.56 Å) and +4 (0.48 Å) [20]. The presence of Ni⁴⁺ in a perovskitelike structure has already been confirmed by Takeda et al. in SrNiO₃ [35] and BaNiO₃ [36] compounds. Since STZN15 is not a single-phase material, it is excluded from the following discussion. XPS measurements were carried out to determine the valence of Ni on the membrane surface. As the Ni content of samples STZN1 and STZN3 is below the detection limit, only the results of STZN5 and STZN10 will be discussed (Figure 3.2). The Ni 2p_{3/2} corelevel spectra of samples STZN5 and STZN10 can be satisfactorily fitted using peak components characteristic of Ni(OH)₂ [37], indicating that Ni primarily exists in the Ni²⁺ oxidation state on the membrane surface. However, the presence of Ni³⁺ cannot be entirely excluded, as it may exist in a relatively low concentration and therefore be difficult to detect. The existence of mixed-valence states of Ni in Ni-containing materials has been reported in previous studies, such as NiO/NiFe₂O₄ [38], Li_{0.6}NiO₂ [39], NiCo₂O₄ [40], Li₂NiTiO₄ [41] and Ni-doped Ba_{1-x}Sr_xTiO₃ [42]. The cross-sectional SEM images (Figure 3.3) of the sintered pellets show that all the materials can achieve densification under the given sintering conditions, which is also confirmed by helium leakage experiments ($< 10^{-7} \, \text{mbar} \cdot \text{L} \cdot \text{s}^{-1}$). It is worth noting that the grain size of STZN_x remains on the same scale. Ni has been reported as an effective sintering aid for perovskites [43-45]. The corresponding SEM images clearly indicate that the STZN10 membrane, with 10 mol% Ni doping, is significantly better sintered than the other STZN_x membranes with lower Ni content, further confirming the role of nickel dopant in enhancing membrane sintering.

Table 3.1 Particle size distribution of as-synthesized powders of STZN_x

Name	Composition	d10	d50	d90
Name	Composition	μm	μm	μm
STZN1	$SrTi_{0.94}Zr_{0.05}Ni_{0.01}O_{3\text{-}\delta}$	0.58	1.00	2.17
STZN3	$SrTi_{0.92}Zr_{0.05}Ni_{0.03}O_{3\text{-}\delta}$	0.58	0.99	2.18
STZN5	$SrTi_{0.90}Zr_{0.05}Ni_{0.05}O_{3\delta}$	0.54	0.96	2.58
STZN10	$SrTi_{0.85}Zr_{0.05}Ni_{\ 0.10}O_{3\delta}$	0.55	1.02	3.09

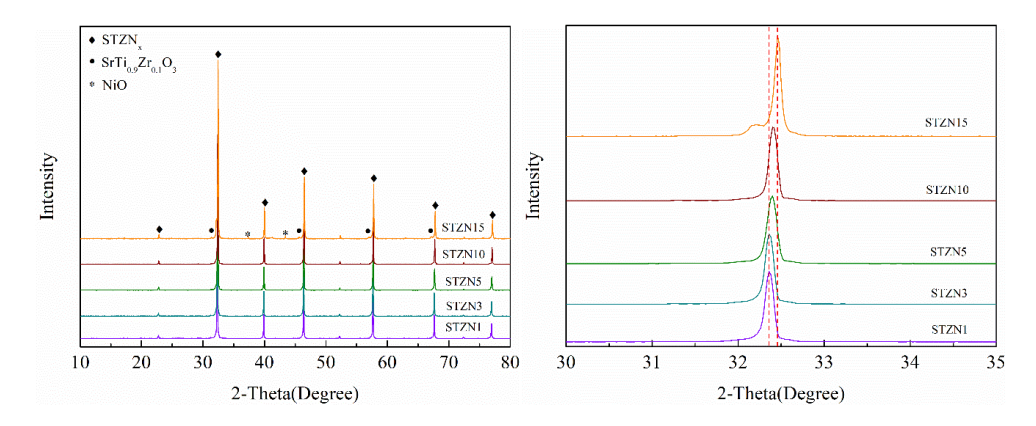


Figure 3.1 XRD patterns of the as-synthesized membranes of STZN_x

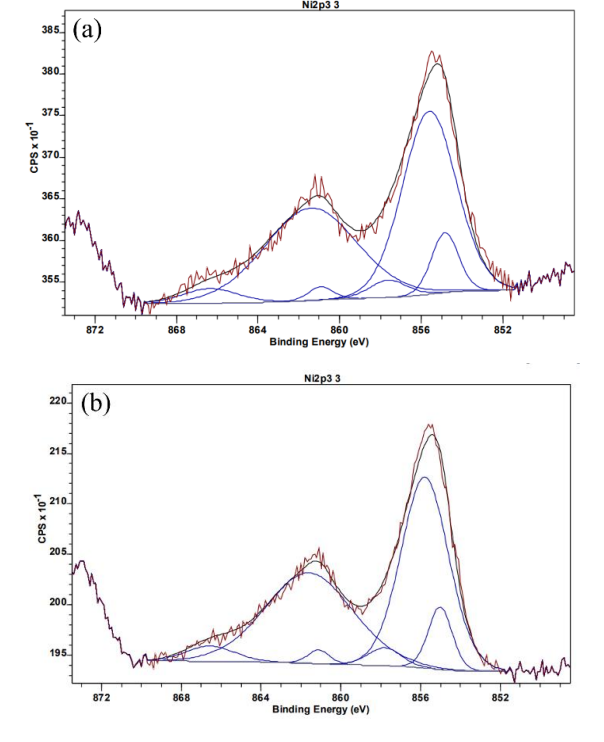


Figure 3.2 XPS spectra of Ni 2p 3/2 of (a) STZN5 and (b) STZN10

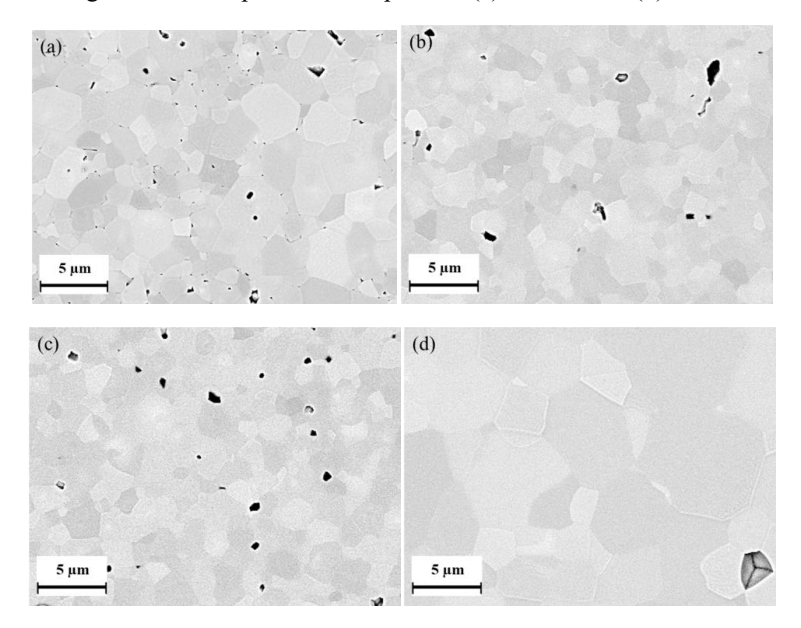


Figure 3.3 Cross-section of the as-synthesized membranes of (a) STZN1, (b) STZN3, (c) $STZN5 \ and \ (d) \ STZN10$

3.2 Functional properties

3.2.1 Electrical conductivity

The electrical conductivity of $STZN_x$ was calculated according to the EIS results. The conductivity increases with the Ni content increasing and the value in air (p_{O2} =0.2 atm) is higher than that in Ar ($\sim p_{O2}$ =10⁻⁵ atm) (Figure 3.4). It is reported that $SrTiO_3$ shows p-type conductivity at this oxygen partial pressure range [46]. In the p-type region, doped $SrTiO_3$ is a mixed conductor of oxygen vacancies and holes, however, with the hole conduction being dominant. Materials can generate more positive holes in air than in Ar due to the equation (3.10) [47]:

$$\frac{1}{2}O_2 + V_O^{\cdot \cdot} = O_O^{\times} + 2h^{\cdot} \tag{3.10}$$

where V_O^* , O_O^* and h^* represents an oxygen vacancy, an oxygen ion occupying an oxygen lattice site, and an electron hole, respectively. The superscripts \times and \cdot denote an electroneutral state and one positive effective charge, respectively. Table 3.2 lists the electrical conductivity of STZN_x at 900 °C and the activation energy in the application relevant temperature range 600-900 °C in air and Ar. The activation energy ranges from 60.88 kJ/mol to 100.81 kJ/mol in both atmospheres, with the value in Ar being higher than that in air.

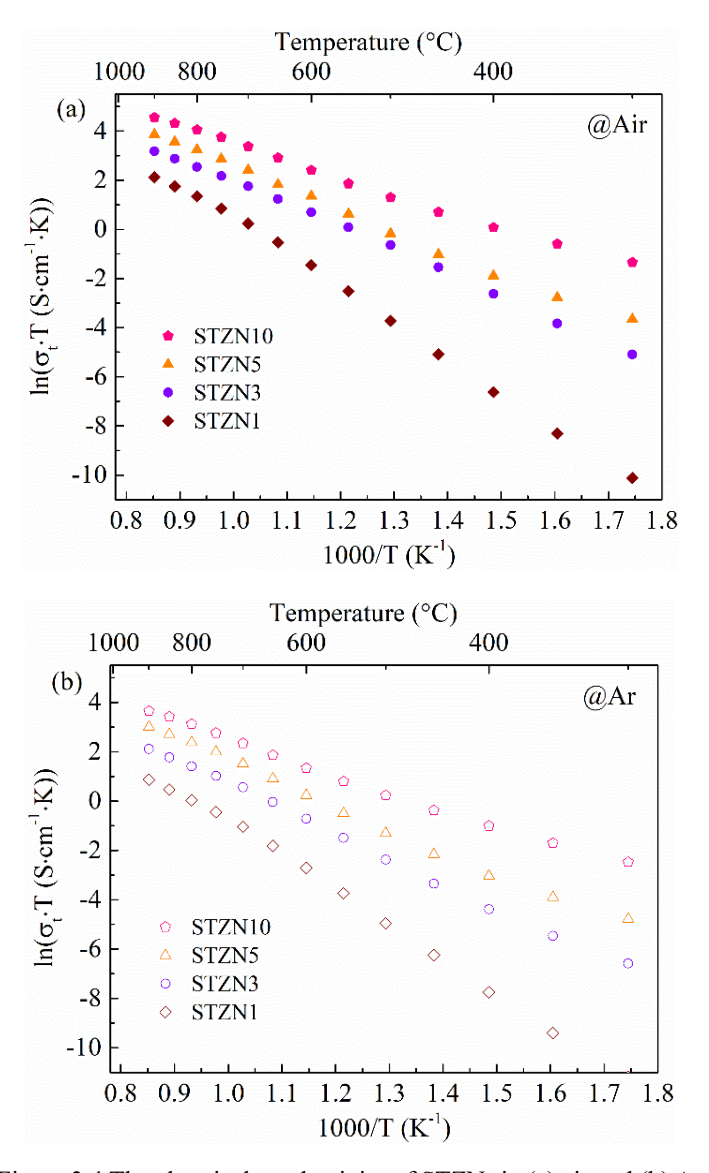


Figure 3.4 The electrical conductivity of STZN_x in (a) air and (b) Ar

Table 3.2 Electrical conductivity σ_t of STZN_x at 900 °C and activation energy E_a

Name	σ_t _Air	E _{a_} Air (600-900 °C)	σ_{t} _Ar 900 °C	E _a _Ar (600-900 °C)
	(S/cm)	(kJ/mol)	(S/cm)	(kJ/mol)
STZN1	7.1×10 ⁻³	101	2.0×10 ⁻³	101
STZN3	2.1×10 ⁻²	71	7.1×10 ⁻³	80
STZN5	4.1×10 ⁻²	72	1.7×10 ⁻²	78
STZN10	8.1×10 ⁻²	61	3.3×10 ⁻²	66

3.2.2 Oxygen permeation

Oxygen permeation through ceramic membranes involves two primary processes [41]: gassolid interfacial exchange occurring at the surface (surface exchange) and ion/electron transport within the bulk. For the 1 mm thick membranes, the oxygen permeation process is typically limited by bulk diffusion. Figure 3.5(a) compares the oxygen flux of STO and STZN_x measured under air/Ar (feed side/sweep side) and O₂/Ar conditions. The oxygen flux of STZN_x is higher than that of pure STO [10] and increases with increasing Ni content. Since the permeability of STZN1 and STZN3 is in a very low range, only STZN5 and STZN10 were tested in the O₂/Ar atmosphere for the following discussion. In addition, Figure 3.5(a) indicates that the oxygen flux of STZN5 and STZN10 is higher in O₂/Ar compared to air/Ar due to the higher oxygen partial pressure gradient. The oxygen permeance, i.e. driving force-normalized oxygen permeation, is shown in Figure 3.5(b). STZN5 and STZN10 can maintain similar values in two different conditions, confirming that the Wagner equation is applicable and, thus, bulk diffusion is the dominating transport mechanism. Table 3.3 compares the oxygen flux, permeance and activation energy E_a of STZN_x with other doped-STO₃ materials from literature at 1000 °C in air/Ar-gradients. The Ea values of STO (353 kJ mol⁻¹) and STZN1 (236 kJ mol⁻¹) are significantly higher than those of STZN3 (108 kJ mol⁻¹), STZN5 (98 kJ·mol⁻¹), and STZN10 (103 kJ·mol⁻¹). The significantly higher activation energy of the former samples is typically attributed to surface exchange limitations. Additionally, the oxygen permeation performance of STZN10 is found to be lower than that of other B-site doped STO₃ samples reported in the literature, such as Fe-doped STO₃ material SrTi_{1-x}Fe_xO_{3-δ} (STF_x) [10], cobalt-doped STO₃ material SrTi_{1-x}Co_xO_{3-δ} (STC_x) [13] and Fe/Ni co-doped STO₃ material SrTi_{0.65-x}Fe_{0.35}Ni_xO_{3-δ} (STFN_x) [48], with the exception of SrMg_{0.15}Zr_{0.05}Ti_{0.8}O_{3-δ} (SMZ-Ti) [17]. Although the oxygen flux of STZN10 is lower than that of most B-site doped STO₃ materials, it can be improved through various strategies, such as the improvement of the oxygen partial pressure gradient across both sides of the membrane to a certain extent based on specific applications, the reduction of membrane thickness, the fabrication of asymmetric membranes, or the addition of a catalytic layer to the material's surface.

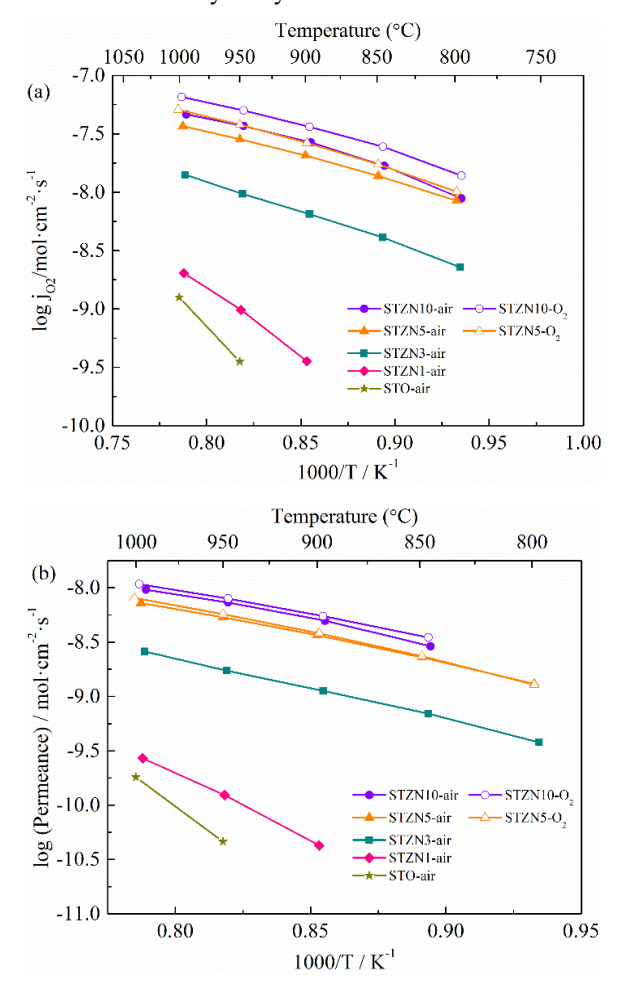


Figure 3.5 (a) Flux in air and O2 and (b) Permeance of 1 mm thickness of STZNx

Table 3.3 Oxygen flux, permeance and activation energy of $STZN_x$ and doped- STO_3 materials at 1000 °C in air

	Oxygen flux	Log	Ea of	Thicknes	Ref.
	mL·cm-	(Permeance)	Permeance	s	
Composition	² ·min ⁻¹	mol·cm ⁻² ·s ⁻¹	(800-	(mm)	
			1000 °C)		
			kJ·mol⁻¹		
SrTiO ₃ (STO)	1.85×10 ⁻³	-9.74	353	1	[10]
$SrTi_{0.75}Fe_{0.25}O_{3\delta}\left(STF25\right)$	2.15×10 ⁻¹	-7.44	89	1	[10]
$SrTi_{0.75}Co_{0.25}O_{3-\delta}$ (STC25)	-	-7.45	79	1	[13]
$SrTi_{0.65}Co_{0.35}O_{3-\delta}$ (STC35)	-	-7.08	65	1	[13]
$SrMg_{0.15}Zr_{0.05}Ti_{0.8}O_{3\delta}\left(SMZTi\right)$	2×10 ⁻²	-	-	0.7	[17]
$SrTi_{0.65}Fe_{0.35}O_{3\text{-}\delta} \ (STF35)$	2.46×10 ⁻¹	-7.27	82	1	[48]
$SrTi_{0.6}Fe_{0.35}Ni_{0.05}O_{3-\delta}$	2.78×10 ⁻¹	-7.20	89	1	[48]
(STFN005)					
$SrTi_{0.64}Zr_{0.05}Ni_{0.01}O_{3\delta}$	2.72×10 ⁻³	-9.57	236	1	This
(STZN1)					work
$SrTi_{0.62}Zr_{0.05}Ni_{0.03}O_{3\delta}$	1.89×10 ⁻²	-8.58	108	1	This
(STZN3)					work
C.T. Z. N. O. (CTZNS)	4.09×10 ⁻²	-8.22	98	1	This
$SrTi_{0.6}Zr_{0.05}Ni_{0.05}O_{3-\delta}$ (STZN5)					work
$SrTi_{0.55}Zr_{0.05}Ni_{0.10}O_{3\text{-}\delta}$	6.23×10 ⁻²	-8.02	103	1	This
(STZN10)					work

Figure 3.6 shows the ambipolar conductivity and ionic conductivity of $STZN_x$ in air. The graph shows that both conductivities are of the same order of magnitude and increase with increasing Ni content. The ionic conductivity is slightly higher than the ambipolar conductivity, indicating the electronic conductivity is much higher than the ionic conductivity. Table 3.4 lists the ambipolar conductivity, ionic conductivity and the corresponding activation energy as well as

the respective ionic transference numbers in air. It can be noted that the activation energy of the ambipolar conductivity is lower than the activation energy of the ionic conductivity. Since the ambipolar conductivity is determined by both the ionic conductivity and electronic conductivity of the material, this reduction reflects a significant contribution of electron transport, which lowers the overall activation energy. In addition, the ionic conductivity of the materials is more sensitive to temperature due to its higher activation energy compared to electronic and ambipolar conductivity.

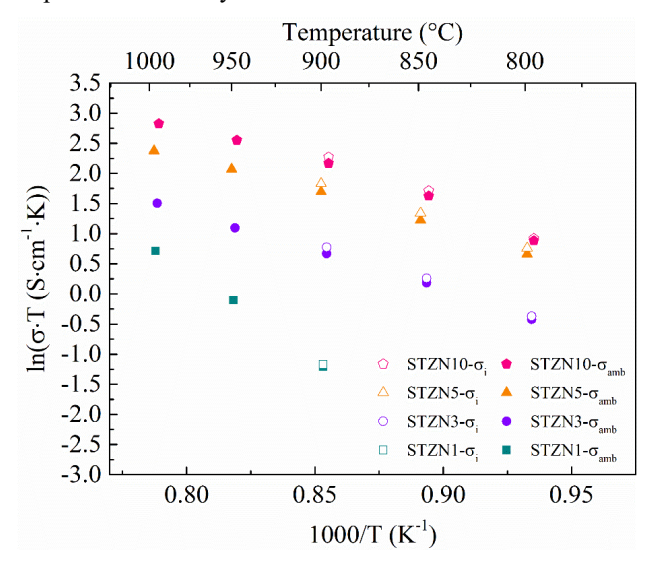


Figure 3.6. Ambipolar conductivity σ_{amb} and ionic conductivity σ_i of STZN_x in air

Table 3.4 Ambipolar conductivity, ionic conductivity, activation energy and respective ionic transference numbers in air

Name	<i>σ_{amb_}</i> Air 900 °C (S/cm)	σ _{i _} Air 900 °C (S/cm)	E_{a} amb $800-1000~^{\circ}C$ (kJ/mol)	E _{a_} ionic 800-900 °C (kJ/mol)	ti_800 °C	ti_900°C
STZN1	2.54×10 ⁻⁴	2.65×10 ⁻⁴	-	-	-	3.75×10 ⁻²
STZN3	1.67×10 ⁻³	1.85×10 ⁻³	108	119	5.44×10 ⁻²	9.02×10 ⁻²
STZN5	4.65×10 ⁻³	5.32×10 ⁻³	98	111	8.42×10 ⁻²	1.31×10 ⁻¹
STZN10	7.48×10 ⁻³	8.30×10 ⁻³	110	141	4.37×10 ⁻²	1.03×10 ⁻¹

3.3.3 Thermo-chemical stability

TG measurements and annealing measurements are designed to evaluate the thermo-chemical stability of the materials.

Figure 3.7 illustrates the mass change over time for different STZN_x samples upon cyclic exposure to air and 2.9 vol% H₂/Ar atmosphere. The mass of all samples is observed to decrease during the periods in the reducing 2.9 vol% H₂/Ar environment (indicated in green) due to oxygen release during reduction of B-site elements, and subsequently recovers due to reoxidation during the air exposure periods (indicated in blue). The mass loss of STZN_x under the reducing condition increases with increasing Ni content. Notably, a two-step mass loss is observed in the STZN10 curve, which can be estimated to the sequential reduction of the same element, such as $Ni^{4+} \rightarrow Ni^{3+} \rightarrow Ni^{2+} \rightarrow Ni$, or the stepwise reduction of the different B-site elements, such as Ni and Ti. Table 3.5 compares the mass loss of STZN_x at different stages. This indicates that the mass loss slightly increases with the number of cycles. But all the values are less than 0.33 wt.%, which is very small. The mass change of all the materials is practically fully reversible confirmed by XRD patterns showing single phase structure after the final reoxidation step of TG measurements (Figure 3.8). Considering the highly reducing conditions of 2.9 vol% H₂/Ar at 900 °C STZN_x materials show excellent cyclic reduction stability. Therefore, STZN10 is identified as a promising candidate for OTMs in membrane reactors, given its excellent stability and the highest oxygen permeability among the STZNx series materials.

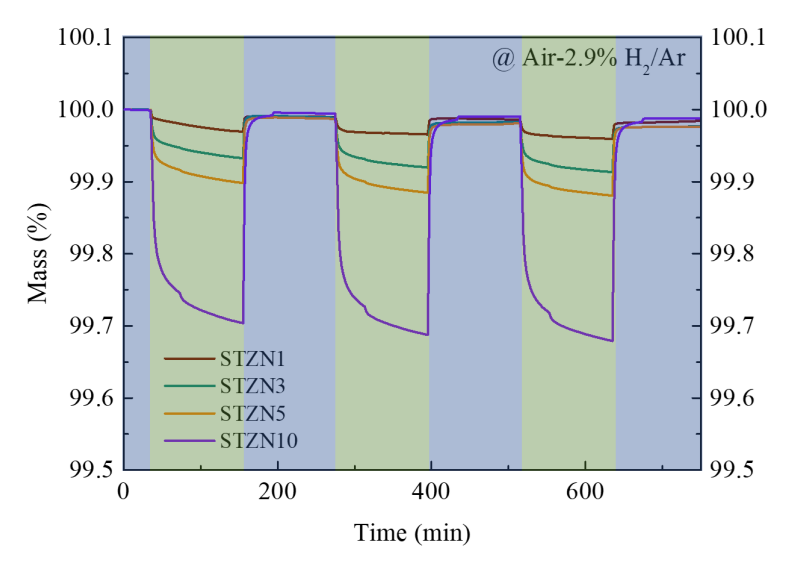


Figure 3.7 Three-cycle TG measurements of $STZN_x$ in air (marked in blue) and 2.9 vol% H_2/Ar atmospheres (marked in green)

Table 3.5 Mass loss of $STZN_x$ at different stages

Commonition	First cycle	Second cycle	Third cycle	Final
Composition	mass loss_H ₂ /Ar	mass loss_H ₂ /Ar	mass loss_H ₂ /Ar	mass loss_air
STZN1	0.030 %	0.035 %	0.041 %	0.017 %
STZN3	0.067 %	0.081 %	0.087 %	0.024 %
STZN5	0.102 %	0.115 %	0.120 %	0.024 %
STZN10	0.296 %	0.313 %	0.321 %	0.013 %

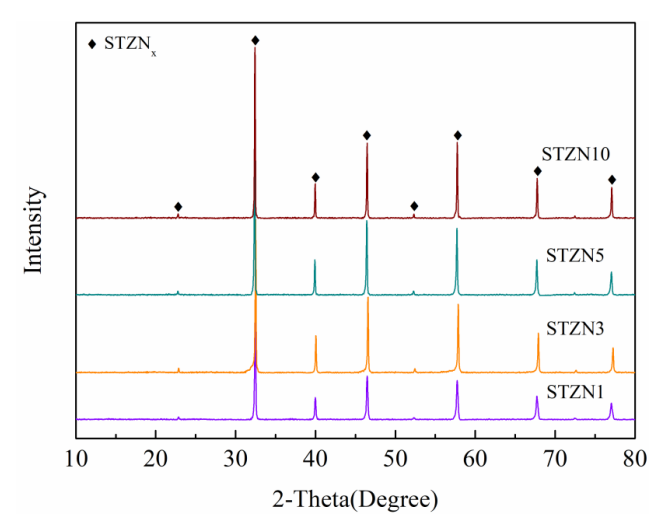


Figure 3.8 XRD patterns of STZN_x after three-cycle TG measurement

Sintered STZN_x pellets were annealed in a 2.9 vol% H₂/Ar atmosphere at 900 °C for either 10 h or 48 h to evaluate their stability under highly reducing conditions. The XRD patterns (Figure 3.9) indicate that all materials still maintain a single-phase structure after annealing demonstrating excellent stability. The surfaces of as-synthesized and annealed STZN10 were characterized using SEM coupled with EDS analysis (Figure 3.10(a-d)). The surface of the sample annealed for 10 h displays a similar morphology to that of the as-synthesized pellets, with no detectable Ni on the surface. However, as the annealing time increases, Ni exsolution becomes obvious on the surface of the sample annealed for 48 h (Figure 3.10(c)), with the exsolved Ni highlighted in yellow in the EDS mapping (Figure 3.10(d)). The prominently bright yellow region in Figure 3.10(d) is attributed to the reduction of a remaining NiO particle, which was not dissolved during powder synthesis. The cross-sectional SEM image (Figure 10(e)) reveals a uniform microstructure without detectable Ni segregation in the bulk of the STZN10 sample after 48 h of annealing.

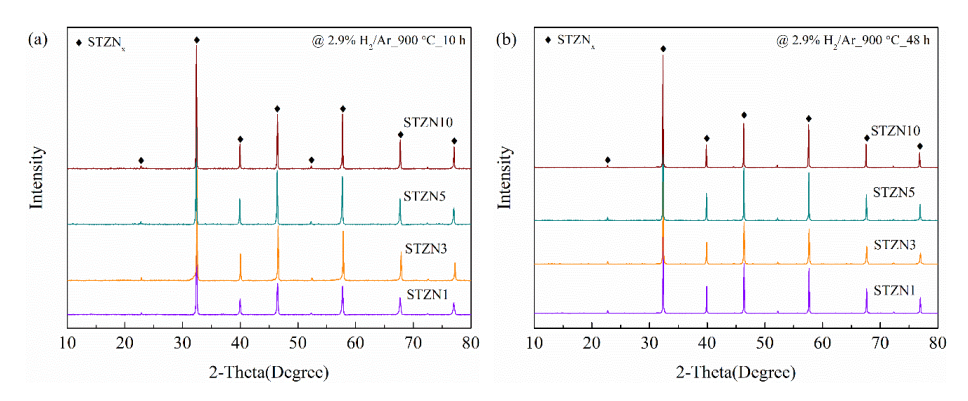
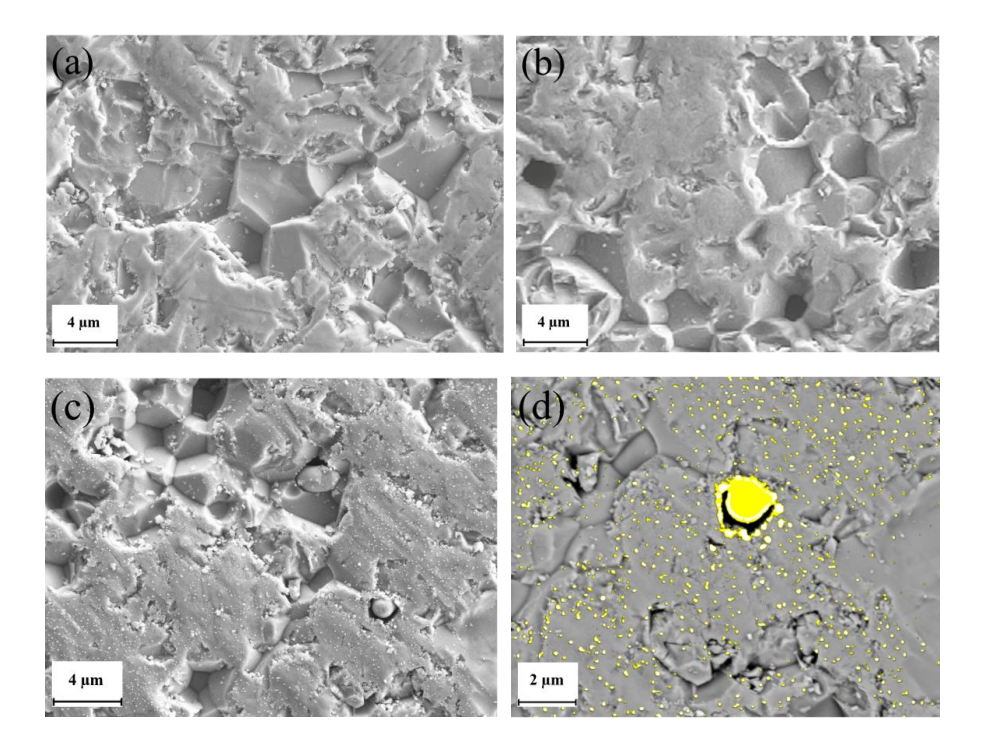


Figure 3.9 XRD patterns of STZNx annealed in 2.9 vol% H_2/Ar at 900 °C for (a) 10 h and (b) 48 h



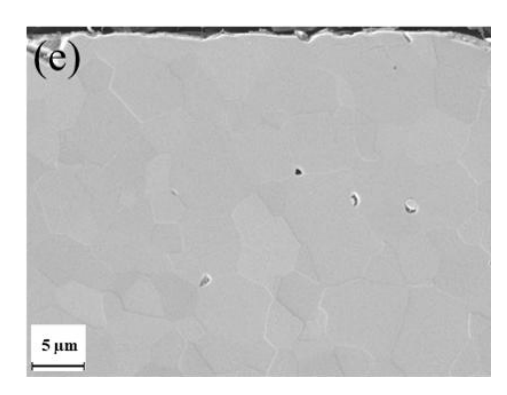


Figure 3.10 Surface and cross-sectional SEM images of STZN10 in different states: (a) assynthesized, (b) annealed for 10 h, (c) annealed for 48 h along with (d) EDS mapping; and (e) cross-section after 48 h of annealing

3.4 Conclusions

This study systematically investigates the microstructures, functional properties and stability of STZN_x series materials for use as OTMs. The single-phase materials STZN1, STZN3, STZN5 and STZN10 were successfully prepared with the solid-state reaction method. XRD characterization shows that the solubility limit of Ni in the perovskite is below 15 mol% in this case. The findings demonstrate that the substitution of Ti with Ni can considerably improve the oxygen permeability and conductivity of STZN_x in comparison to that of pure STO. It can be observed that an increase in Ni content results in enhanced performance. All samples still are single phase materials even annealed in 2.9 vol% H₂/Ar for 48 h. The surface of STZN10 exhibits uniformly distributed Ni particles after annealing, which can be regarded as active catalytic centers for chemical reactions in a membrane reactor. Three-cycle TG measurements illustrate that all the STZN_x materials exhibit reversible oxygen exchange and, thus, excellent stability in a reducing atmosphere.

Although the oxygen flux of STZN10 is lower than that of most B-site doped STO₃ materials, it demonstrates unique potential for applications as oxygen transport membranes (OTMs) in membrane reactors, particularly in processes involving hydrocarbons at high temperatures. The advantages of STZN10 lie in two key aspects: (1) the incorporation of Ni creates catalytically

active sites on the material surface due to the Ni exsolution phenomenon in reducing atmosphere; and (2) exceptional structural stability under harsh conditions. To enhance its oxygen permeability, several optimization strategies can be implemented, such as establishing a gradient oxygen partial pressure driving force to a certain extent based on specific applications, fabricating submicron-scale ultrathin dense layers (e.g., thickness <50 µm), designing asymmetric membranes with a support layer-functional dense layer composite structure, or the addition of a catalytic layer to the material's surface to reduce surface exchange resistance. These approaches make STZN10 a promising candidate for high temperature membrane reactors involving separation and reaction processes like partial oxidation of methane, combining catalytic activity with high stability.

REFERENCES

- [1] R.W. Baker, Future Directions of Membrane Gas Separation Technology, Industrial & Engineering Chemistry Research 41(6) (2002) 1393-1411.
- [2] R. Kiebach, S. Pirou, L. Martinez Aguilera, A.B. Haugen, A. Kaiser, P.V. Hendriksen, M. Balaguer, J. García-Fayos, J.M. Serra, F. Schulze-Küppers, M. Christie, L. Fischer, W.A. Meulenberg, S. Baumann, A review on dual-phase oxygen transport membranes: from fundamentals to commercial deployment, Journal of Materials Chemistry A 10(5) (2022) 2152-2195.
- [3] F. Sjoberg, M. Singer, The medical use of oxygen: a time for critical reappraisal, Journal of internal medicine 274(6) (2013) 505-28.
- [4] H. Jiang, H. Wang, S. Werth, T. Schiestel, J. Caro, Simultaneous production of hydrogen and synthesis gas by combining water splitting with partial oxidation of methane in a hollow-fiber membrane reactor, Angewandte Chemie 47(48) (2008) 9341-4.
- [5] G. He, Y. Ling, H. Jiang, A. Toghan, Barium Titanate as a Highly Stable Oxygen Permeable Membrane Reactor for Hydrogen Production from Thermal Water Splitting, ACS Sustainable Chemistry & Engineering 9(33) (2021) 11147-11154.
- [6] F.T. Akin, Y.S. Lin, Selective oxidation of ethane to ethylene in a dense tubular membrane reactor, Journal of Membrane Science 209(2) (2002) 457-467.
- [7] H.R. Godini, S. Xiao, M. Kim, N. Holst, S. Jašo, O. Görke, J. Steinbach, G. Wozny, Experimental and model-based analysis of membrane reactor performance for methane oxidative coupling: Effect of radial heat and mass transfer, Journal of Industrial and Engineering Chemistry 20 (2014) 1993-2002.
- [8] A.H. Elbadawi, L. Ge, Z. Li, S. Liu, S. Wang, Z. Zhu, Catalytic partial oxidation of methane to syngas: review of perovskite catalysts and membrane reactors, Catalysis Reviews 63(1) (2021) 1-67.
- [9] W. Bai, J. Feng, C. Luo, P. Zhang, H. Wang, Y. Yang, Y. Zhao, H. Fan, A comprehensive review on oxygen transport membranes: Development history, current status, and future directions, International Journal of Hydrogen Energy 46(73) (2021) 36257-36290.
- [10] F. Schulze-Küppers, S.F.P. ten Donkelaar, S. Baumann, P. Prigorodov, Y.J. Sohn, H.J.M.

- Bouwmeester, W.A. Meulenberg, O. Guillon, Structural and functional properties of $SrTi1-xFexO3-\delta$ ($0 \le x \le 1$) for the use as oxygen transport membrane, Separation and Purification Technology 147 (2015) 414-421.
- [11] V. Metlenko, W. Jung, S.R. Bishop, H.L. Tuller, R.A. De Souza, Oxygen diffusion and surface exchange in the mixed conducting oxides SrTi(1-y)Fe(y)O(3-delta), Physical chemistry chemical physics: PCCP 18(42) (2016) 29495-29505.
- [12] X. Li, H. Zhao, N. Xu, X. Zhou, C. Zhang, N. Chen, Electrical conduction behavior of La, Co co-doped SrTiO3 perovskite as anode material for solid oxide fuel cells, International Journal of Hydrogen Energy 34(15) (2009) 6407-6414.
- [13] Y. Liu, S. Baumann, F. Schulze-Küppers, D.N. Mueller, O. Guillon, Co and Fe co-doping influence on functional properties of SrTiO3 for use as oxygen transport membranes, Journal of the European Ceramic Society 38(15) (2018) 5058-5066.
- [14] L.A. Dunyushkina, V.A. Gorbunov, A.A. Babkina, N.O. Esina, High-temperature electrical transport in Al-doped calcium and strontium titanates, Ionics 9(1) (2003) 67-70.
- [15] Z. Zhao, R.V. Goncalves, S.K. Barman, E.J. Willard, E. Byle, R. Perry, Z. Wu, M.N. Huda, A.J. Moulé, F.E. Osterloh, Electronic structure basis for enhanced overall water splitting photocatalysis with aluminum doped SrTiO3 in natural sunlight, Energy & Environmental Science 12(4) (2019) 1385-1395.
- [16] M.A.K.Y. Shah, Y. Lu, N. Mushtaq, M. Yousaf, S. Rauf, M.I. Asghar, P.D. Lund, B. Zhu, Perovskite Al-SrTiO3 semiconductor electrolyte with superionic conduction in ceramic fuel cells, Sustainable Energy & Fuels 6(16) (2022) 3794-3805.
- [17] G. He, W. Liang, C.L. Tsai, X. Xia, S. Baumann, H. Jiang, W.A. Meulenberg, Chemical Environment-Induced Mixed Conductivity of Titanate as a Highly Stable Oxygen Transport Membrane, iScience 19 (2019) 955-964.
- [18] Y. Liu, V. Motalov, S. Baumann, D. Sergeev, M. Müller, Y.J. Sohn, O. Guillon, Thermochemical stability of Fe- and co-functionalized perovskite-type SrTiO3 oxygen transport membrane materials in syngas conditions, Journal of the European Ceramic Society 39(15) (2019) 4874-4881.
- [19] K. Kendall, M. Kendall, High-temperature solid oxide fuel cells for the 21st century: fundamentals, design and applications, Elsevier2015.

- [20] A. Mizera, E. Drożdż, Studies on structural, redox and electrical properties of Ni-doped strontium titanate materials, Ceramics International 46(15) (2020) 24635-24641.
- [21] M.L. Weber, M. Wilhelm, L. Jin, U. Breuer, R. Dittmann, R. Waser, O. Guillon, C. Lenser, F. Gunkel, Exsolution of Embedded Nanoparticles in Defect Engineered Perovskite Layers, ACS Nano 15(3) (2021) 4546-4560.
- [22] T. Zhu, H.E. Troiani, L.V. Mogni, M. Han, S.A. Barnett, Ni-Substituted Sr(Ti,Fe)O3 SOFC Anodes: Achieving High Performance via Metal Alloy Nanoparticle Exsolution, Joule 2(3) (2018) 478-496.
- [23] D. Papargyriou, D.N. Miller, J.T. Sirr Irvine, Exsolution of Fe–Ni alloy nanoparticles from (La,Sr)(Cr,Fe,Ni)O3 perovskites as potential oxygen transport membrane catalysts for methane reforming, Journal of Materials Chemistry A 7(26) (2019) 15812-15822.
- [24] J. Wang, D. Kalaev, J. Yang, I. Waluyo, A. Hunt, J.T. Sadowski, H.L. Tuller, B. Yildiz, Fast Surface Oxygen Release Kinetics Accelerate Nanoparticle Exsolution in Perovskite Oxides, Journal of the American Chemical Society 145(3) (2023) 1714-1727.
- [25] W. O'Leary, L. Giordano, J. Park, S.S. Nonnenmann, Y. Shao-Horn, J.L.M. Rupp, Influence of Sr-Site Deficiency, Ca/Ba/La Doping on the Exsolution of Ni from SrTiO(3), Journal of the American Chemical Society 145(25) (2023) 13768-13779.
- [26] K.A. Müller, W. Berlinger, R.S. Rubins, Observation of Two Charged States of a Nickel-Oxygen Vacancy Pair in SrTiO3by Paramagnetic Resonance, Physical Review 186(2) (1969) 361-371.
- [27] A.M. Beale, M. Paul, G. Sankar, R.J. Oldman, C.R.A. Catlow, S. French, M. Fowles, Combined experimental and computational modelling studies of the solubility of nickel in strontium titanate, Journal of Materials Chemistry 19(25) (2009) 4391.
- [28] F. Mauvy, J.M. Bassat, E. Boehm, P. Dordor, J.C. Grenier, J.P. Loup, Chemical oxygen diffusion coefficient measurement by conductivity relaxation—correlation between tracer diffusion coefficient and chemical diffusion coefficient, Journal of the European Ceramic Society 24(6) (2004) 1265-1269.
- [29] P.-M. Geffroy, E. Blond, N. Richet, T. Chartier, Understanding and identifying the oxygen transport mechanisms through a mixed-conductor membrane, Chemical Engineering Science 162 (2017).

- [30] R. Cox-Galhotra, S. McIntosh, Unreliability of simultaneously determining kchem and Dchem via conductivity relaxation for surface-modified La0.6Sr0.4Co0.2Fe0.8O3 δ , Solid State Ionics 181 (2010) 1429-1436.
- [31] H.J.M. Bouwmeester, H. Kruidhof, A.J. Burggraaf, Importance of the surface exchange kinetics as rate limiting step in oxygen permeation through mixed-conducting oxides, Solid State Ionics 72 (1994) 185-194.
- [32] J.E. ten Elshof, H.J.M. Bouwmeester, H. Verweij, Oxygen transport through La1-xSrxFeO3-δ. I. Permeation in air/He gradients, Solid State Ionics 81 (1996).
- [33] J. Sunarso, S. Baumann, J.M. Serra, W.A. Meulenberg, S. Liu, Y.S. Lin, J.C. Diniz da Costa, Mixed ionic–electronic conducting (MIEC) ceramic-based membranes for oxygen separation, Journal of Membrane Science 320(1-2) (2008) 13-41.
- [34] A. Arratibel Plazaola, A. Cruellas Labella, Y. Liu, N. Badiola Porras, D.A. Pacheco Tanaka, M.V. Sint Annaland, F. Gallucci, Mixed Ionic-Electronic Conducting Membranes (MIEC) for Their Application in Membrane Reactors: A Review, Processes 7(3) (2019) 128.
- [35] Y. Takeda, T. Hashino, H. Miyamoto, F. Kanamaru, S. Kume, M. Koizumi, Synthesis of SrNiO3 and related compound, Sr2Ni2O5, Journal of Inorganic and Nuclear Chemistry 34(5) (1972) 1599-1601.
- [36] Y. Takeda, F. Kanamura, M. Shimada, M. Koizumi, The crystal structure of BaNiO3, Acta Crystallographica Section B 32(8) (1976) 2464-2466.
- [37] M.C. Biesinger, B.P. Payne, L.W.M. Lau, A. Gerson, R.S.C. Smart, X ray photoelectron spectroscopic chemical state quantification of mixed nickel metal, oxide and hydroxide systems, Surface and Interface Analysis 41(4) (2009) 324-332.
- [38] G. Liu, X. Gao, K. Wang, D. He, J. Li, Uniformly mesoporous NiO/NiFe2O4 biphasic nanorods as efficient oxygen evolving catalyst for water splitting, International Journal of Hydrogen Energy 41(40) (2016) 17976-17986.
- [39] X. Xiao, Y. Xu[‡], Soft chemical synthesis and characterization of lithium nickel oxide electrode materials, Journal of Materials Science 31(24) (1996) 6449-6454.
- [40] J.F. Marco, J.R. Gancedo, M. Gracia, J.L. Gautier, E.I. Ríos, H.M. Palmer, C. Greaves, F.J. Berry, Cation distribution and magnetic structure of the ferrimagnetic spinel NiCo2O4, Journal of Materials Chemistry 11(12) (2001) 3087-3093.

- [41] Y. Wang, Y. Wang, F. Wang, Facile molten salt synthesis of Li2NiTiO4 cathode material for Li-ion batteries, Nanoscale Research Letters 9(1) (2014) 197.
- [42] A.I. Lebedev, I.A. Sluchinskaya, On the nature of change in Ni oxidation state in BaTiO3–SrTiO3system, Ferroelectrics 501(1) (2016) 1-8.
- [43] M.T. Colomer, J.A. Kilner, Effect of sintering time on structural, microstructural and chemical composition of Ni-doped lanthanum gallate perovskites, Journal of Solid State Chemistry 228 (2015) 167-173.
- [44] C. Duan, J. Huang, N. Sullivan, R. O'Hayre, Proton-conducting oxides for energy conversion and storage, Applied Physics Reviews 7(1) (2020).
- [45] M. Yang, F. He, C. Zhou, F. Dong, G. Yang, W. Zhou, Z. Shao, New perovskite membrane with improved sintering and self-reconstructed surface for efficient hydrogen permeation, Journal of Membrane Science 620 (2021) 118980.
- [46] C. Ohly, S. Hoffmann Eifert, X. Guo, J. Schubert, R. Waser, Electrical Conductivity of Epitaxial SrTiO3 Thin Films as a Function of Oxygen Partial Pressure and Temperature, Journal of the American Ceramic Society 89(9) (2006) 2845-2852.
- [47] X. Zhu, W. Yang, Introduction to Mixed Ionic–Electronic Conducting Membranes, in: X. Zhu, W. Yang (Eds.), Mixed Conducting Ceramic Membranes: Fundamentals, Materials and Applications, Springer Berlin Heidelberg, Berlin, Heidelberg, 2017, pp. 1-10.
- [48] Y. Tang, S. Baumann, M. Müller, D. Sebold, A. Nijmeijer, O. Guillon, W.A. Meulenberg, Ni-doping influence on functional properties of SrTi0.65Fe0.35O3-δ for use as oxygen transport membranes, Journal of the European Ceramic Society 44(15) (2024) 116742.

Chapter 4

4.The effects of microstructure and functional properties of Mg and Al doped into SrTi_{0.65}Fe_{0.35}O_{3-δ} (STF35)

Abstract

Mixed ionic-electronic conducting (MIEC) ceramics have significant potential as oxygen transport membranes (OTMs), enabling the separation of high-purity oxygen from air while also combining chemical reactions within membrane reactors. Since most membrane reactors operate in a reducing atmosphere, ensuring the stability of the materials is crucial. Pure strontium titanate (SrTiO₃) demonstrates remarkable thermodynamic stability; however, its electronic and ionic conductivity is limited over a broad spectrum of temperatures and oxygen partial pressures. To improve conductivity, this study utilized a B-site doping approach, involving the partial replacement of Ti with Fe and Al/Mg. The SrTi_{0.65-x}Fe_{0.35}Al_xO_{3-δ} (x=0.01, 0.03, 0.05, 0.10, 0.15) (STFA_x) and SrTi_{0.65-x}Fe_{0.35}Mg_xO_{3-δ} (x=0.01, 0.03, 0.05, 0.10) (STFM_x) powders were synthesized using a solid-state reaction method at 1200 °C, followed by membrane fabrication via sintering at 1400 °C for 5 hours. X-ray diffraction (XRD) analysis confirmed the solubility limits of Al and Mg in the perovskite lattice.

Oxygen permeation measurements showed that Al doping in STF35 led to an oxygen permeability decline compared to pure STF35, attributed to unfavorable substitution effects. The oxygen permeation behavior of STFM_x remained similar with increasing Mg content, except for a notable drop observed in STFM10. Thermogravimetric analysis (TGA) indicated that oxygen concentration changes in STFM_x increased with rising Mg content, higher temperatures, and lower oxygen partial pressures. Scanning electron microscopy (SEM) cross-sectional images revealed MgO segregation during the sintering process of STFM_x, which significantly impacted oxygen permeability. As a result, Al doping was determined to be

unsuitable for this system, while the fabrication process of STFM_x membranes needs optimization to minimize MgO segregation and its associated adverse effects.

4.1 Introduction

Oxygen is a crucial gas with widespread applications across various industrial sectors. Despite its abundance in the atmosphere, separating oxygen into its pure form requires a substantial energy input. The most established technology for oxygen production is cryogenic air distillation in the industry, which can reach a purity exceeding 95% [1, 2]. This technology requires high vacuum conditions and cryogenic temperatures to separate oxygen from air, which is complex and energy-intensive [3, 4].

Ceramic materials that exhibit both ionic and electronic conductivity have shown excellent performance as oxygen transport membranes (OTMs). These membranes have been developed for various energy-related applications, such as air separation for oxyfuel combustion [4] and medical oxygen supply [5]. Additionally, OTMs can be integrated into membrane reactors for the production of key industrial chemicals, such as water splitting [6, 7], selective oxidation of ethane [8], oxidative coupling of methane [9], and partial oxidation of methane [10, 11]. In membrane reactor applications, the gas environment typically contains CO, CO₂, H₂, or CH₄, requiring high chemical stability of the membranes in reducing atmospheres. Strontium titanate (SrTiO₃), a highly stable perovskite material, is primarily known for its dielectric properties. However, its electrical properties can be significantly modified through A/B-site doping strategy. The introduction of oxygen vacancies and electronic defects allows doped SrTiO₃ to conduct oxide ions, making it a mixed ionic-electronic conductor (MIEC) suitable for use as an OTM. Over the past decade, various elements have been doped into the Sr or Ti sites of SrTiO₃, with La [12] and Ca [13] incorporated at the A-site, and Fe [14, 15], Co [16, 17], Ni [18-20], Al [21-23], and Mg [24-26] at the B-site. However, while doping enhances oxygen transport properties, it can also compromise structural stability. For instance, cobalt-doped SrTiO₃ significantly improves oxygen permeability but suffers from stability issues [27]. Dunyushkina et al. [21] reported that incorporating 10 mol% Al into the SrTiO structure enhances its ionic conductivity. However, when the Al content exceeds 20 mol% SrTi_{l-x}Al_xO_{3-δ} (x > 0.2), the formation of secondary phases in the SrTiO₃ perovskite phase leads to a decline in conductivity, which limits its overall performance. Shah et al. [23] further explored the effects of Al doping into the SrTiO₃ structure and found that introducing 20 mol% Al into SrTiO₃ (SrTi_{0.8}Al_{0.2}O_{3.8}) significantly improves the performance of solid oxide fuel cells (SOFCs). This composition has been identified as a promising electrolyte candidate, particularly for low-temperature solid oxide fuel cells (LT-SOFCs) due to its enhanced ionic conductivity and electrochemical stability. On the other hand, Kharton et al. [24] investigated the impact of Mg doping on SrTiO₃. Their study revealed that substituting 10 mol% of the Bsite cations with Mg in Sr_{0.97}Ti_{0.70}Fe_{0.20}Mg_{0.10}O_{3-δ} increases ionic conductivity while simultaneously reducing surface exchange rates. Compared to Sr_{0.97}Ti_{0.60}Fe_{0.40}O_{3-δ}, which exhibits a similar oxygen flux, the Mg-doped material demonstrates higher ionic transport properties, making it a potential candidate for applications requiring efficient ion conduction. Additionally, Tkach et al. [25] found that Mg doping in the B-site of the SrTiO₃ structure shifts the system away from ferroelectric instability, leading to a reduction in dielectric permittivity and dielectric losses. Similarly, He et al. [26] reported that Mg doping enhances the oxygen permeability of SrTiO₃. In particular, the highly stable compound SrMg_{0.15}Zr_{0.05}Ti_{0.8}O_{3-δ} (SMZ-Ti) exhibits excellent oxygen permeation properties under operational conditions. This material has demonstrated the ability to facilitate water splitting on one side of the membrane while simultaneously utilizing the permeated oxygen for methane reforming on the other. Such a dual-functionality mechanism makes SMZ-Ti a highly promising material for energy conversion and storage applications. Schulze-Küppers et al. [14] investigated the functional properties of SrTi_{1-x}Fe_xO_{3-\delta} (STF) and reported that an Fe content of 25–35 mol% offers a promising balance between stability and oxygen permeability. While Al- and Mg-doped STO₃ have been studied by many researchers, the impact of Al/Mg-doping on the functional properties of STF35, particularly for oxygen transport membrane (OTM) applications, has not yet been systematically explored. In this study, we synthesized the compositions $SrTi_{0.65-x}Fe_{0.35}Al_xO_{3-\delta}$ (x=0.01, 0.03, 0.05, 0.10, 0.15) (STFA_x) and $SrTi_{0.65-x}Fe_{0.35}Mg_xO_{3-\delta}$ (x=0.01, 0.03, 0.05, 0.10) (STFM_x). The structure of the various materials has been characterized, and their oxygen permeability has been determined.

4.2 Experimental

4.2.1 Sample preparation

SrTi_{0.65-x}Fe_{0.35}Al_xO_{3-\delta} (x=0.01, 0.03, 0.05, 0.10, 0.15) (STFA_x) and SrTi_{0.65-x}Fe_{0.35}Mg_xO_{3-\delta} (x=0.01, 0.03, 0.05, 0.10) (STFM_x) ceramic powders were synthesized via a solid-state reaction route. The commercial precursors SrCO₃ (Merck, 99%), TiO₂ (Merck, 99%), Fe₂O₃ (Merck, 99%), Al₂O₃ (Merck, 99%), standard MgO (Merck, 99%) and nano-sized MgO (Thermo Fisher, 99%) were used as-received without purification. The Mg-doped STF35 synthesized using standard MgO is referred to as STFM_x_standard to distinguish it from STFM_x synthesized with nano-sized MgO. The stoichiometric mixtures were homogenized by ball milling in ethanol for 48 h using 3 mm Y-stabilized ZrO₂ balls, maintaining a mass ratio of powder: ethanol: balls = 1:2:3. The slurry was subsequently dried at 70°C, sieved through a 250 µm mesh, and calcined at 1200°C for 5 h in air. The calcined powders were subjected to secondary ball milling or 24 h under the same conditions and followed by final drying. Bulk membranes (\varnothing 20 mm) were fabricated by uniaxial pressing at 70 MPa for 90 s using a PW10 press (Paul Otto Weber GmbH, Remshalden). The pressed discs were sintered in air at 1400°C for 5 h with controlled heating and cooling rates of 5 °C/min to get dense membranes.

4.2.2 Structural characterization

The crystalline phases and structural characteristics of the synthesized materials were analyzed using X-ray diffraction (XRD, Bruker D4 ENDEAVOR) with Cu Kα radiation at room temperature. Scans were performed over a 2θ range of 10–80° with a step size of 0.02° and a dwell time of 0.75 s per step. Phase identification and refinement were conducted using Profex software. Microstructural features and elemental distribution were performed via scanning electron microscopy (SEM, Hitachi TM3000 tabletop) equipped with energy-dispersive X-ray spectroscopy (EDS). The gas-tightness of sintered membranes was verified using a helium leak detector (Qualy test HTL 260, Pfeiffer Vacuum GmbH, Asslar, Germany). Thermogravimetric analysis (TGA) coupled with mass spectrometry (MS) was performed on a STA449 F1 Jupiter system integrated with a QMS 403C Aëolos mass spectrometer (Netzsch). TG measurements

were conducted in air and Ar atmospheres from 600 °C to 900 °C, with a heating/cooling rate of 10°C/min and a gas flow rate of 50 mL/min.

4.2.3 Oxygen permeation measurement

All the materials were subjected to oxygen permeation measurements, which were conducted on a 4-end mode set up in air (feed gas)/Ar (sweep side) atmosphere from 700 °C to 1000 °C. The dense membranes were prepared with a diameter of approximately 14.6 mm and a thickness of 1 mm. The gas flow rates were controlled using mass flow controllers (MFCs, Bronkhorst, Germany), with a standard flow rate of 250 mL·min⁻¹ for the feed side (air) and 50 mL·min⁻¹ for the sweep side (Ar). All samples were sequentially polished with sandpaper to remove surface contaminants and achieve a smooth surface before measurements. Subsequently, the samples were sealed to a quartz glass reactor using gold rings with an inner diameter of 13 mm. During the measurements, the O₂ and N₂ concentration was recorded using a mass spectrometer (Omni Star, Pfeiffer Vacuum US). By measuring the N₂ concentration in the Ar sweep gas, air leakage through the membrane or the sealing process can be determined. The oxygen flux j(O₂) can be described by the Wagner equation [28, 29] (equation (4.1)).

$$j(O_2) = \frac{R \cdot T}{16F^2 \cdot L} \cdot \int_{\ln p''_{O_2}}^{\ln p'_{O_2}} \sigma_{amb} \cdot d \ln p_{O_2}$$
 (4.1)

A more simplified Wagner equation is derived in the form of

$$j(O_2) = \frac{R}{16F^2 \cdot L} \cdot T \cdot \sigma_{amb} \cdot \ln \frac{p'_{O_2}}{p''_{O_2}}$$

$$\tag{4.2}$$

where R represents the gas constant (8.314 J·K⁻¹·mol⁻¹), T is the temperature (K), F is the Faraday constant, L is the thickness of the membrane (cm). The parameters p'_{o_2} and p''_{o_2} refer to the oxygen partial pressure on the oxygen-rich and oxygen-lean sides of the membrane, respectively. σ_{amb} is the ambipolar conductivity, which can be defined by equation (4.3):

$$\sigma_{amb} = \frac{\sigma_i \cdot \sigma_e}{\sigma_i + \sigma_e} \tag{4.3}$$

Where σ_i and σ_e are the ionic and electronic conductivity, respectively.

Oxygen permeance, as discussed in Chapter 1, is a key parameter for evaluating the performance of oxygen transport membranes. It is determined by normalizing the oxygen flux $j(O_2)$ with respect to the oxygen partial pressure gradient $(\ln \frac{p'o_2}{p''_{O_2}})$, which serves as the driving

force for oxygen transport. The oxygen permeance can be expressed as:

$$Permeance = \frac{j(O_2)}{\ln \frac{p'_{O_2}}{p''_{O_2}}} = \frac{R}{16F^2 \cdot L} \cdot T \cdot \sigma_{amb}$$
(4.4)

The activation energy of the oxygen permeance can be obtained by the Arrhenius approach:

$$ln(permeance) = -\frac{E_a}{RT} + A$$
(4.5)

Where E_a is the activation energy and A is the pre-exponential factor.

4.3 Results and discussion

4.3.1 Microstructure

Figure 4.1 presents the XRD patterns of STFA_x and STFM_x materials. The STFA_x samples maintain a single-phase structure throughout the studied composition range, even at an Al content of up to 15 mol%. In contrast, the solubility limit of Mg in STFM_x is below 10 mol%, as impure phases such as Sr₄Ti₃O₁₀ are detected in the XRD patterns (Figure 4.1(a)). The analysis confirms that the space group of all STFA_x and STFM_x materials crystallize is Pm3m, adopting a cubic perovskite structure. The incorporation of Al into STF35 results in a shift of all diffraction peaks toward higher angles, as illustrated by the zoomed-in patterns in the 31°~34° range (Figure 4.1(b)), indicating a reduction in the lattice constant. In perovskite structures, Al is typically present as Al³⁺. Meanwhile, Ti is confirmed to exist in both Ti³⁺ (0.67 Å) and Ti⁴⁺ (0.605 Å) oxidation states [22]. The substitution of the host Ti³⁺ /Ti⁴⁺ with the dopant Al³⁺ (0.535 Å) is expected to decrease the lattice constant due to the smaller ionic radius of Al³⁺. Similar trends have been observed in Fe-doped STO₃ and cobalt-doped STO₃ materials, where increasing Fe/Co content leads to a reduction in the lattice parameter. This

effect is attributed to the smaller ionic radii of Fe⁴⁺ (0.585 Å) and Co³⁺ (0.545 Å) compared to Ti⁴⁺ (0.605 Å) [14, 17].

For STFM_x materials, the XRD peaks shift to higher degree and then to lower degree as Mg content increases, indicating a decrease followed by an increase in the lattice constant. This behavior suggests that the lattice first contracts and then expands with rising Mg doping levels. To explain this, we need consider the substitution way of Mg²⁺ for Ti³⁺ /Ti⁴⁺. At low Mg doping concentrations, Mg²⁺ (0.72 Å) may prefer substitutes Ti³⁺ (0.67 Å), and charge compensation leads to the oxidation of some Ti³⁺ to Ti⁴⁺. Since the ionic radius of Ti³⁺ is larger than that of Ti⁴⁺ (0.605 Å), the reduction in Ti³⁺ content decreases the average ionic radius, resulting in lattice shrinkage and a shift of the XRD peaks toward higher angles. At higher Mg doping concentrations, more Mg²⁺ starts to replace Ti⁴⁺. In this case, the ionic radius of Mg²⁺ is larger than that of Ti⁴⁺, causing lattice expansion and a shift of the peaks toward lower angles. The lattice parameters of STFA_x and STFM_x perovskites have been determined from XRD patterns as shown in Table 4.1. The density is confirmed by Helium leakage experiments (< 10^{-7} mbar·L·s⁻¹).

Table 4.1 The lattice parameters of STFA_x and STFM_x perovskite structure

Name	Lattice parameter	Name	Lattice parameter
	a=b=c, Å		a=b=c, Å
STFA1	3.900	STF35	3.903
STFA3	3.900	STFM1	3.900
STFA5	3.900	STFM3	3.901
STFA10	3.899	STFM5	3.902
STFA15	3.897	STFM10	3.903

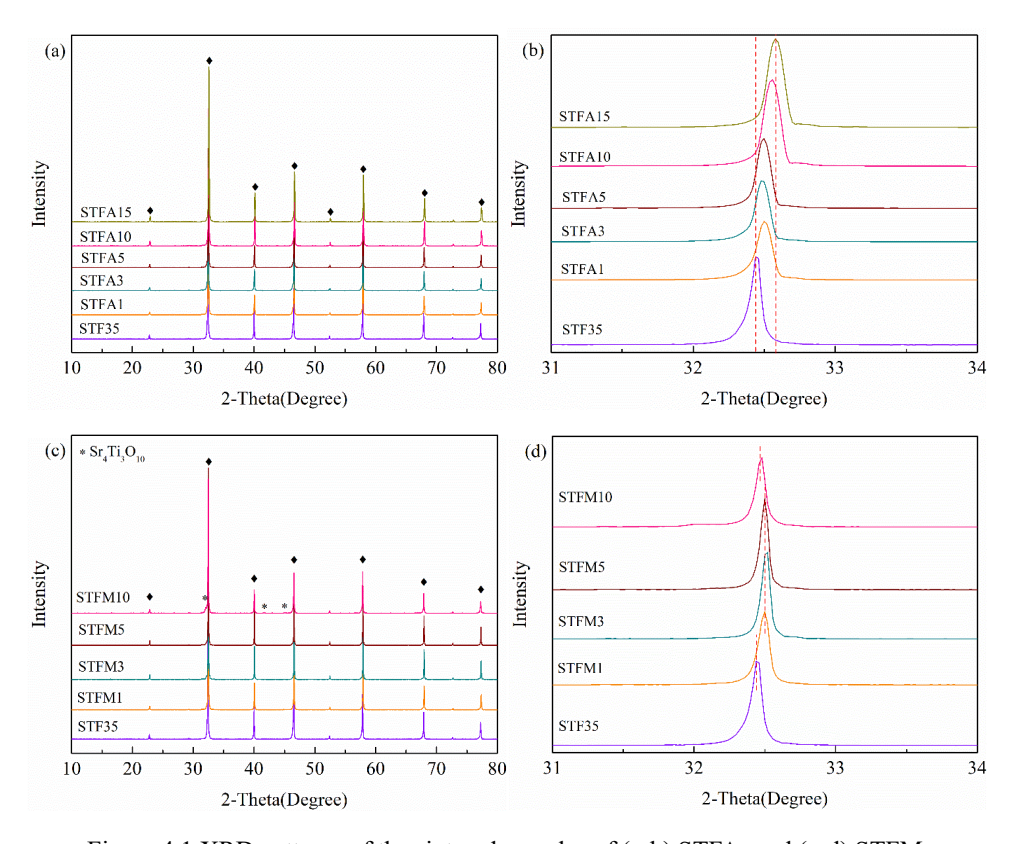


Figure 4.1 XRD patterns of the sintered samples of (a-b) STFA_x and (c-d) STFM_x.

4.3.2 Oxygen permeation

In perovskite structures, Al³⁺ can substitute titanium through two distinct mechanisms based on ionic matching criteria. The first substitution mechanism involves Al³⁺ (0.535 Å) replacing Ti⁴⁺ (0.605 Å), facilitated by their comparable ionic radii. This substitution creates oxygen vacancies due to the charge imbalance between Al³⁺ and Ti⁴⁺, which theoretically enhances oxygen permeability. However, the stronger Al-O bond strength compared to Ti-O simultaneously suppresses lattice oxygen loss, creating a counteractive effect on oxygen transport. Another substitution mechanism occurs through valence matching, where Al³⁺ replaces Ti³⁺ (0.67 Å). Zhao et al. and Shah et al. have reported that Al doping in STO₃ structures leads to the dispersion of Ti³⁺ with the help of XPS measurements [22, 23]. Additionally, Shah et al. [23] indicated that approximately 27.2 mol% of the Ti in the perovskite

exists in the Ti³⁺ oxidation state. Their findings confirm that Al³⁺ ions successfully substitute Ti³⁺ ions within the STO₃ lattice [30]. In this case, no additional oxygen vacancies are generated as both ions share the same +3 valence state. Moreover, the enhanced Al-O bond strength again restricts lattice oxygen mobility, which can significantly influence the oxygen permeability. Therefore, the impact of Al doping on the oxygen permeability in STO materials results from synergistic interaction between two distinct substitution mechanisms.

As shown in Figure 4.2, all STFA_x samples exhibit lower oxygen permeance compared to STF35. The permeance generally decreases with increasing Al content, except for STFA15. This overall trend can be attributed to two factors: (1) the substitution of Al³⁺ into Ti³⁺ sites and (2) the enhanced lattice stability induced by stronger Al-O bond. However, the slight increase observed in STFA15 compared to STFA10 may originate from Al³⁺ partially occupying Ti⁴⁺ sites, which modifies the oxygen vacancy concentration and charge compensation mechanisms.

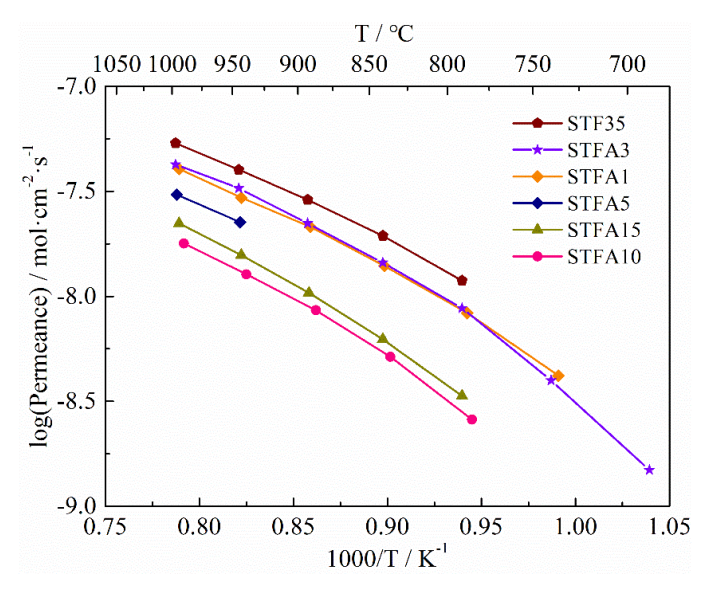


Figure 4.2 Oxygen permeance of STFA_x

Figure 4.3 presents the oxygen permeance of STFM_x_standard synthesized with standard MgO powder. The permeance of the STFM_x_standard membranes decreases with increasing Mg content. There are distinct black regions on the STFM3_standard membrane surface, which are visibly noticeable and confirmed by SEM images. The regions are likely caused by excessively

large MgO particles that fail to fully integrate into the structure, thereby affecting permeance. To verify this, nano-sized MgO powder was used to synthesize $STFM_x$ for further investigation.

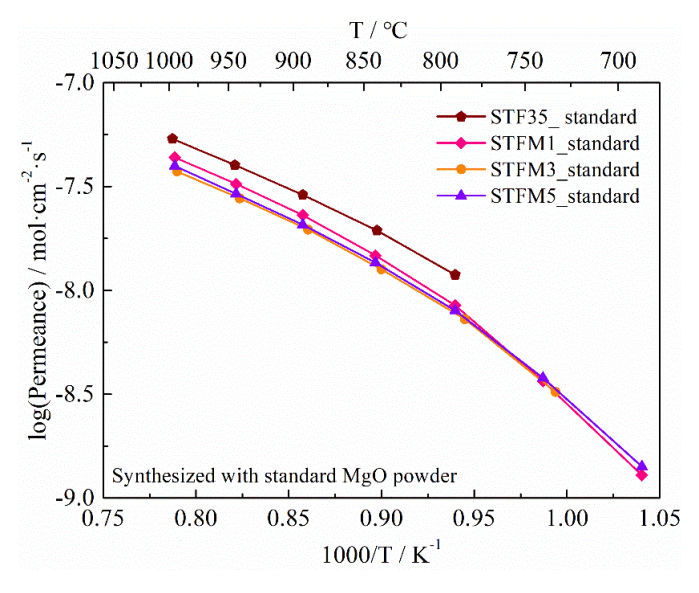


Figure 4.3 Oxygen permeance of STFM_x synthesized with standard MgO powder

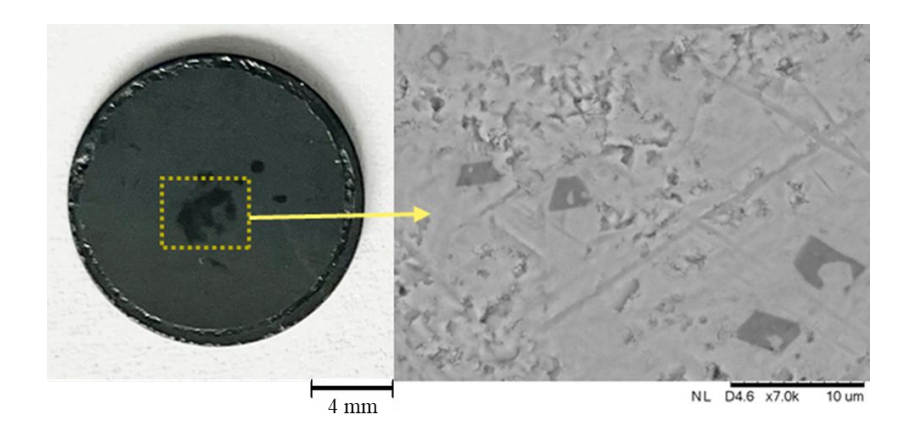


Figure 4.4 SEM image of STFM3 surface synthesized with standard MgO powder

The synthesized STFM_x samples incorporating nano-MgO exhibit no visible dark regions on the surface (Figure 4.5(a)). The oxygen permeance of STFM_x is higher than that of the STFM_x_standard, but the results still remain similar across the STF35 and the STFM_x samples except for STFM10. STFM10 shows a significant decline in permeance (Figure 4.5(b)), which

can be attributed to the formation of impure phases that disrupt crystalline continuity in the structure. Generally, Mg^{2+} (0.72 Å) doping in the STO₃ structure has positive effects on oxygen permeability, regardless of whether it occupies Ti^{3+} (0.67 Å) or Ti^{4+} (0.605 Å) lattice sites. The cationic replacement generates oxygen vacancies through a charge compensation mechanism ($Mg^{2+} \rightarrow Ti^{3+}$ / Ti^{4+}). Additionally, the lower bond dissociation energy of Mg-O compared to Ti-O enhances lattice oxygen mobility, theoretically improving oxygen transport kinetics. However, the observed similar volume in oxygen permeance of STFM_x materials compared to STF35 is not consistent with the mechanisms discussed above (Figure 4.5(b)). To investigate this further, two aspects require attention: (1) oxygen vacancy concentration changes and (2) structural integrity.

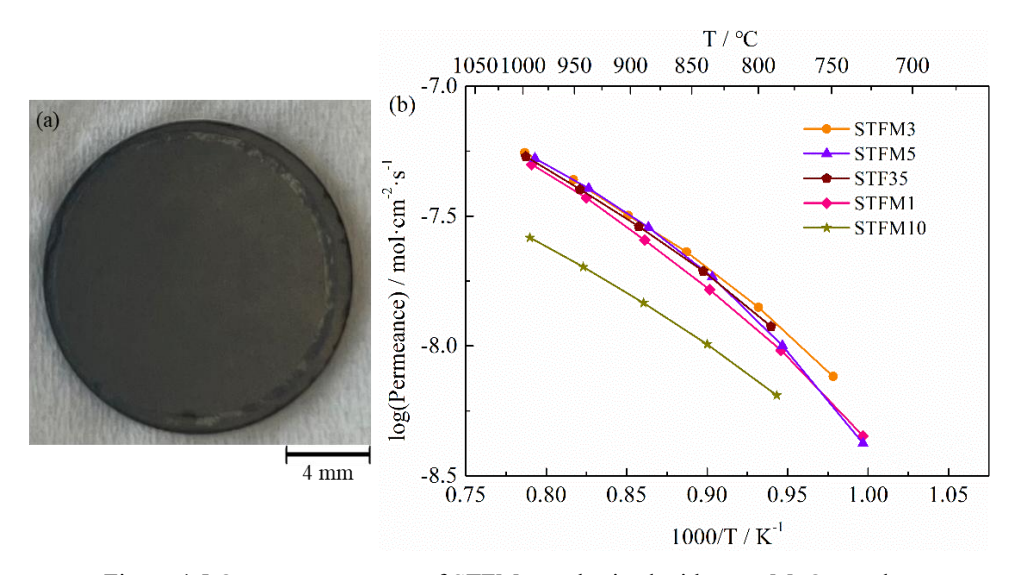


Figure 4.5 Oxygen permeance of STFM_x synthesized with nano MgO powder

The ambipolar conductivity of STF35 and STFM_x materials follows the same trend as permeance as shown in Figure 4.6. Table 4.2 lists the oxygen flux, permeance, ambipolar conductivity and the activation energy of permeance for STF35 and STFM_x. Among them, STFM3 demonstrates the highest oxygen flux, permeance and ambipolar conductivity at approximately 900 °C compared to STF35 and other STFM_x compositions. The activation energy values for all samples range from 76 to 89 kJ/mol, suggesting that the oxygen

permeation process is primarily limited by bulk diffusion.

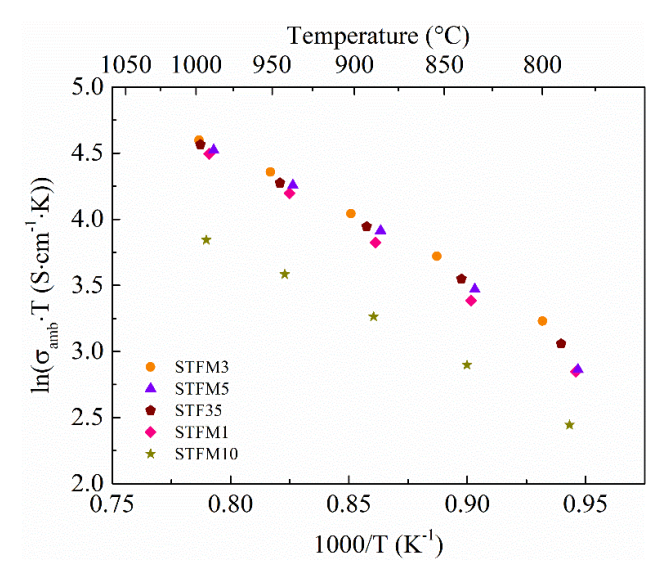


Figure 4.6 Arrhenius plot of ambipolar conductivity of $STFM_x$ synthesized with nano MgO powder

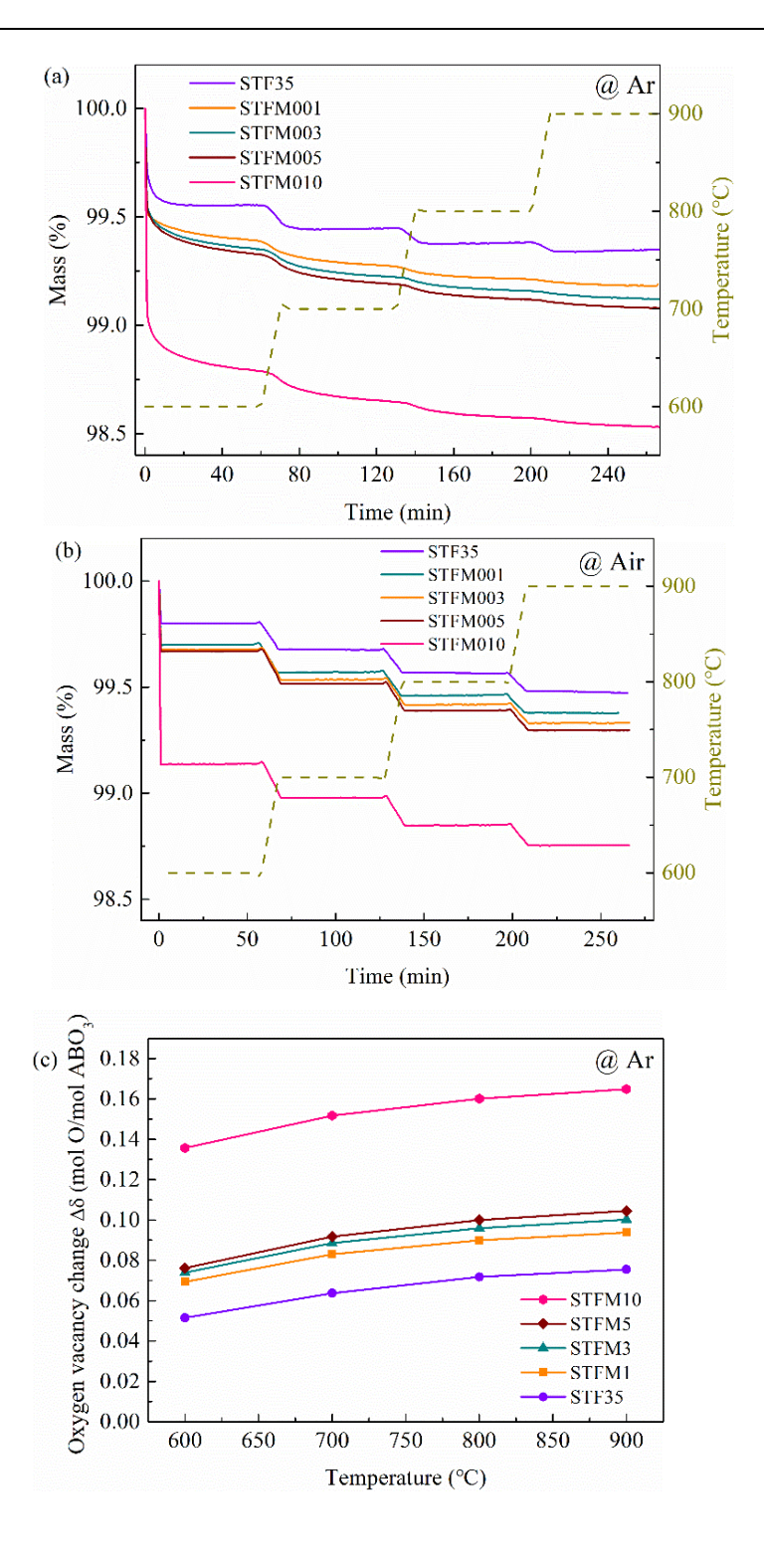
Table 4.2 Oxygen flux, permeance, ambipolar conductivity and the activation energy of oxygen permeance for STF35 and STF $M_{\rm x}$

Name	T ℃	Oxygen flux ml·cm ⁻² ·min ⁻¹	Log (Permeance) mol·cm ⁻² ·s ⁻¹	σ_{amb} _Air (S/cm)	E _{a_} Permeance (800-1000 °C) kJ/mol
STF35	893	0.15	-7.54	4.43×10 ⁻²	82
STFM1	888	0.14	-7.59	3.94×10 ⁻²	89
STFM3	902	0.17	-7.49	4.85×10 ⁻²	78
STFM5	885	0.15	-7.54	4.32×10 ⁻²	89
STFM10	889	0.088	-7.83	2.25×10 ⁻²	76

4.3.3 Oxygen vacancy concentration change of STFM_x

Figure 4.7 illustrates TG measurements of $STFM_x$ in Ar and air, and corresponding oxygen vacancy changes in Ar and air. In the $STFM_x$ series materials, the oxygen vacancy concentration changes increase with rising Mg content, higher temperatures, and decreasing oxygen partial pressure.

This trend is primarily driven by the substitution Ti³⁺/Ti⁴⁺ with Mg²⁺, which induces oxygen vacancy formation through charge compensation. Additionally, high temperatures enhance oxygen ion mobility, further promoting vacancy formation. A lower oxygen partial pressure also favors oxygen vacancy generation as the material tends to release lattice oxygen to maintain equilibrium. Generally, a higher oxygen vacancy concentration change is expected to enhance oxygen permeability, as vacancies facilitate oxygen ion transport. For STFM10, although STFM10 shows the highest mass loss and oxygen vacancy concentration change under both Ar and air conditions, the impure phases in the perovskite structure results in a loss of structural integrity and thus a decrease in permeability. However, in other STFM_x materials, the observed trend does not match the results from the oxygen permeance measurements, suggesting that additional factors, such as microstructure, may influence the permeability behavior.



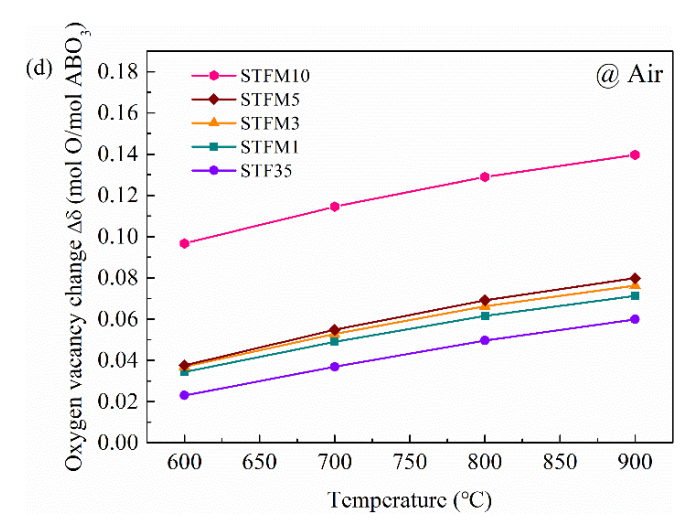


Figure 4.7 TG measurements of $STFM_x$ in Ar and air, and corresponding oxygen vacancy changes in Ar and air

4.3.4 MgO segregation of STFM

Figure 4.8 presents SEM images of the cross-section of STFM $_{\rm X}$ materials. The cross-section of STFM10 is significantly rougher than that of STFM3 and STFM5 due to the influence of impure phase. During sintering, Mg-enriched phases were observed on most of STFM $_{\rm X}$ materials except STFM1 (marked in red circle), which negatively impacted the oxygen permeability of the materials. This phenomenon has been previously reported in the $La_{\rm X}Sr_{1-{\rm X}}Ga_{\rm Y}Mg_{1-{\rm Y}}O_{3-{\rm Z}}$ (LSGM) system literature [31-33]. In this study, it was found that MgO segregation during the sintering process led to a decrease in ionic conductivity, suggesting that the introduction of Mg may adversely affect the microstructure and phase composition, ultimately weakening ionic transport properties. Reis et al. observed that the microstructural features appear to be inherent to the compound, regardless of the sintering method used [33] . Therefore, understanding and controlling MgO segregation is essential for optimizing the performance of such materials.

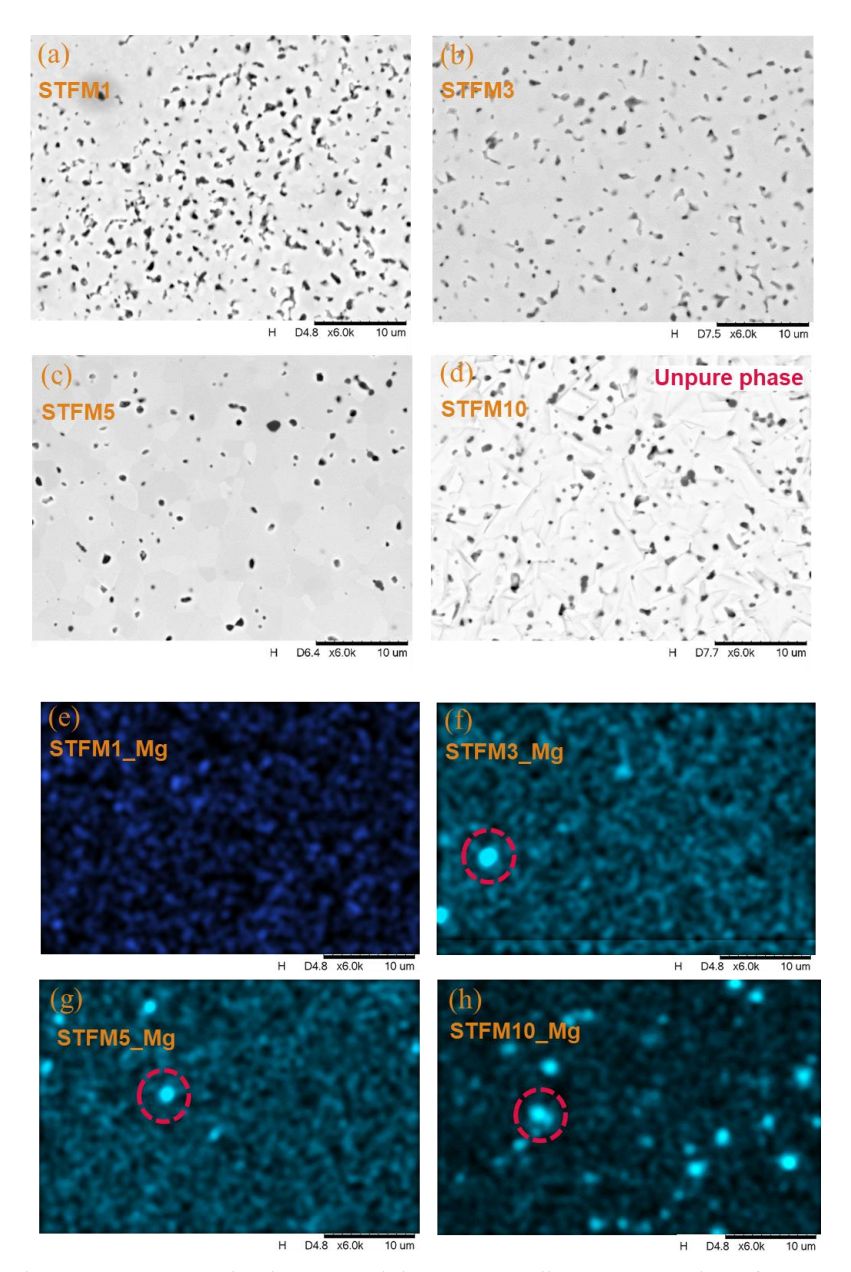


Figure 4.8 Cross-section images and the corresponding EDS mapping of STFM_x

4.4 Conclusions

This study systematically investigates the microstructures and oxygen permeability of $SrTi_{0.65-x}Fe_{0.35}Al_xO_{3-\delta}$ (x=0.01, 0.03, 0.05, 0.10, 0.15) (STFA_x) and $SrTi_{0.65-x}Fe_{0.35}Mg_xO_{3-\delta}$ (x=0.01, 0.03, 0.05, 0.10) (STFM_x) series materials for use as OTMs. XRD characterization shows that the STFAx samples maintain a single-phase structure throughout the studied composition range, even at an Al content of up to 15 mol%. In contrast, the solubility limit of Mg in $STFM_x$ is below 10 mol%. The oxygen permeation measurements demonstrate that all STFA_x samples exhibit lower oxygen permeance compared to STF35 attributed to unfavorable substitution effects. The permeance generally decreases with increasing Al content, except for STFA15. The slight increase observed in STFA15 compared to STFA10 may originate from Al³⁺ partially occupying Ti⁴⁺ sites, which modifies the oxygen vacancy concentration and charge compensation mechanisms. The oxygen permeance of STFM_x standard synthesized with standard MgO powder and STFMx synthesized with nano-sized MgO powder are compared. The permeance of the STFM_x standard membranes decreases with increasing Mg content. The distinct black regions on the STFM3 standard membrane surface are likely caused by excessively large MgO particles that fail to fully integrate into the structure, thereby affecting permeance. The oxygen permeance of STFM_x is higher than that of STFM_x standard, but the results still remain similar across the STF35 and the STFMx samples except for STFM10. Thermogravimetric analysis (TGA) indicated that oxygen concentration changes in STFM_x increased with rising Mg content, higher temperatures, and lower oxygen partial pressures. However, the observed trend does not match the results from the oxygen permeance measurements. Mg-enriched phases were observed on most of STFM_x materials, which negatively impacted the oxygen permeability of the materials. Therefore, understanding and controlling MgO segregation is essential for optimizing the performance of such materials. As a result, Al doping was determined to be unsuitable for this system. Although the oxygen flux of STFM_x is not ideal, several optimization strategies can be implemented to minimize MgO segregation and then improve permeability, such as utilizing controlled atmosphere sintering (e.g., inert or reducing environments) to stabilize the lattice and inhibit secondary phase formation, employing rapid sintering methods such as spark plasma sintering (SPS) or fieldassisted sintering (FAST) to shorten high-temperature exposure, minimizing time-dependent Mg diffusion, using sol-gel or chemical precursor synthesis to achieve atomic-level homogeneity in the initial powder, reducing localized Mg-rich regions and so on. These approaches can still make $STFM_x$ a promising candidate for use as OTMs in membrane reactors.

REFERENCES

- [1] R.J. Allam, Improved oxygen production technologies, Energy Procedia 1(1) (2009) 461-470.
- [2] F. Wu, M. Argyle, P. Dellenback, M. Fan, Progress in O2 separation for oxy-fuel combustion—A promising way for cost-effective CO2 capture: A review, Progress in Energy and Combustion Science 67 (2018).
- [3] R.W. Baker, Future Directions of Membrane Gas Separation Technology, Industrial & Engineering Chemistry Research 41(6) (2002) 1393-1411.
- [4] R. Kiebach, S. Pirou, L. Martinez Aguilera, A.B. Haugen, A. Kaiser, P.V. Hendriksen, M. Balaguer, J. García-Fayos, J.M. Serra, F. Schulze-Küppers, M. Christie, L. Fischer, W.A. Meulenberg, S. Baumann, A review on dual-phase oxygen transport membranes: from fundamentals to commercial deployment, Journal of Materials Chemistry A 10(5) (2022) 2152-2195.
- [5] F. Sjoberg, M. Singer, The medical use of oxygen: a time for critical reappraisal, Journal of internal medicine 274(6) (2013) 505-28.
- [6] H. Jiang, H. Wang, S. Werth, T. Schiestel, J. Caro, Simultaneous production of hydrogen and synthesis gas by combining water splitting with partial oxidation of methane in a hollow-fiber membrane reactor, Angewandte Chemie 47(48) (2008) 9341-4.
- [7] G. He, Y. Ling, H. Jiang, A. Toghan, Barium Titanate as a Highly Stable Oxygen Permeable Membrane Reactor for Hydrogen Production from Thermal Water Splitting, ACS Sustainable Chemistry & Engineering 9(33) (2021) 11147-11154.
- [8] F.T. Akin, Y.S. Lin, Selective oxidation of ethane to ethylene in a dense tubular membrane reactor, Journal of Membrane Science 209(2) (2002) 457-467.
- [9] H.R. Godini, S. Xiao, M. Kim, N. Holst, S. Jašo, O. Görke, J. Steinbach, G. Wozny, Experimental and model-based analysis of membrane reactor performance for methane oxidative coupling: Effect of radial heat and mass transfer, Journal of Industrial and Engineering Chemistry 20 (2014) 1993-2002.
- [10] A.H. Elbadawi, L. Ge, Z. Li, S. Liu, S. Wang, Z. Zhu, Catalytic partial oxidation of methane to syngas: review of perovskite catalysts and membrane reactors, Catalysis Reviews

- 63(1) (2021) 1-67.
- [11] W. Bai, J. Feng, C. Luo, P. Zhang, H. Wang, Y. Yang, Y. Zhao, H. Fan, A comprehensive review on oxygen transport membranes: Development history, current status, and future directions, International Journal of Hydrogen Energy 46(73) (2021) 36257-36290.
- [12] X. Li, H. Zhao, X. Zhou, N. Xu, Z. Xie, N. Chen, Electrical conductivity and structural stability of La-doped SrTiO3 with A-site deficiency as anode materials for solid oxide fuel cells, International Journal of Hydrogen Energy 35(15) (2010) 7913-7918.
- [13] P. Fedeli, V. Nigroni, E. Malgrati, A. Cavaliere, A. Cammi, F. Drago, Ca substitution in Ca1 xSrxTi0.8Fe0.2O3 δ perovskites for oxygen transport membranes: A promising strategy to improve CO2 tolerance, Journal of the American Ceramic Society 107(8) (2024) 5668-5681.
- [14] F. Schulze-Küppers, S.F.P. ten Donkelaar, S. Baumann, P. Prigorodov, Y.J. Sohn, H.J.M. Bouwmeester, W.A. Meulenberg, O. Guillon, Structural and functional properties of $SrTi1-xFexO3-\delta$ ($0 \le x \le 1$) for the use as oxygen transport membrane, Separation and Purification Technology 147 (2015) 414-421.
- [15] V. Metlenko, W. Jung, S.R. Bishop, H.L. Tuller, R.A. De Souza, Oxygen diffusion and surface exchange in the mixed conducting oxides SrTi(1-y)Fe(y)O(3-delta), Physical chemistry chemical physics: PCCP 18(42) (2016) 29495-29505.
- [16] X. Li, H. Zhao, N. Xu, X. Zhou, C. Zhang, N. Chen, Electrical conduction behavior of La, Co co-doped SrTiO3 perovskite as anode material for solid oxide fuel cells, International Journal of Hydrogen Energy 34(15) (2009) 6407-6414.
- [17] Y. Liu, S. Baumann, F. Schulze-Küppers, D.N. Mueller, O. Guillon, Co and Fe co-doping influence on functional properties of SrTiO3 for use as oxygen transport membranes, Journal of the European Ceramic Society 38(15) (2018) 5058-5066.
- [18] K.A. Müller, W. Berlinger, R.S. Rubins, Observation of Two Charged States of a Nickel-Oxygen Vacancy Pair in SrTiO3by Paramagnetic Resonance, Physical Review 186(2) (1969) 361-371.
- [19] A.M. Beale, M. Paul, G. Sankar, R.J. Oldman, C.R.A. Catlow, S. French, M. Fowles, Combined experimental and computational modelling studies of the solubility of nickel in strontium titanate, Journal of Materials Chemistry 19(25) (2009) 4391.

- [20] A. Mizera, E. Drożdż, Studies on structural, redox and electrical properties of Ni-doped strontium titanate materials, Ceramics International 46(15) (2020) 24635-24641.
- [21] L.A. Dunyushkina, V.A. Gorbunov, A.A. Babkina, N.O. Esina, High-temperature electrical transport in Al-doped calcium and strontium titanates, Ionics 9(1) (2003) 67-70.
- [22] Z. Zhao, R.V. Goncalves, S.K. Barman, E.J. Willard, E. Byle, R. Perry, Z. Wu, M.N. Huda, A.J. Moulé, F.E. Osterloh, Electronic structure basis for enhanced overall water splitting photocatalysis with aluminum doped SrTiO3 in natural sunlight, Energy & Environmental Science 12(4) (2019) 1385-1395.
- [23] M.A.K.Y. Shah, Y. Lu, N. Mushtaq, M. Yousaf, S. Rauf, M.I. Asghar, P.D. Lund, B. Zhu, Perovskite Al-SrTiO3 semiconductor electrolyte with superionic conduction in ceramic fuel cells, Sustainable Energy & Fuels 6(16) (2022) 3794-3805.
- [24] V.V. Kharton, A.P. Viskup, A.V. Kovalevsky, F.M. Figueiredo, J.R. Jurado, A.A. Yaremchenko, E.N. Naumovich, J.R. Frade, Surface-limited ionic transport in perovskites Sr0.97(Ti,Fe,Mg)O3 δ, Journal of Materials Chemistry 10(5) (2000) 1161-1169.
- [25] A. Tkach, P.M. Vilarinho, A. Kholkin, Effect of Mg doping on the structural and dielectric properties of strontium titanate ceramics, Applied Physics A 79(8) (2004) 2013-2020.
- [26] G. He, W. Liang, C.L. Tsai, X. Xia, S. Baumann, H. Jiang, W.A. Meulenberg, Chemical Environment-Induced Mixed Conductivity of Titanate as a Highly Stable Oxygen Transport Membrane, iScience 19 (2019) 955-964.
- [27] Y. Liu, V. Motalov, S. Baumann, D. Sergeev, M. Müller, Y.J. Sohn, O. Guillon, Thermochemical stability of Fe- and co-functionalized perovskite-type SrTiO3 oxygen transport membrane materials in syngas conditions, Journal of the European Ceramic Society 39(15) (2019) 4874-4881.
- [28] J. Sunarso, S. Baumann, J.M. Serra, W.A. Meulenberg, S. Liu, Y.S. Lin, J.C. Diniz da Costa, Mixed ionic–electronic conducting (MIEC) ceramic-based membranes for oxygen separation, Journal of Membrane Science 320(1-2) (2008) 13-41.
- [29] A. Arratibel Plazaola, A. Cruellas Labella, Y. Liu, N. Badiola Porras, D.A. Pacheco Tanaka, M.V. Sint Annaland, F. Gallucci, Mixed Ionic-Electronic Conducting Membranes (MIEC) for Their Application in Membrane Reactors: A Review, Processes 7(3) (2019) 128.
- [30] T. Takata, K. Domen, Defect Engineering of Photocatalysts by Doping of Aliovalent Metal

Cations for Efficient Water Splitting, The Journal of Physical Chemistry C 113(45) (2009) 19386-19388.

- [31] R. Polini, A. Pamio, E. Traversa, Effect of synthetic route on sintering behaviour, phase purity and conductivity of Sr- and Mg-doped LaGaO3 perovskites, Journal of the European Ceramic Society 24(6) (2004) 1365-1370.
- [32] P.-S. Cho, S.-Y. Park, Y.H. Cho, S.-J. Kim, Y.C. Kang, T. Mori, J.-H. Lee, Preparation of LSGM powders for low temperature sintering, Solid State Ionics 180(11) (2009) 788-791.
- [33] S.L. Reis, E.N.S. Muccillo, Microstructure and electrical conductivity of fast fired Sr- and Mg-doped lanthanum gallate, Ceramics International 42(6) (2016) 7270-7277.

Chapter 5

5. The performance of B-site doped STO₃ in a membrane reactor

Abstract

Developing stable mixed ionic-electronic conducting (MIEC) ceramics as oxygen transport membranes (OTMs) is crucial for their application in membrane reactors, which typically operate under reducing atmospheres. Strontium titanate (SrTiO₃) material demonstrates remarkable thermodynamic stability. In this study, a series B-site doped SrTiO₃ materials SrTi_{0.60}Fe_{0.35}Ni_{0.05}O_{3-δ} (STFN005), SrTi_{0.75}Fe_{0.25}O_{3-δ} (STF25), SrTi_{0.65}Fe_{0.35}O_{3-δ} (STF35) and SrTi_{0.85}Zr_{0.05}Ni_{0.10}O_{3-δ} (STZN10) were synthesized by solid-state reaction method. To enhance surface exchange kinetics and overall oxygen transport efficiency, STF25 and STF35 membranes were further modified with porous STFN005 catalytic layers on the both sides, yielding STF25 cl and STF35 cl, respectively. Oxygen permeation studies under standard conditions (air/Ar gradients), STF35 cl achieved the highest oxygen flux, demonstrating the critical role of the catalytic layer in improving permeability. While STF25 cl exhibits lower oxygen permeability under Ar sweep conditions compared to the pure STFN005 membrane, it shows higher permeability in methane partial oxidation (POM), suggesting the porous STFN005 catalytic layer significantly enhances the catalytic performance through optimized surface exchange kinetics and redox-active sites (Fe/Ni). Structural stability assessments revealed that STF25 cl and STZN10 maintained their integrity under reducing conditions, whereas STFN005 and STF35 cl experience structural fracture due to chemical expansion. As a result, product selectivity identified distinct reaction pathways for each material: STFN005 exhibits high CO selectivity, making it a promising candidate for syngas production via POM; STZN10 demonstrated superior C2 hydrocarbon selectivity, indicating its suitability for oxidative coupling of methane (OCM); STF25 cl and STF35 cl displayed preferential CO₂ selectivity, making them potential candidates for oxy-combustion applications.

5.1 Introduction

Oxygen transport membranes (OTMs) present an advanced solution for pure oxygen supply, offering a more energy-efficient alternative to conventional cryogenic air separation units (ASUs) [1-3]. Utilizing mixed ionic-electronic conductors (MIECs), OTMs selectively transport oxygen ions at high temperatures (700-1000 °C), achieving enhanced performance while minimizing energy consumption. In recent decades, membrane reactors with OTMs have attracted significant attention by integrating air separation and chemical reactions into a single unit. OTMs can be utilized in membrane reactors to facilitate various chemical reactions [4-6], including oxidative coupling of methane (OCM), partial oxidation of methane (POM), oxidative dehydrogenation of ethane (ODHE), water splitting, oxy-combustion and other reactions [5, 7-10]. The key advantages of membrane reactors include: (1) enhanced sustainability through inherent carbon capture and reduced emissions; (2) improved process intensification via thermal integration of exothermic reactions with oxygen separation; (3) higher hydrocarbon conversion rates in processes like OCM and POM, enabled by controlled oxygen dosing; and (4) increased operational safety by preventing explosive oxygen-fuel mixtures. Syngas (CO + H₂) is a key intermediate for methanol synthesis and Fischer-Tropsch (F-T) processes [11] and can be effectively produced via the partial oxidation of methane (POM). This reaction (CH₄ + $1/2O_2 \rightarrow CO + 2H_2$, $\Delta H = -36$ kJ/mol at 25 °C) generates syngas with an optimal H₂/CO ratio of 2, aligning with the stoichiometric needs for methanol and hydrocarbon production [12]. The use of membrane reactors for POM provides significant advantages over conventional methods, cutting operational costs by 20–30% through process intensification [13].

Mixed ionic-electronic conducting (MIEC) perovskite membranes have been widely investigated for syngas production via (POM) in membrane reactors. Among these materials, $SrCo_{0.8}Fe_{0.2}O_{3-\delta}$ (SCF) initially gained attention for its high oxygen flux. However, its structural instability in reducing environments severely limited its practical application, with membranes failing within minutes under POM conditions [14-16]. To enhance stability, research has focused on doping strategies to reinforce the perovskite framework by incorporating higher-valence cations, such as Ba^{2+} [17, 18] and La^{3+} [17, 19] at the A-site, and Zr^{4+} [20], Nb^{5+} [21],

and Ta⁵⁺ [22] at the B-site. Composite materials like BaCo_xFe_yTa_zO_{3-δ} (BCFT) [22] BaCo_xFe_yZr_zO_{3-δ} (BCFZ) [20] have been developed to balance stability and oxygen permeability. BCFT, for instance, has demonstrated more stable than BaCo_{0.7}Fe_{0.2}Nb_{0.1}O_{3-δ} (BCFN), which is one of the highest oxygen flux perovskite materials until now [21]. On the other hand, some studies have focused on surface modification of membranes to enhance POM performance in membrane reactors. As the surface-to-volume ratio increases in a porous catalytic layer, oxygen molecule adsorption and dissociation are promoted, improving overall oxygen permeability [23]. The material used for the porous coating can either be the same as the catalytic layer [24-26] or a different material [27], and it may exhibit ionic and/or electronic conductivity. To prevent expansion or compatibility issues, a porous coating with a composition similar to the dense material is generally preferred. The POM performance of (SrFe)_{0.7}(SrAl₂)_{0.3}O_z, where the material functioned as both a dense membrane and a catalytic layer has been investigated [28]. The CH₄ conversion improved from 5.2% at 850 °C to 16.1% at 950 °C. Furthermore, BSCF membranes coated with Ni/ZrO2 catalysts on the surface achieved near-complete CH₄ conversion with high syngas selectivity [29]. Additionally, Porous catalytic coatings, such as LSCF and LSFT, have been shown to significantly enhance oxygen surface exchange kinetics, improving oxygen flux by 20% and 88% in LSTF-coated BSFC [27] and LSCF-coated CTF membrane systems [30], respectively.

Based on our previous study, SrTi_{0.60}Fe_{0.35}Ni_{0.05}O_{3-δ} (STFN005), SrTi_{0.75}Fe_{0.25}O_{3-δ} (STF25), SrTi_{0.65}Fe_{0.35}O_{3-δ} (STF35) and SrTi_{0.85}Zr_{0.05}Ni_{0.10}O_{3-δ} (STZN10) dense membrane have been selected to evaluate their performance in a membrane reactor in this study. The oxygen permeability of these materials follows the trend: STFN005 > STF35 > STF25 > STZN10. STFN005 was chosen for its good balance between the oxygen permeability and stability as well as Ni exsolution, while STZN10 was selected for its exceptional stability and Ni exsolution properties. To assess the influence of the catalytic layer on oxygen permeability and overall catalytic performance, a porous STFN005 layer was deposited on both sides of STF25 and STF35 dense membranes, named as STF25_cl and STF35_cl, respectively. The oxygen permeability of all samples is evaluated under various conditions, including air/Ar, air/10 vol% CH₄ and 15 vol% CO₂/10 vol% CH₄ atmospheres. The microstructure is assessed following the completion of all tests. Additionally, CH₄ conversion rates and product selectivity are

determined in air/10 vol% CH₄ condition.

5.2 Experimental

5.2.1 Sample preparation

SrTi_{0.60}Fe_{0.35}Ni_{0.05}O_{3-\delta} (STFN005), SrTi_{0.75}Fe_{0.25}O_{3-\delta} (STF25), SrTi_{0.65}Fe_{0.35}O_{3-\delta} (STF35) and SrTi_{0.85}Zr_{0.05}Ni_{0.10}O_{3-δ} (STZN10) ceramic powders were synthesized by the solid-state reaction method. The commercial precursors, including SrCO₃ (Merck, 99%), TiO₂ (Merck, 99%), Fe₂O₃ (Merck, 99%), ZrO₂ (Merck, 99%) and NiO (Merck, 99%) were used as received without further purification. The stoichiometrically formulated precursors underwent mechanochemical homogenization via a ball milling process utilizing Y-stabilized ZrO₂ balls (3 mm) in ethanol for 48 h. The system maintained a mass ratio of powder-to-solvent-to-balls of 1:2:3 to ensure an optimal milling path. Post-milling, the resultant suspension was subjected to solvent evaporation at 70°C, followed by sieving through a 250 µm sieve. Subsequent thermal treatment involved calcination in air at 1200°C for 5 h (5 K/min heating and cooling rate) to achieve phase stabilization. To refine particle size distribution, the calcined product was ball milled again under the same conditions for 24 h, and followed by final drying at 70°C. For the fabrication of MIEC dense membranes, the homogeneous powder was carefully loaded into a cylindrical die with a diameter of 20 mm and pressed at 70 MPa for 1.5 minutes. The resulting pellets were then sintered at 1350°C (STFN005), 1400°C (STF25 and STF35) or 1500°C (STZN10) for 5 h. To achieve the desired dimensions, the membranes were carefully ground using sandpaper, adjusting the final diameter to approximately 15 mm and the thickness to around 0.9 mm.

Once the STF25 and STF35 dense membranes were prepared, porous STFN005 catalytic layers were deposited using the screen-printing technique (Figure 5.1). The first step involved preparing the paste for the porous layer, where the viscosity and material content per gram of paste were key factors in controlling the final layer thickness. The paste was formulated using terpineol with 6 wt.% ethyl cellulose, maintaining a typical powder-to-carrier ratio of 1:1. To facilitate mixing and reduce viscosity, the paste was first heated to 60°C under agitation. It was

then applied onto the screen and printed onto the STF25 and STF35 dense membrane with a diameter of approximately 13 mm. Finally, the membranes were sintered at 1080 °C for 30 min to ensure proper adhesion and porosity of the catalytic layer. The obtained samples were named as STF25_cl and STF35_cl, respectively.

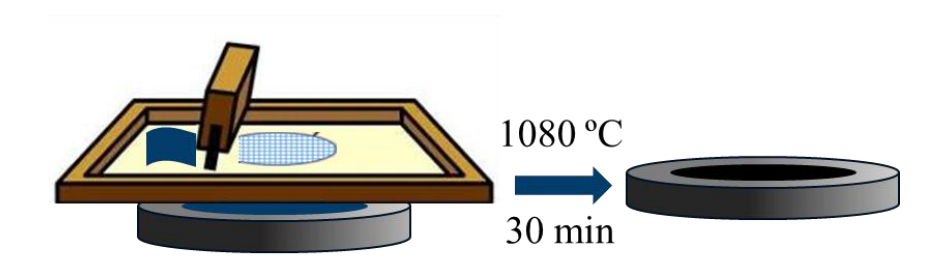


Figure 5.1 Catalytic layer deposition by screen-printing

5.2.2 Structural characterization

Crystalline phase analysis implemented through X-ray diffraction (XRD) using a Bruker D4 ENDEAVOR diffractometer with Cu Kα radiation. Room-temperature measurements spanned a 2θ angular range of 10-80° with an optimized angular increment of 0.02° and a dwell time of 0.75 s/step. Rietveld refinement and phase identification were executed via Profex software. Microstructural features were performed using scanning electron microscopy (SEM, Hitachi TM3000 tabletop) coupled with energy-dispersive X-ray spectroscopy (EDS). Gas-tightness validation, critical for membrane reactor applications, employed a high-sensitivity helium leak detection system (Qualy test HTL 260, Pfeiffer Vacuum GmbH, Asslar, Germany).

5.2.3 Membrane reactor set up

The membrane reactor used for oxygen permeation studies consisted of a lab-scale quartz reactor, as illustrated in Figure 5.2. The feed chamber was supplied with either synthetic air (21 vol% O₂/79 vol% N₂) or 15 vol% CO₂ in N₂, while pure Ar or 10 vol% CH₄ in Ar was used as the sweep gas on the permeate side. Both gas streams were introduced at atmospheric pressure. To ensure the correct gas temperature upon contact with the membrane surface, all inlet gases were preheated—an essential step, particularly at high flow rates. Each gas stream

was individually regulated using mass flow controllers. The membrane temperature was monitored by a thermocouple attached to its surface, with a PID controller maintaining temperature variations within 2 °C of the setpoint. The membrane samples were gastight, disk-shaped, with a diameter of 15 mm, and leak-free operation was ensured using gold O-rings. Permeate analysis was conducted at steady state using an online micro-GC (Varian CP-4900) equipped with Molsieve 5A, Pora-Plot-Q glass capillary, and CP-Sil modules. To verify gastight conditions, nitrogen concentration in the product gas stream was continuously monitored. The data presented in this chapter were recorded under steady-state conditions after 1 hour of exposure to the reaction stream. Each GC analysis was repeated three times to minimize errors, with the experimental analytical error remaining below 0.5%.

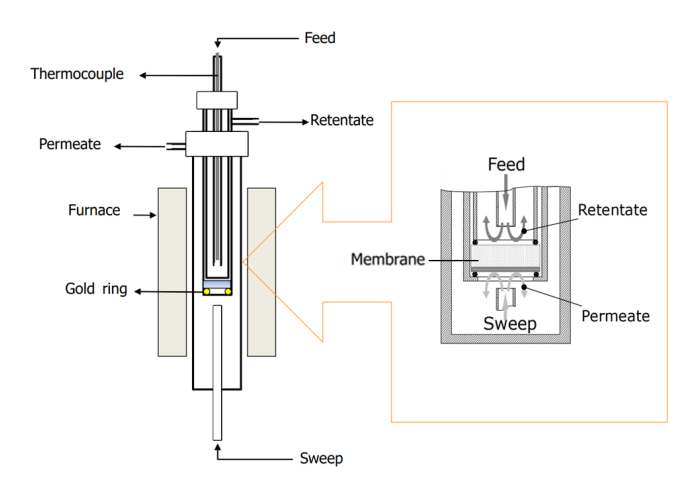


Figure 5.2 Lab-scale MIEC membrane reactor and a zoomed-in view of the membrane reactor [31]

5.3 Results and discussion

5.3.1 Oxygen flux in different conditions

SrTi_{0.60}Fe_{0.35}Ni_{0.05}O_{3-δ} (STFN005)

Figure 5.3 illustrates the oxygen flux of STFN005 under different conditions. The first part of the oxygen permeation study focused on standard conditions, where air was used as the feed gas and argon as the sweep gas. Two different sweep gas flow rates, 150 mL·min⁻¹ and 50

mL·min⁻¹, were applied, while the feed gas flow rate was maintained at 150 mL·min⁻¹. As shown in Figure 5.3(a), the oxygen flux is higher with a higher sweep gas rate. At 950 °C, the oxygen flux (jO₂) values are 0.39 mL·cm⁻²·min⁻¹ and 0.33 mL·cm⁻²·min⁻¹ for sweep gas flow rates of 150 mL·min⁻¹ and 50 mL·min⁻¹, respectively.

The second part of the study investigated oxygen permeation under the reducing condition in the sweep chamber (10 vol% CH₄ in Ar) to evaluate the membrane's performance in the partial oxidation of methane (POM) reaction. The experimental setup used a sweep gas flow rate of 50/150 mL·min⁻¹ and a feed gas flow rate of 150 mL·min⁻¹. As illustrated in Figure 5.3(a), oxygen flux under reducing conditions is higher than that observed under standard conditions at the same gas flow rates. Furthermore, the oxygen flux observed at a sweep flow rate of 150 mL·min⁻¹ is nearly the same as at 50 mL·min⁻¹, indicating that increasing the flow beyond 50 mL·min⁻¹ offers no significant advantage in this case. Therefore, a sweep flow rate of 50 mL·min⁻¹ was used for further experiments under the POM condition. The increased residence time can enhance process efficiency by improving the balance between reactant adsorption and catalytic conversion. The oxygen flux reaches 0.55 mL·cm⁻²·min⁻¹ in the presence of 10 vol% methane in Ar with a sweep flow rate of 50 mL min⁻¹ at 950 °C. This increase is primarily attributed to the significantly lower oxygen partial pressure (po2) on the sweep side containing 10 vol% CH₄ in Ar ($p_{02} \sim 10^{-15}$ bar) compared to pure argon ($p_{02} \sim 10^{-5}$ bar), which generate a higher oxygen partial pressure gradient. Additionally, some degree of reduction of B-site elements, such as Fe and Ni, may occur, leading to increased electronic conductivity and improved oxygen transport. Since the activation energy (Ea) reflects the ratelimiting step in the permeation process, it was calculated under different conditions. Oxygen transport is primarily limited by two mechanisms: surface exchange reactions and bulk diffusion. Bulk diffusion follows Wagner's law and is influenced by temperature, the po2 gradient, membrane thickness, and the ambipolar conductivity. Generally, lower E_a values suggest that oxygen permeation is controlled by bulk diffusion, whereas higher Ea values indicate an increasing contribution from surface exchange reactions. Table 5.1 presents the activation energy values and oxygen flux at 950 °C. For STFN005, the activation energy in Air/10 vol% CH₄ (102.70 kJ·mol⁻¹) is higher than that in Air/Ar (80.52 kJ·mol⁻¹), indicating that oxygen permeation is more limited by surface exchange reactions in the reducing condition. The third part of the oxygen permeation study focused on integrating CO_2 decomposition reaction with the POM reaction. The feed gas consisted of 15 vol% CO_2 in N_2 at a flow rate of 150 mL·min⁻¹, while the sweep gas contained 10 vol% CH_4 in Ar with a flow rate of 50 mL·min⁻¹. The results indicate that the oxygen flux is significantly lower than that under both the standard and POM conditions (Figure 5.3(a)). The lower oxygen flux is primarily due to the reduced p_{O2} on the feed side, as a result of CO_2 decomposition ($CO_2 \rightarrow CO + 1/2O_2$), compared to air. Although the O_2 consumption due to POM reaction on the sweep side can shift the equilibrium of CO_2 decomposition toward larger O_2 production, the overall oxygen partial pressure gradient still remains relatively small. Notably, a sharp increase in oxygen flux is observed in this case when the temperature exceeds 900 °C, indicating that high temperature enhances the efficiency of both reactions by promoting equilibrium conversion and accelerating reaction kinetics.

To evaluate stability, oxygen flux was remeasured under standard conditions after all tests. The results indicate a slight decrease of approximately 5%, likely due to surface coking. Figure 5.3(b) presents the membrane after testing, revealing visible cracks on its surface. These cracks may have resulted from chemical expansion during heating and cooling cycles. After the oxygen permeation studies, both sides of STFN005 membrane were characterized by XRD, as shown in Figure 5.4. The XRD patterns indicate no detectable structural changes, secondary phases, or impurities, confirming that STFN005 remains single phase on the both sides after exposure to the reducing atmosphere. The membrane was also analyzed using SEM to further investigate its surface morphology. Figure 5.5 exhibits SEM images of the feed and sweep sides of the STFN005 membrane after measurements, along with the corresponding EDS mapping of C and Ni element distribution. The images indicate that the membrane can still keep the perovskite microstructure after all the measurements. Clearly C/Ni-enriched parts are observed on the feed side, which is attributed to coking and Ni exsolution in the reducing atmosphere (15 vol% CO₂ in N₂). In contrast, the sweep side exhibits less C enrichment, suggesting a lower degree of coking under 10 vol% CH₄ in Ar.

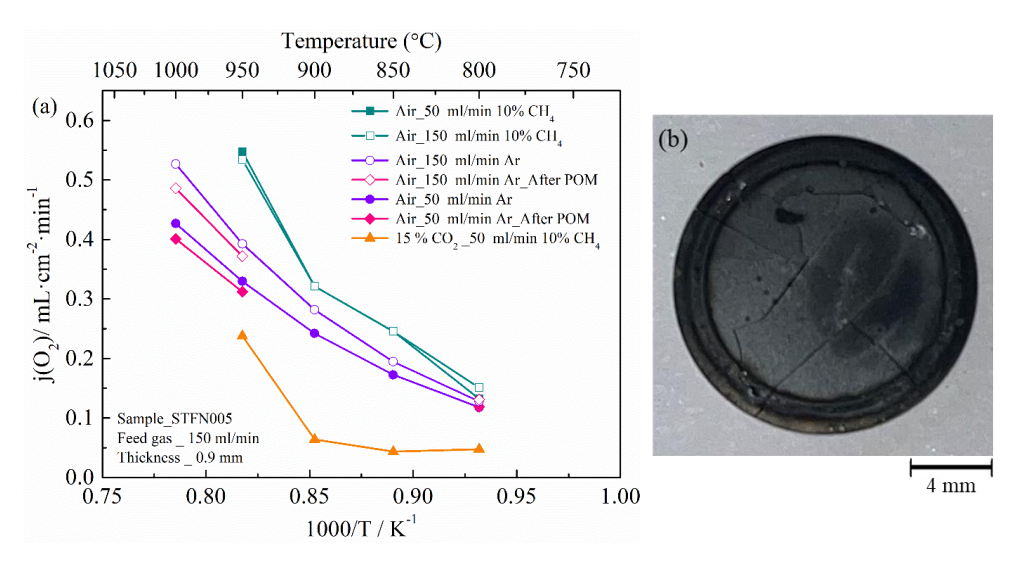


Figure 5.3 (a) Oxygen flux of STFN005 and (b) the membrane after measurements

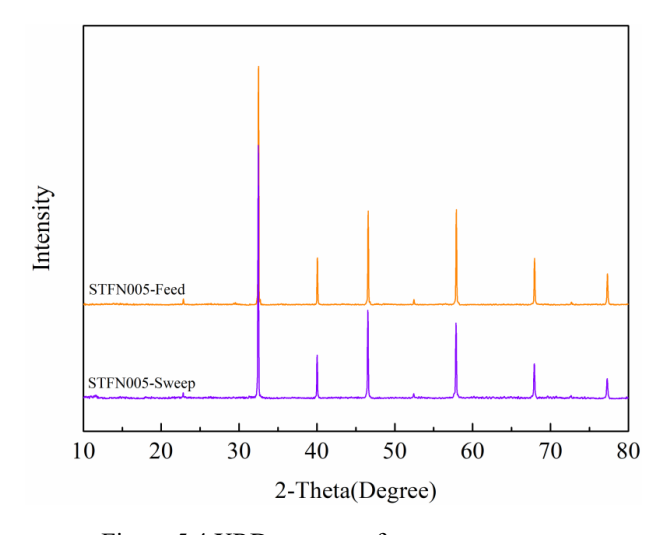


Figure 5.4 XRD patterns after measurements

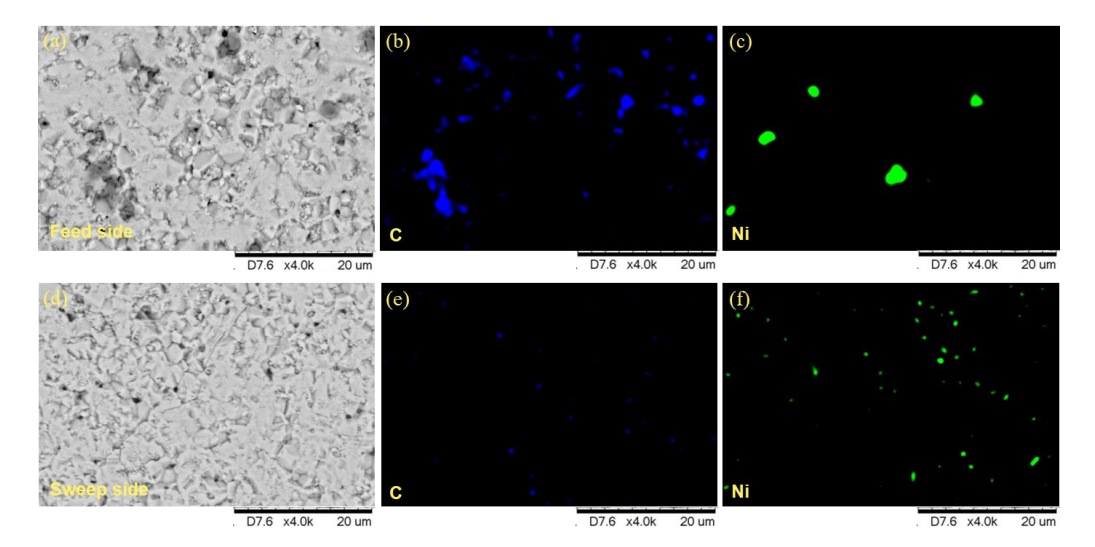


Figure 5.5 SEM images of the STFN005 membrane after measurements: (a–c) feed side and (d–f) sweep side, along with the corresponding EDS mapping.

SrTi_{0.75}Fe_{0.25}O_{3-δ} with STFN005 catalytic layer (STF25_cl)

Since combining CO₂ decomposition reaction and POM is less desirable in our system, the oxygen flux of STF25_cl was measured exclusively under standard conditions (air/Ar) and the reducing atmosphere (air/10 vol% CH₄ in Ar), as shown in Figure 5.6(a). Similar to the behavior observed in the STFN005 material, the oxygen flux of STF25_cl increases with higher sweep gas flow rates (Figure 5.6(a)) due to the enhanced oxygen partial pressure gradient across the membrane, which drives the permeation process. Under standard conditions at 950°C, the oxygen flux is 0.32 mL·cm⁻²·min⁻¹ at a sweep gas flow rate of 150 mL·min⁻¹ and 0.27 mL·cm⁻²·min⁻¹ at 50 mL·min⁻¹.

Remarkably, in the POM reaction environment, the flux increased to 0.78 mL·cm⁻²·min⁻¹ at 920°C, over three times higher than under standard conditions (~0.23 mL·cm⁻²·min⁻¹). Although the flux of STF25_cl is lower than that of STFN005 under standard conditions, its performance in the POM reaction surpasses that of the pure STFN005 dense membrane (Figure 5.6(a)), demonstrating the significant role of the STFN005 catalytic layer in enhancing catalytic performance. Moreover, the activation energy analysis reveals that the STF25 cl membrane exhibits a lower activation energy compared to STFN005 under both

the standard condition and the reducing atmosphere (Table 5.1). This reduction is consistent with the strategy of applying catalytic layers to membrane surfaces, which enhances the amount of surface-active sites and improves oxygen exchange kinetics, resulting in a decrease in activation energy. The oxygen flux after the POM reaction demonstrates that the membrane retains its performance even after testing in a reducing atmosphere (Figure 5.6(a)), showing a good stability. Figure 5.6(b) presents the picture of the STF25_cl membrane after testing, with its morphology remaining intact, indicating good thermochemical stability in the reducing atmosphere. The missing section is due to human error during the removal process and does not indicate material instability.

The SEM images of the feed and sweep sides of the STF25_cl membrane after measurements reveal the STFN005 catalytic layer on the both sides exhibits a highly porous structure with a relatively uniform grain distribution (Figure 5.7). However, some differences can be observed between the both sides. The texture on the sweep side appears slightly coarser, with larger and more irregularly shaped grains compared to the feed side, which displays a more compact and uniform morphology. Additionally, the sweep side shows more obvious variations in surface roughness and porosity, attributed to exposure to the reducing atmosphere. EDS mapping indicates almost no C enrichment on the both sides, suggesting that carbon deposition is negligible (Figure 5.7). This implies that the catalytic layer exhibits good resistance to coking under the tested conditions, maintaining its structural integrity and catalytic performance. Moreover, Ni enrichment is observed on the both sides, which can enhance the catalytic performance of the membrane by promoting surface reactions.

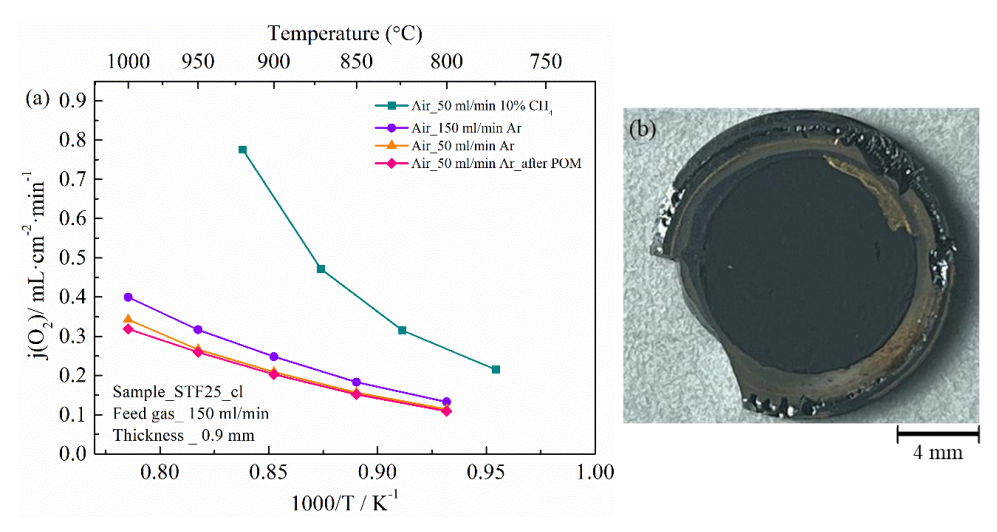


Figure 5.6 (a) Oxygen flux of STF25_cl and (b) the sweep side of the membrane after measurements

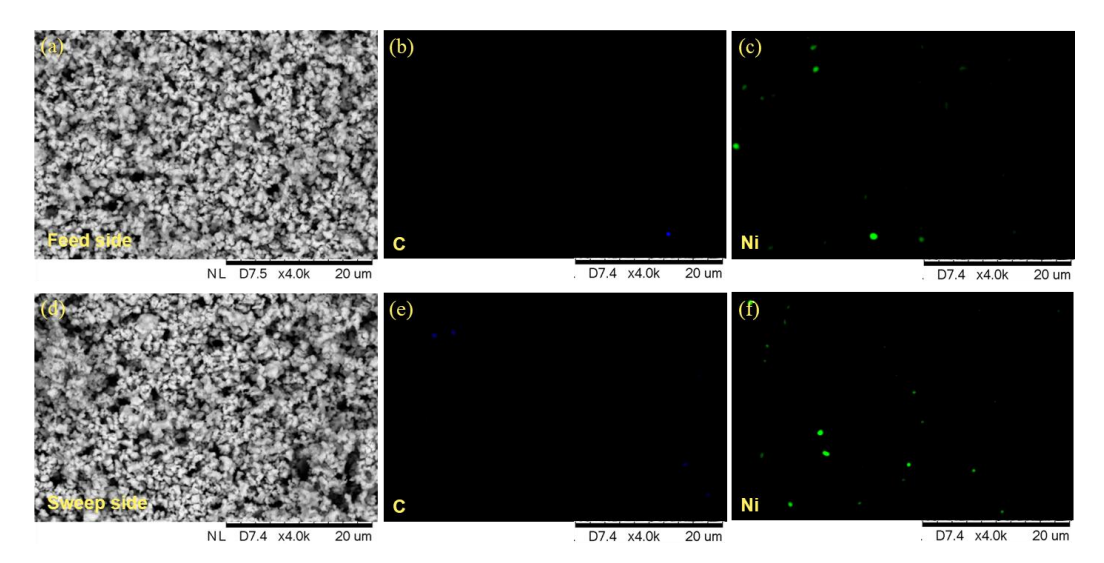


Figure 5.7 SEM images of the STF25_cl membrane after measurements: (a–c) feed side and (d–f) sweep side, along with the corresponding EDS mapping.

SrTi_{0.65}Fe_{0.35}O_{3-δ} with STFN005 catalytic layer (STF35 cl)

Figure 5.8(a) presents the oxygen flux of STF35_cl under different conditions. The measurements were conducted under a standard condition (150 mL·min⁻¹ Air/150 mL·min⁻¹ Ar) and a reducing atmosphere (150 mL·min⁻¹ Air/50 mL·min⁻¹ 10 vol% CH₄ in Ar). At 950 °C, the oxygen flux is 0.46 mL·cm⁻²·min⁻¹ under the standard condition and increases to 0.91 mL·cm⁻²·min⁻¹ in the reducing atmosphere. After the POM reaction, the oxygen flux decreases slightly to 0.22 mL·cm⁻²·min⁻¹, indicating a minor performance decline following exposure to the reducing atmosphere. The activation energy results show that the E_a value of STF35_cl in both standard conditions (54.70 kJ·mol⁻¹) and the reducing atmosphere (81.59 kJ·mol⁻¹) is lower than that of STF25_cl and STFN005 (Table 5.1) due to the improved oxygen surface exchange and bulk diffusion properties, contributing to enhanced permeation efficiency. Figure 5.8(b) shows the STFN005 membrane after testing, where a visible crack is observed on the surface. This crack may have resulted from chemical expansion during heating and cooling cycles.

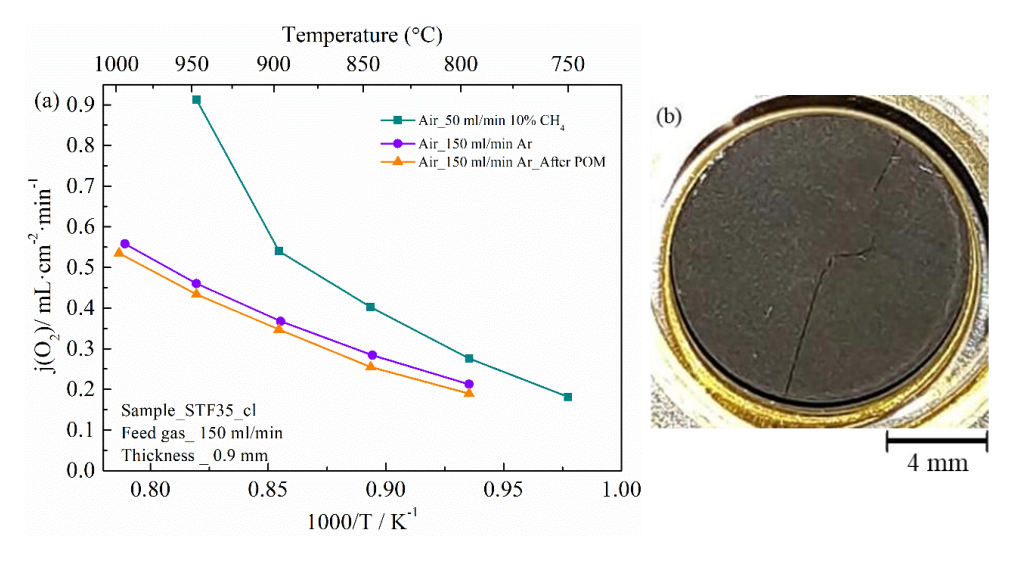


Figure 5.8 (a) Oxygen flux of STF35_cl and (b) the sweep side of the membrane after measurements

SrTi_{0.85}Zr_{0.05}Ni_{0.10}O_{3-δ} (STZN10)

The oxygen flux is 0.084 mL·cm⁻²·min⁻¹ in the standard condition and 0.12 mL·cm⁻²·min⁻¹ at 950 °C in the reducing atmosphere (Figure 5.9(a)), respectively, both are significantly lower than those of the previously discussed materials. After the POM reaction, the oxygen flux further declined to 0.068 mL·cm⁻¹·min⁻¹, indicating a reduction in performance following exposure to the reducing atmosphere. The membrane photograph (Figure 5.9(b)) and SEM image of the sweep side after testing (Figure 5.10) show that the membrane morphology remains intact, demonstrating excellent thermochemical stability in the reducing atmosphere. EDS mapping reveals minimal carbon enrichment on the sweep side, suggesting that carbon deposition is negligible and the membrane exhibits strong resistance to coking under reducing conditions. Additionally, the presence of Ni particles is also observed, which may contribute to enhanced catalytic performance. The XRD results (Figure 5.11) show that STZN10 are still single phase after the measurements in the reducing atmosphere, while additional Au peaks are found in STZN10, which are attributed to gold residue from the sealing process. This indicates that STZN10 exhibits high stability under reducing conditions.

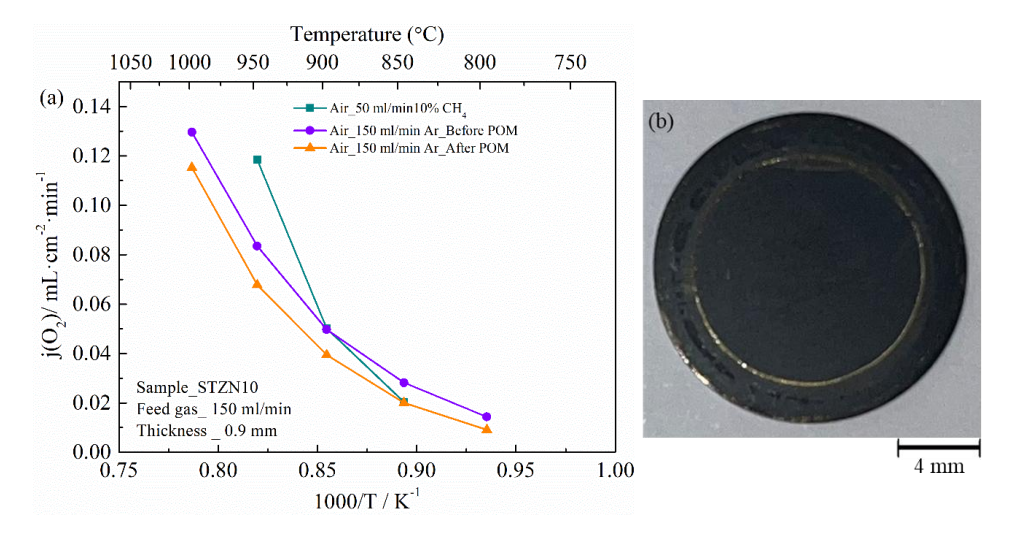


Figure 5.9 (a) Oxygen flux of STZN10 and (b) the membrane after measurements

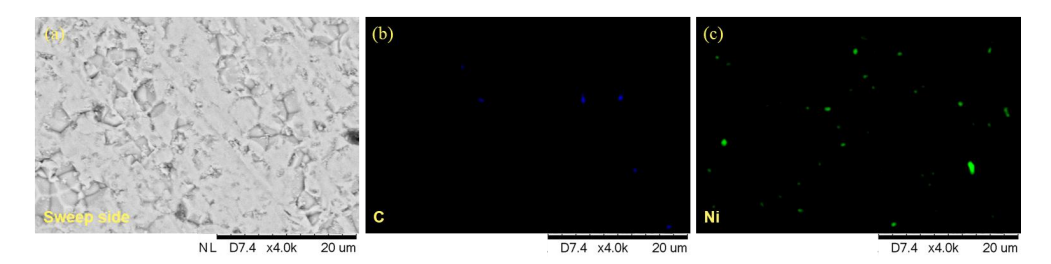


Figure 5.10 SEM images of the sweep side of STZN10 membrane after measurements and the corresponding EDS mapping.

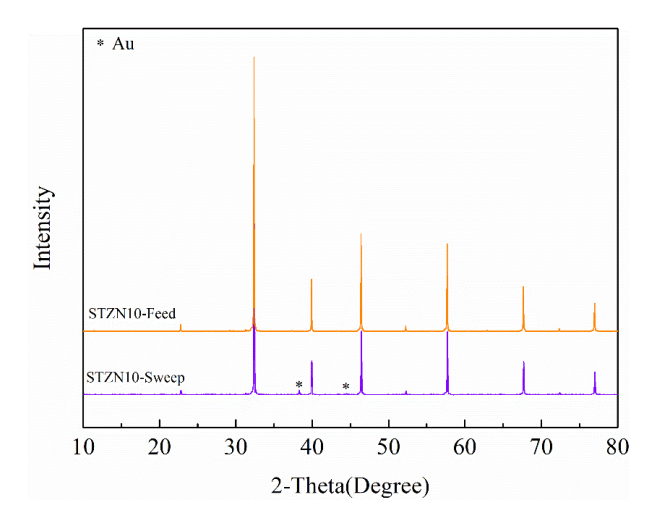


Figure 5.11 XRD patterns after measurements

Table 5.1 Oxygen flux and the activation energy E_{a} of different materials in different conditions

			O ₂ flux	O ₂ flux	Ea	Ea
Materials	T	Catalytic	(Air/Ar)	(Air/10 vol% CH ₄)	(Air/Ar)	(Air/10 vol% CH ₄)
	(°C)	layer	(150/ 150 mL·min ⁻¹)	(150/ 50 mL·min ⁻¹)	kJ·mol⁻¹	kJ·mol⁻¹
			mL·cm ⁻² ·min ⁻¹	$mL \cdot cm^{-2} \cdot min^{-1}$		
STFN005	950	-	0.39	0.55	80.52	102.70
STF25_cl	920	STFN005	0.32	0.78	62.70	91.20
STF35_cl	950	STFN005	0.46	0.91	54.70	81.59
STZN10	950	-	0.084	0.12	123.07	197.44

Figure 5.12 compares the oxygen flux comparison among STFN005, STF25_cl, STF35_cl and STZN10 under POM reaction condition. The oxygen flux of STF25_cl and STF35_cl are comparable, both are higher that STFN005 and STZN10 due the enhanced performance by the catalytic layer.

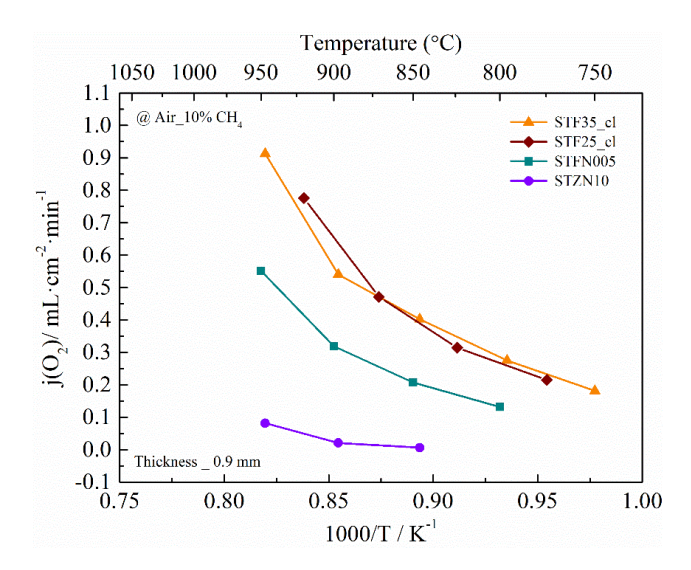


Figure 5.12 Oxygen flux comparison among STFN005, STF25_cl, STF35_cl and STZN10 in POM reaction condition

5.3.2 CH₄ conversion and selectivity

Figure 5.13 and Table 5.2 show CH₄ conversion and the selectivity for all the reaction products generated during the catalytic test for the performed experiments at 950 °C. Although the methane conversion efficiency of STF25_cl (12.4 \pm 0.9 %) and STF35_cl (13.2 \pm 0.2 %) is slightly higher than that of STFN005 (11.1 \pm 0.4 %) under identical partial oxidation of methane (POM) conditions, their product selectivity profiles exhibit a marked difference. While STFN005 achieves a CO selectivity of 40.2 ± 0.5 %, the STF25_cl and STF35_cl exhibit drastically reduced values of 11.2 ± 0.9 % and 11.0 ± 0.6 %, respectively—representing an approximately fourfold decline in performance. This performance gap suggests that STFN005 possesses a greater number of active sites that synergistically optimize both methane activation and intermediate CO stabilization. The superior CO selectivity of STFN005 likely stems from

its higher density of redox-active metal centers (e.g., Ni^0/Ni^{2+}), which play a crucial role in facilitating the kinetically challenging C–O coupling step while suppressing undesired deep oxidation pathways leading to CO_2 formation. In contrast, while STF25_cl and STF35_cl enhance methane dissociation rates, their lower CO selectivity may be attributed to the insufficient availability of redox-active sites or weaker stabilization of CO intermediates could promote excessive oxidation, leading to an increased formation of CO_2 rather than CO. Additionally, differences in catalyst microstructure, oxygen mobility, or metal-support interactions might further contribute to the observed variations in selectivity. Notably, while the CH₄ conversion of STZN10 (3.9 \pm 0.2 %) is significantly lower than that of the other membranes, it exhibits exceptional selectivity toward C_2 hydrocarbons (C_2H_4/C_2H_6), reaching 70.3 \pm 0.9 %. This high selectivity suggests that STZN10 holds great potential for oxidative coupling of methane (OCM), a process that benefits from limited O_2 availability to suppress unwanted deep oxidation and enhance C_2 product yield. The superior C_2 selectivity of STZN10 may be attributed to its optimized active sites, which facilitate CH_4 activation while effectively minimizing the formation of CO and CO_2 byproducts.

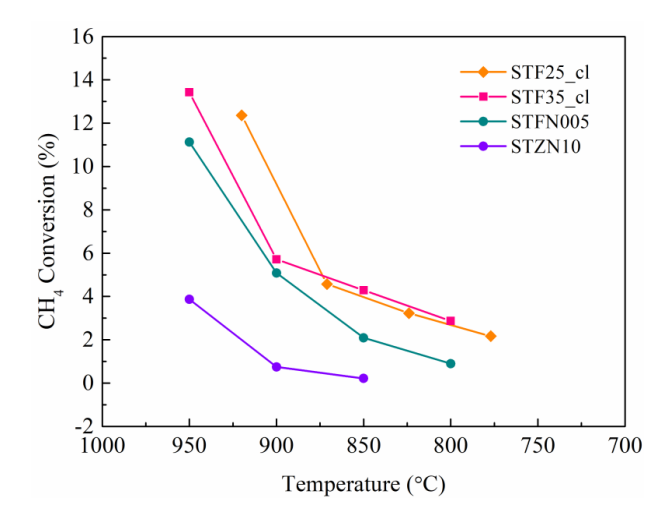


Figure 5.13 CH₄ conversion comparison among STFN005, STF25_cl, STF35_cl and STZN10 in POM reaction condition

Table 5.2 The conversion and selectivity of different materials at 950 °C

Materials	T	Catalytic layer	Conversion	Sco (%)	S _{CO2} (%)	S _{C2} (%)	Thickness
	(°C)		(%)				(mm)
STFN005	950	-	11.1 ± 0.4	40.2 ± 0.5	23.4 ± 1.0	36.3 ± 0.6	0.9
STF25_cl	920	STFN005	12.4 ± 0.9	11.2 ± 0.9	53.9 ± 0.6	34.9 ± 0.6	0.9
STF35_cl	950	STFN005	13.2 ± 0.2	11.0 ± 0.6	46.3 ± 0.9	42.7 ± 0.8	0.9
STZN10	950	-	3.9 ± 0.2	16.3 ± 1.1	13.4 ± 0.2	70.3 ± 0.9	0.9

5.4 Conclusions

This study investigates and compares the oxygen flux and catalytic performance of SrTi_{0.60}Fe_{0.35}Ni_{0.05}O_{3-δ} (STFN005), SrTi_{0.75}Fe_{0.25}O_{3-δ} with STFN005 catalytic layer (STF25 cl), $SrTi_{0.65}Fe_{0.35}O_{3-\delta}$ with STFN005 catalytic layer (STF35 cl) and $SrTi_{0.85}Zr_{0.05}Ni_{0.10}O_{3-\delta}$ (STZN10) as OTMs in a membrane reactor. The oxygen flux of STFN005 is studied in three different conditions, which are air/Ar, air/10 vol% CH₄ and 15 vol% CO₂/10 vol% CH₄. The results show that the oxygen flux in air/10 vol% CH₄ (0.55 mL·cm⁻²·min⁻¹) is higher than in other conditions. The activation energy in air/10 vol% CH₄ and air/Ar suggests that oxygen transport is more constrained by surface exchange reactions under reducing conditions. Additionally, oxygen flux in 15 vol% CO₂/10 vol% CH₄ is significantly lower than in other gas environments due to the much lower po2 gradient. A slight decline of approximately 5% of remeasured oxygen flux after all tests indicates the good stability of STFN005. While the perovskite structure of STFN005 remains intact after the measurements confirmed by XRD, the sample fractures due to chemical expansion. Furthermore, Ni exsolution is observed on the membrane surface after the experiments. For STF25 cl, although STF25 cl exhibits lower oxygen permeability under air/Ar compared to the pure STFN005 membrane, it shows higher oxygen flux in air/10 vol% CH₄, suggesting the porous STFN005 catalytic layer significantly enhances the catalytic performance through optimized surface exchange kinetics and redoxactive sites (Fe/Ni). Moreover, STF25 cl remains structurally intact, indicating good thermochemical stability in the reducing atmosphere. The SEM images of the feed and sweep sides of the STF25 cl membrane reveal the STFN005 catalytic layer on the both sides still exhibits a highly porous structure with a relatively uniform grain distribution after measurements. The activation energy analysis in air/Ar and air/10 vol% CH₄ conditions reveals that STF35_cl exhibits a lower activation energy compared to STF25_cl and STFN005 due to the improved oxygen surface exchange and bulk diffusion properties, contributing to enhanced permeation efficiency. However, the STF35_cl dense membrane fractures after measurements in the reducing atmosphere due to chemical expansion. For STZN10, although the oxygen flux is much lower than the other compositions of this study, the membrane photograph and SEM image of the sweep side after testing show the material exhibits excellent thermochemical stability in the reducing atmosphere. Product selectivity identified distinct reaction pathways for each material: STFN005 exhibits high CO selectivity, making it a promising candidate for syngas production via POM; STZN10 demonstrated superior C₂ hydrocarbon selectivity, indicating its suitability for oxidative coupling of methane (OCM); STF25_cl and STF35_cl displayed preferential CO₂ selectivity, making them potential candidates for oxy-combustion applications. Moreover, the investigation on optimizing membrane architecture through precise thickness control and asymmetric structural fabrication in the further can further enhance membrane performance for the target reactions in a membrane reactor.

REFERENCES

- [1] F. Wu, M. Argyle, P. Dellenback, M. Fan, Progress in O2 separation for oxy-fuel combustion—A promising way for cost-effective CO2 capture: A review, Progress in Energy and Combustion Science 67 (2018).
- [2] R.J. Allam, Improved oxygen production technologies, Energy Procedia 1(1) (2009) 461-470.
- [3] N.F. Himma, A.K. Wardani, N. Prasetya, P.T.P. Aryanti, I.G. Wenten, Recent progress and challenges in membrane-based O2/N2 separation, 35(5) (2019) 591-625.
- [4] J. Sunarso, S.S. Hashim, N. Zhu, W. Zhou, Perovskite oxides applications in high temperature oxygen separation, solid oxide fuel cell and membrane reactor: A review, Progress in Energy and Combustion Science 61 (2017) 57-77.
- [5] F. Schulze-Küppers, F. Drago, L. Ferravante, S. Herzog, S. Baumann, P. Pinacci, W.A. Meulenberg, Design and fabrication of large-sized planar oxygen transport membrane components for direct integration in oxy-combustion processes, Separation and Purification Technology 220 (2019) 89-101.
- [6] G. Zhang, W. Jin, N. Xu, Design and Fabrication of Ceramic Catalytic Membrane Reactors for Green Chemical Engineering Applications, Engineering 4(6) (2018) 848-860.
- [7] J. Garcia-Fayos, M.P. Lobera, M. Balaguer, J.M. Serra, Catalyst Screening for Oxidative Coupling of Methane Integrated in Membrane Reactors, Frontiers in Materials 5 (2018).
- [8] H. Wang, Y. Cong, W. Yang, Investigation on the partial oxidation of methane to syngas in a tubular Ba0.5Sr0.5Co0.8Fe0.2O3-δ membrane reactor, Catalysis Today 82(1) (2003) 157-166.
- [9] R. Schucker, G. Dimitrakopoulos, K. Derrickson, K. Kopec, F. Al-Ahmadi, J. Johnson, L. Shao, A. Ghoniem, Oxidative Dehydrogenation of Ethane to Ethylene in an Oxygen Ion Transport Membrane Reactor A Proposed Design for Process Intensification, Industrial & Engineering Chemistry Research 58 (2019).
- [10] Z. Cao, H. Jiang, H. Luo, S. Baumann, W.A. Meulenberg, H. Voss, J. Caro, Simultaneous overcome of the equilibrium limitations in BSCF oxygen-permeable membrane reactors: Water splitting and methane coupling, Catalysis Today 193(1) (2012) 2-7.

- [11] H. Jiang, S. Wang H Fau Werth, T. Werth S Fau Schiestel, J. Schiestel T Fau Caro, J. Caro, Simultaneous production of hydrogen and synthesis gas by combining water splitting with partial oxidation of methane in a hollow-fiber membrane reactor, (1521-3773 (Electronic)).
- [12] V.V. Kharton, A.A. Yaremchenko, A.V. Kovalevsky, A.P. Viskup, E.N. Naumovich, P.F. Kerko, Perovskite-type oxides for high-temperature oxygen separation membranes, Journal of Membrane Science 163(2) (1999) 307-317.
- [13] J. Sunarso, S. Baumann, J.M. Serra, W.A. Meulenberg, S. Liu, Y.S. Lin, J.C. Diniz da Costa, Mixed ionic–electronic conducting (MIEC) ceramic-based membranes for oxygen separation, Journal of Membrane Science 320(1-2) (2008) 13-41.
- [14] U. Balachandran, J.T. Dusek, P.S. Maiya, B. Ma, R.L. Mieville, M.S. Kleefisch, C.A. Udovich, Ceramic membrane reactor for converting methane to syngas, Catalysis Today 36(3) (1997) 265-272.
- [15] U. Balachandran, B. Ma, Mixed-conducting dense ceramic membranes for air separation and natural gas conversion, Journal of Solid State Electrochemistry 10(8) (2006) 617-624.
- [16] B.J. Mitchell, R.C. Rogan, J.W. Richardson, B. Ma, U. Balachandran, Stability of the cubic perovskite SrFe0.8Co0.2O3–δ, Solid State Ionics 146(3) (2002) 313-321.
- [17] C.-Y. Tsai, A.G. Dixon, W.R. Moser, Y.H. Ma, Dense perovskite membrane reactors for partial oxidation of methane to syngas, AIChE Journal 43(S11) (1997) 2741-2750.
- [18] H. Dong, Z. Shao, G. Xiong, J. Tong, S. Sheng, W. Yang, Investigation on POM Reaction in a New Perovskite Membrane Reactor, Catalysis Today CATAL TODAY 67 (2001) 3-13.
- [19] H.J.M. Bouwmeester, Dense ceramic membranes for methane conversion, Catalysis Today 82(1) (2003) 141-150.
- [20] J. Tong, W. Yang, R. Cai, B. Zhu, L. Lin, Novel and Ideal Zirconium-Based Dense Membrane Reactors for Partial Oxidation of Methane to Syngas, Catalysis Letters 78(1) (2002) 129-137.
- [21] M. Harada, K. Domen, M. Hara, T. Tatsumi, Ba1.0Co0.7Fe0.2Nb0.1O3–δ Dense Ceramic as an Oxygen Permeable Membrane for Partial Oxidation of Methane to Synthesis Gas, Chemistry Letters 35(12) (2006) 1326-1327.
- [22] H. Luo, Y. Wei, H. Jiang, W. Yuan, Y. Lv, J. Caro, H. Wang, Performance of a ceramic membrane reactor with high oxygen flux Ta-containing perovskite for the partial oxidation of

- methane to syngas, Journal of Membrane Science 350(1-2) (2010) 154-160.
- [23] Q. Jiang, S. Faraji, D.A. Slade, S.M. Stagg-Williams, Chapter 11 A Review of Mixed Ionic and Electronic Conducting Ceramic Membranes as Oxygen Sources for High-Temperature Reactors, in: S.T. Oyama, S.M. Stagg-Williams (Eds.), Membrane Science and Technology, Elsevier2011, pp. 235-273.
- [24] M.A. Peña, J.L.G. Fierro, Chemical Structures and Performance of Perovskite Oxides, Chemical Reviews 101(7) (2001) 1981-2018.
- [25] J. Gurauskis, Ø.F. Lohne, K. Wiik, La0.2Sr0.8Fe0.8Ta0.2O3-δ based thin film membranes with surface modification for oxygen production, Solid State Ionics 225 (2012) 703-706.
- [26] S. Cheng, H. Huang, S. Ovtar, S.B. Simonsen, M. Chen, W. Zhang, M. Søgaard, A. Kaiser, P.V. Hendriksen, C. Chen, High-Performance Microchanneled Asymmetric Gd0.1Ce0.9O1.95–δ–La0.6Sr0.4FeO3–δ-Based Membranes for Oxygen Separation, ACS Applied Materials & Interfaces 8(7) (2016) 4548-4560.
- [27] J.P. Kim, J.H. Park, E. Magnone, Y. Lee, Significant improvement of the oxygen permeation flux of tubular Ba0.5Sr0.5Co0.8Fe0.2O3-δ membranes covered by a thin La0.6Sr0.4Ti0.3Fe0.7O3-δ layer, Materials Letters 65(14) (2011) 2168-2170.
- [28] A.A. Yaremchenko, A.A. Kharton Vv Fau Valente, S.A. Valente Aa Fau Veniaminov, V.D. Veniaminov Sa Fau Belyaev, V.A. Belyaev Vd Fau Sobyanin, F.M.B. Sobyanin Va Fau Morques, F.M. Morques, Mothers, evidetion, ever mixed conducting, SrEe(Al)O3 delta.
- Marques, F.M. Marques, Methane oxidation over mixed-conducting SrFe(Al)O3-delta-SrAl2O4 composite, (1463-9076 (Print)).
- [29] Z. Shen, P. Lu, J. Hu, X. Hu, Performance of Ba0.5Sr0.5Co0.8Fe0.2O3+δ membrane after laser ablation for methane conversion, Catalysis Communications 11(10) (2010) 892-895.
- [30] M. Jacobs, M.L. Fontaine, R. Bredesen, B. Michielsen, V. Middelkoop, Y. Larring, F. Snijkers, Surface activation of asymmetric CaTi1–xFexO3–δ tubular membranes for oxygen separation, Journal of Membrane Science 477 (2015) 58-64.
- [31] J.G. Fayos, Development of ceramic miec membranes for oxygen separation: application in catalytic industrial processes Universitat Politècnica de València, 2017.

Chapter 6

6. Reflections and Conclusions

6.1 Introduction

This chapter presents a summary of the key achievements and conclusions regarding the development of B-site doped STO₃ as a potential oxygen transport membrane for membrane reactor applications, where the operating environment typically involves exposure to reducing gases. The primary objective of this study is to achieve an optimal balance between material stability and oxygen permeability, which is essential for improving membrane reactor performance. This is accomplished through the strategic doping of various elements at the Bsite of the highly stable STO₃ structure to improve the oxygen transport performance. The selection of dopant elements plays an important role in modifying the perovskite lattice and, consequently, influencing its functional properties. Depending on the chosen dopants, the material's ability to conduct oxygen ions and electrons can be either enhanced or inhibited. Based on tolerance factor calculations, Fe, Ni, and similar redox-active elements, as well as less redox-active elements like Mg and Al, are selected for B-site doping in SrTiO₃ for this work. The substitution of Ti with these elements introduces mixed ionic and electronic conductivity, enhancing the material's functionality. Among them, Ni is particularly promising due to its strong catalytic properties. In this study, dense membranes of Fe/Ni co-doped STO₃ materials $SrTi_{0.65-x}Fe_{0.35}Ni_xO_{3-\delta}$ (x=0, 0.05, 0.075, 0.1) (STFN_x), Zr/Ni co-doped STO₃ materials SrTi_{0.95-x}Zr_{0.05}Ni_xO_{3-δ} (x=0.01, 0.03, 0.05, 0.10, 0.15) (STZN_x), Al-doped STF35 materials $SrTi_{0.65-x}Fe_{0.35}Al_xO_{3-\delta}$ (x=0.01, 0.03, 0.05, 0.10, 0.15) (STFA_x) and Mg-doped STF35 materials $SrTi_{0.65-x}Fe_{0.35}Mg_xO_{3-\delta}$ (x=0.01, 0.03, 0.05, 0.10) (STFM_x) are prepared and systematically studied. The findings from powder synthesis, microstructural analysis, conductivity, oxygen permeation measurements, Ni exsolution phenomenon and stability are discussed in the following sections, along with recommendations for future research.

Additionally, the performance of these materials in a membrane reactor is thoroughly evaluated to assess their efficiency in target applications. This work aims to contribute to the advancement of high-performance oxygen transport membranes that exhibit both stability and efficiency under the demanding conditions of membrane reactors.

6.1.1 Samples selection

The impact of Fe/Ni co-doping at the B-site of STO₃ on its structural and functional properties for application as an oxygen transport membrane (OTM) is explored in Chapter 2. The $SrTi_{0.65-x}Fe_{0.35}Ni_xO_{3-\delta}$ (x=0, 0.05, 0.075, 0.1) (STFN_x) materials are successfully synthesized using the solid-state reaction method. To obtain dense membranes, the Ni-free SrTi_{0.65}Fe_{0.35}O₃₋ δ (STF35) is sintered at 1400 °C, while Ni-doped samples are sintered at 1350 °C. XRD analysis confirms that Ni is soluble in the perovskite structure up to a concentration of 10 mol% in the studied range. The findings indicate that Ni doping at the B-site enhances both the electronic and ionic conductivities of STF35, primarily due to the increased oxygen vacancy concentration resulting from the substitution of Ti by Ni. The oxygen permeance of STFN_x slightly increases with Ni concentration and is comparable to that of the benchmark material LSCF6428. Notably, Fe and Ni exsolution is clearly observed on the surfaces of STF35 and STFN_x after annealing in reducing atmospheres, and these exsolved particles can serve as active catalytic centers. All samples still possess the main peaks of perovskite even if annealed in a very harsh condition, i.e. syngas with high H₂S contamination (~1000 ppm), indicating good structural stability in harsh environments. However, the stability of STFN_x decreases as Ni content increased, which can be attributed to the intensified formation of secondary phases, as evidenced by the rising intensity of their XRD peaks. A key observation is that the 5 mol% Ni-doped material STFN005 exhibits a uniformly distributed Fe/Ni exsolution after annealing in a reducing atmosphere, which could enhance catalytic performance in membrane reactors. Additionally, two-cycle TGA measurements reveal that mass loss increases with increasing Ni content. STF35 and STFN005 exhibit comparable mass loss values that remain relatively stable across both cycles. In contrast, STFN0075 and STFN010 show significantly greater mass loss, which further increases during the second cycle. XRD analysis after the two-cycle TGA tests

confirms that STF35 and STFN005 retain a single-phase structure, whereas additional NiO peaks are observed in STFN0075 and STFN010, indicating secondary phase formation. These results demonstrate that STF35 and STFN005 possess greater stability under reducing conditions compared to STFN0075 and STFN010. Therefore, STFN005, with 5 mol% Ni doping, emerges as a promising candidate for partial oxidation of methane (POM) applications in membrane reactors

Chapter 3 provides a systematic investigation into the microstructure, functional properties, and stability of the SrTi_{0.95-x}Zr_{0.05}Ni_xO_{3-δ} (x=0.01, 0.03, 0.05, 0.10, 0.15) (STZN_x) series materials for their potential use as OTMs. The single-phase materials STZN1, STZN3, STZN5, and STZN10 are successfully synthesized using the solid-state reaction method and subsequently sintered at 1500 °C to produce dense membranes. XRD analysis confirmed that the solubility limit of Ni in the perovskite structure is below 15 mol%. The results indicate that substituting Ti with Ni significantly introduces the oxygen permeability and electrical conductivity of STZN_x compared to undoped SrTi_{0.95}Zr_{0.05}O₃. An increase in Ni content correlates with improved performance, and all samples maintain their single-phase structure even after annealing in 2.9 vol% H₂/Ar for 48 hours, indicating high stability under reducing atmospheres. Notably, STZN10 exhibits a uniform distribution of Ni particles on its surface after annealing, which can serve as active catalytic centers in membrane reactor applications. Three-cycle TGA measurements reveal that all STZN_x materials demonstrate reversible oxygen exchange, further indicating excellent stability in reducing atmospheres.

Although the oxygen flux of STZN10 is lower than that of many B-site doped SrTiO₃ materials due to its lower oxygen vacancy concentration, it presents unique advantages for OTM applications, particularly in high-temperature membrane reactors involving hydrocarbon processing:

- (1) Ni exsolution under reducing conditions generates catalytically active sites on the surface, enhancing reaction kinetics
- (2) the material exhibits exceptional structural stability under harsh operating conditions.

 To further improve its oxygen permeability, several optimization strategies can be considered, including establishing a gradient oxygen partial pressure driving force based on specific

applications, fabricating ultrathin dense layers (e.g., $<50 \mu m$) to reduce diffusion resistance, designing asymmetric membranes with a composite support-functional layer structure, or incorporating a catalytic surface layer to lower surface exchange resistance. These strategies position STZN10 as a promising candidate for high-temperature membrane reactor applications that integrate separation and reaction processes, such as the partial oxidation of methane, where both catalytic activity and structural stability are critical.

The microstructures and oxygen permeability of SrTi_{0.65-x}Fe_{0.35}Al_xO_{3-δ} (x=0.01, 0.03, 0.05, 0.10, 0.15) (STFA_x) and SrTi_{0.65-x}Fe_{0.35}Mg_xO_{3-\delta} (x=0.01, 0.03, 0.05, 0.10) (STFM_x) series materials is studied in Chapter 4. All samples are successfully synthesized and sintered at 1400 °C to obtain dense membranes. XRD analysis confirmed that the STFA_x samples maintain a single-phase structure across the studied composition range (up to 15 mol%). In contrast, the solubility limit of Mg in the STFM_x series is below 10 mol%. Oxygen permeation measurements reveal that all STFA_x samples exhibit lower oxygen permeance compared to STF35 due to unfavorable substitution effects, indicating Al doping is unsuitable for this system. A comparative analysis is conducted between Mg doped STF35 samples synthesized using standard MgO powder (STFM_x standard) and those synthesized with nano-sized MgO powder (STFM_x). The permeance of STFM_x standard membranes decrease as Mg content increased, with distinct black regions appearing on the surface of STFM3 standard. These secondary phases are likely due to oversized MgO particles failing to integrate fully into the structure, thereby negatively impacting permeability. While STFM_x samples with no visible dark regions on the surface demonstrated higher oxygen permeance than STFMx standard, the overall permeance values remain comparable to undoped STF35, except for STFM10, which showed a reduced permeance. TGA indicated that oxygen concentration changes in STFM_x increase with higher Mg content, higher temperatures, and lower oxygen partial pressures. However, these trends did not align with the oxygen permeance measurements. MgO segregation is observed by SEM and EDS mapping on STFM_x materials, which negatively impacted the oxygen permeability of the materials. Consequently, understanding and mitigating MgO segregation is crucial for optimizing material performance.

Given these findings, although the oxygen permeance of STFM_x is suboptimal, several

optimization strategies could be employed to minimize MgO segregation and enhance permeability:

- (1) Adopting sol-gel or chemical precursor synthesis methods to achieve atomic-scale homogeneity in the initial powder, reducing localized Mg-rich regions.
- (2) Utilizing controlled-atmosphere sintering (e.g., in inert or reducing environments) to stabilize the lattice and inhibit secondary phase formation.
- (3) Employing rapid sintering techniques such as spark plasma sintering (SPS) or field-assisted sintering (FAST) to minimize high-temperature exposure and limit time-dependent Mg diffusion.

Provided these approaches are successfully implemented, STFMx could still hold potential as a promising candidate for oxygen transport membranes (OTMs) in membrane reactor applications.

6.1.2 Performance in a membrane reactor

Chapter 5 explores the oxygen flux and catalytic performance of selected materials, including STFN005, STF25 with STFN005 catalytic layer (STF25_cl), STF35 with STFN005 catalytic layer (STF35_cl), and STZN10 for use as OTMs in a membrane reactor.

The oxygen flux of STFN005 is evaluated under three different gas environments: air/Ar, air/10 vol% CH₄ and 15 vol% CO₂/10 vol% CH₄. The results indicate that the highest oxygen flux of STFN005 (0.55 mL·cm⁻²·min⁻¹) is achieved in air/10 vol% CH₄ with a sweep flow rate of 50 mL·min⁻¹ at 950 °C, suggesting that POM promotes oxygen transport. The activation energy analysis in air/Ar and air/10 vol% CH₄ confirms that surface exchange reactions primarily govern oxygen transport under reducing conditions. The oxygen flux in 15 vol% CO₂/10 vol% CH₄ was significantly lower due to the much-reduced oxygen partial pressure gradient. The remeasured oxygen flux after testing demonstrates the good stability of STFN005. XRD analysis confirms that the perovskite structure remains intact post-measurement; however, the membrane fractured due to chemical expansion when sealed in the quartz glass housing. Additionally, Ni exsolution is observed on the membrane surface after the experiments as intended.

For STF25_cl, despite exhibiting lower oxygen permeability than STFN005 under air/Ar condition due to lower Fe content, it demonstrates higher permeability in air/10 vol% CH₄. This improvement suggests that the porous STFN005 catalytic layer significantly improves catalytic performance through enhanced surface exchange kinetics and the exsolution of redoxactive Fe/Ni sites. Furthermore, STF25_cl remained structurally intact, indicating strong thermochemical stability in reducing atmospheres. SEM images of the feed and sweep sides of STF25_cl confirmed that the STFN005 catalytic layer still maintains its highly porous structure with a uniform particle distribution after testing.

Activation energy analysis in air/Ar and air/10 vol% CH₄ reveals that STF35_cl exhibits improved oxygen surface exchange and bulk diffusion properties compared to STFN005 and STF25_cl. However, like STFN005, STF35_cl also fractures after exposure to the reducing atmosphere due to chemical expansion.

STZN10 exhibits the lowest oxygen flux among the studied materials. However, the post-experiment membrane photograph and the SEM images of the sweep side demonstrates its excellent thermochemical stability in reducing environments.

Product selectivity analysis suggests distinct reaction pathways for each material:

- (1) STFN005 exhibits high CO selectivity, making it a strong candidate for syngas production via partial oxidation of methane (POM).
- (2) STF25_cl and STF35_cl favored CO₂ production, indicating their suitability for oxy-combustion applications.
- (3) STZN10 demonstrated superior selectivity for C₂ hydrocarbons, suggesting its potential for oxidative coupling of methane (OCM).

Detailed studies are still needed to understand the potential reaction mechanisms. Further optimization of membrane architecture, including precise thickness control and asymmetric structural design and so on, is expected to enhance membrane performance for target reactions in membrane reactors.

6.2 Conclusions

In this study, B-site doped STO₃-based materials—STFN_x, STZN_x, STFA_x and STFM_x—are synthesized using the solid-state reaction method from commercially available powders. Among the STFN_x series, SrTi_{0.6}Fe_{0.35}Ni_{0.05}O_{3-δ} (STFN005), doped with 5 mol% Ni, is selected for membrane reactor applications due to its high oxygen permeance, effective Ni exsolution, and good stability in reducing environments. In the STZN_x series, SrTi_{0.85}Zr_{0.05}Ni_{0.10}O_{3-δ} (STZN10), with 10 mol% Ni doping, demonstrates outstanding structural stability under reducing conditions and exhibits catalytically active sites due to Ni exsolution, making it a promising candidate for membrane reactors in low p_{O2} . In contrast, Al doping in the STFA_x system proved unsuitable, as increased Al content led to a decline in oxygen permeability. Similarly, Mg doping in the STFM_x system did not show increased performance. MgO segregation was observed, adversely affecting oxygen transport properties. To enhance the viability of STFM_x as an oxygen transport membrane (OTM) for membrane reactors, future research should focus on strategies to mitigate MgO segregation, such as using sol-gel or chemical precursor synthesis to reduce localized Mg-rich regions, utilizing controlled atmosphere sintering to stabilize the lattice and inhibit secondary phase formation, employing rapid sintering methods to shorten high-temperature exposure and time-dependent Mg diffusion, and so on. These approaches could still make STFM_x a promising candidate for use as OTMs in membrane reactors.

Product selectivity in the membrane reactor tests suggests distinct reaction pathways for each material. Further improvements in membrane performance could be achieved by optimizing membrane architecture, particularly through precise thickness control and asymmetric structural design.

Acknowledgements

I feel truly honored to have the opportunity to carry out my doctoral research at Forschungszentrum Jülich GmbH in Germany and the University of Twente in the Netherlands. I am deeply grateful for meeting so many inspiring mentors and supportive colleagues along the way. As this dissertation comes to a close, so too does my four-year journey as a PhD student. Time, like sand slipping through one's fingers, has passed by swiftly. Looking back over the past four years, I have experienced a full spectrum of emotions — joy, challenge, growth, and discovery. Four years ago, I arrived in Germany alone, facing the unknown. From feeling lost at the beginning to becoming confident and independent, I owe every step of progress and growth not only to the invaluable guidance of my supervisors, the encouragement and assistance of my colleagues and friends, but also to the unwavering support of my family. In this chapter, it is with immense gratitude and joy that I would like to thank all the people who have supported, guided, and helped me throughout my PhD journey.

First and foremost, I would like to express my heartfelt thanks to Prof. Dr. Wilhelm A. Meulenberg and Prof. Dr. Arian Nijmeijer for offering me such a precious opportunity to pursue this joint PhD program. When I first arrived at Forschungszentrum Jülich GmbH, it was the warm welcome and thoughtful care from Prof. Meulenberg that gave me confidence and a deep sense of comfort in a foreign country. Throughout the following years, he has consistently supported me, helping me overcome numerous administrative and scientific challenges. Joining his research group has truly been one of the most fortunate aspects of my PhD life.

I also wish to extend my sincere gratitude to my promoter at the University of Twente, Prof. Dr. Arian Nijmeijer, for the many insightful discussions and valuable suggestions that helped improve the quality of my work. He is always quick to respond to my requests and provided great support in my work reports, manuscript revisions, and collaboration between the two institutions.

I am especially thankful to Dr. Stefan Baumann for his long-standing guidance and care. He is my outstanding daily supervisor during my time at IMD-2, Forschungszentrum Jülich GmbH. His suggestions and support accompanied me through every stage of the research. Always kind, patient, and open to discussion, Dr. Baumann generously shared his experience and wisdom. Regardless of the time or situation, he was always willing to engage in result discussions and helped me shape my scientific understanding and thinking. His gentle and encouraging demeanor gave me the courage to explore new directions and try different ideas. Whether in research or daily life, whenever I encountered difficulties, he would work with me to analyze the problems and look for solutions. His trust and encouragement have been powerful driving forces in my personal and professional growth.

The main work of this dissertation was carried out at the Institute of Energy Materials and Devices (IMD-2), Forschungszentrum Jülich GmbH. I would like to express my sincere thanks to Prof. Dr. Oliver Guillon, the director of the institute, for providing the research resources and facilities, as well as for his insightful feedback during my progress presentations and paper writing. I have learned a great deal from his professional suggestions.

Many thanks also go to all my colleagues at IMD-2. Special thanks to Mr. Stefan Heinz for his assistance with lab work, sample preparation, and permeation testing. I gratefully acknowledge Dr. Doris Sebold for SEM measurements, Dr. Yoo Jung Sohn for XRD measurements and Rietveld refinements, Ms. Marie Theres Gerhards for TG measurements, and Mr. Volker Bader and Ms. Andrea Hilgers for their experimental support.

I would also like to extend my appreciation to the colleagues from Universitat Politècnica de València (ITQ), who provided significant help with my experiments. In particular, I am deeply grateful to Dr. María Balaguer Ramírez, Dr. Marwan Laqdiem and Andrés López for their ongoing support in measurements in a membrane reactor and for working with me to resolve experimental issues. I have learned a great deal from their expertise and generous help.

Without all this experimental support, my research work would not have been possible.

I gratefully acknowledge the China Scholarship Council for financial support under Grant No. 202006150006.

Lastly, I would like to express my deepest gratitude to my family. Thank you for your continuous love, encouragement, and understanding throughout my research and thesis writing. Your support has been my greatest strength.

About the Author

Yuning Tang was born on September 24, 1995, in Sichuan, China. She obtained her bachelor's degree in chemical engineering from Beijing University of Chemical Technology (Beijing, China), followed by a master's degree in chemical engineering at South China University of Technology (Guangzhou, China). Her master's thesis, supervised by Prof. Dr. Z. Li, focused on gas separation using Metal–Organic Framework (MOFs) materials.



After spending one year as a research assistant at the university

during the COVID-19 period, she commenced her PhD as a joint doctoral candidate at Forschungszentrum Jülich GmbH (Jülich, Germany) and the University of Twente (Enschede, the Netherlands). Her doctoral research, supervised by Prof. Dr. W. A. Meulenberg and financially supported by the China Scholarship Council (CSC), focused on single-phase oxygen transport membranes. During her PhD, she was the first author of two articles published in the Journal of the European Ceramic Society and presented her research at two international conferences (ECERS 2023 and CMCEE 2024).

Band / Volume 660

Recyclingmöglichkeiten für die Keramikkomponenten einer Festoxidzelle

S. Sarner (2025), VIII, 122 pp ISBN: 978-3-95806-816-2

Band / Volume 661

Methodological Approach Enabling the Two-phase Flow Investigation in Alkaline Electrolysis under Demanding Conditions

S. Renz (2025), IX, 252 pp ISBN: 978-3-95806-821-6

Band / Volume 662

Variable renewable energy potential estimates based on high-resolution regional atmospheric modelling over southern Africa

S. Chen (2025), XIII, 141 pp ISBN: 978-3-95806-822-3

Band / Volume 663

Advances in Understanding Nitrate Aerosol Formation and the Implications for Atmospheric Radiative Balance

A. Milousis (2025), 195 pp ISBN: 978-3-95806-823-0

Band / Volume 664

Optimization of NaSICON-type lithium- ion conductors for solid-state batteries

A. Loutati (2025), viii, 104 pp ISBN: 978-3-95806-824-7

Band / Volume 665

Innovative Plasma Sprayed Thermal Barrier Coatings for Enhanced Flexibility in Gas Turbine Operation

J. Igel (2025), V, 153, XXXVI pp ISBN: 978-3-95806-827-8

Band / Volume 666

Techno- ökonomisches Potenzial dezentraler und autarker Energiesysteme

S. K. A. Risch (2025), xxiii, 210 pp ISBN: 978-3-95806-829-2

Band / Volume 667

Reactive Field Assisted Sintering of Novel Rare Earth Garnets for Plasma Etching Applications

C. Stern (2025), VII, 101, XXVIII pp

ISBN: 978-3-95806-833-9

Band / Volume 668

Effects of mucilage and extracellular polymeric substances on soil gas diffusion

A. Haupenthal (2025), v, 99 pp ISBN: 978-3-95806-834-6

Band / Volume 669

Quantifying Recombination Losses and Charge Extraction in Halide Perovskite Solar Cells

L. Krückemeier (2025), vi, 286 pp

ISBN: 978-3-95806-835-3

Band / Volume 670

Investigation of Dynamic Material Changes During the Preparation of ZnPd Nanoparticles Supported on ZnO and their Catalytic Application in Methanol Steam Reforming on the Atomic Level

A. Meise (2025), xviii, 175 pp ISBN: 978-3-95806-838-4

Band / Volume 671

Improving Energy Efficiency of Public Buildings by Influencing Occupant Behaviour using Dashboards and Gamification

E. Ubachukwu (2025), xxi, 191 pp

ISBN: 978-3-95806-840-7

Band / Volume 672

Exploring Plant Responses to Changing Environments: Integrating Phenotyping and Modeling Across Scales

F. M. Bauer (2025), xxix, 188 pp ISBN: 978-3-95806-845-2

Band / Volume 673

A constitutive theory to represent non-idealities in contacting of SOC interconnect contacts

R. M. Pinto (2025), xii, 139 pp ISBN: 978-3-95806-846-9

Band / Volume 674

Strontium titanate based materials for use as oxygen transport membranes in membrane reactors

Y. Tang (2025), XIV, 132 pp ISBN: 978-3-95806-849-0

Weitere Schriften des Verlags im Forschungszentrum Jülich unter http://www.zb1.fz-juelich.de/verlagextern1/index.asp

Energie & Umwelt / Energy & Environment Band / Volume 674 ISBN 978-3-95806-849-0

